Doctoral Dissertation

Manipulating Electron and Nuclear Spins Dynamics Using Solid Surfaces: A Theoretical Study

（固体表面を用いた電子・核スピンダイナミクス制御に関する理論的研究）

Elvis F. Arguelles

July, 2017

Graduate School of Engineering,
Osaka University

Osaka University

Doctoral Dissertation

Manipulating Electron and Nuclear Spins Dynamics Using Solid Surfaces: A Theoretical Study

by

Elvis F. Arguelles

A thesis submitted in partial fulfilment of the requirements for the degree of Doctor of Philosophy

in the

Division of Precision Science and Applied Physics
Graduate School of Engineering

July 2017

Declaration of Authorship

I, Elvis F. Arguelles, declare that this thesis titled, 'Manipulating Electron and Nuclear Spins Dynamics Using Solid Surfaces: A Theoretical Study' and the work presented in it are my own. I confirm that:

- This work was done wholly or mainly while in candidature for a research degree at this University.
- Where any part of this thesis has previously been submitted for a degree or any other qualification at this University or any other institution, this has been clearly stated.
- Where I have consulted the published work of others, this is always clearly attributed.
- Where I have quoted from the work of others, the source is always given. With the exception of such quotations, this thesis is entirely my own work.
- I have acknowledged all main sources of help.
- Where the thesis is based on work done by myself jointly with others, I have made clear exactly what was done by others and what I have contributed myself.

Signed: _____

Date: _____

OSAKA UNIVERSITY

Abstract

Doctor of Philosophy

Manipulating Electron and Nuclear Spins Dynamics Using Solid Surfaces: A Theoretical Study

by Elvis F. Arguelles

Solid surfaces have been serving as the so-called "playground of physics" since the development of ultra high vacuum environment and advanced experimental techniques for their syntheses and characterizations. Significant discoveries have been unraveled ranging from strange electronic states that are only observable in their presence, to the better understanding of gas molecules-surfaces reactions, all of which have immensely contributed to the progress of surface science. In the past decade, there have been considerable interests in the behavior of electron spins in solid surfaces and their manipulations in the next generation electronic devices have given birth to the field of spintronics. Similarly, the effects of solid surfaces on the electronic and nuclear spins of molecules involved in many heterogenous catalytic reactions have been gaining recognition among surface physicists and chemists. This imply that one can tune the physical properties of solid surfaces by intelligent materials design to influence and manipulate the electronic and nuclear spin states. Fundamental to such design strategies is how to take advantage of the system's symmetry and its breaking processes. Broken symmetries can lead to drastic changes in the electronic, magnetic, and structural properties of solids and gas molecules which in principle can be used to manipulate the behavior of electron and nuclear spin states. In this dissertation, we presented the manipulations of electrons and nuclei spins using symmetry-driven designs of solid surfaces by considering two case studies using a combination of first principles calculations based on the density functional theory (DFT) and model Hamiltonian calculations. In the first case study, we introduced a new way of designing dilute magnetic semiconductors by taking advantage of the layered structures of an oxide crystal in introducing magnetic and non-magnetic impurities. By means of intelligent materials design computations we showed how the local symmetry breaking introduced by impurities at the interstitial regions changes the crystal fields of its surroundings in solids and induce electron spin polarization at the surface layer. We also found that the formation energies of interstitial impurities in a semiconducting lead oxide (PbO) surface is significantly lower compared to their substitutional counterparts due to their unique bonding mechannism with the host crystal

atoms. This bonding results in splitting of the *d*-orbitals of the impurity atoms that induce spin polarization and magnetic moments in the surface. We also found ferromagnetic spin ordering that persists above room temperature which is stabilized by the exchange of electrons between impurities through oxide atoms. Further, we have shown that magnetic moments are strongly enhanced by hole doping which can be attributed to the emptying of the minority spin states, giving rise to stronger spin-polarization in the crystal. In the second case study, we demonstrated from quantum dynamics calculations how the introduction of steps on solid surfaces breaks the rotational symmetry of adsorbing H_2 that leads to the lifting of the angular momentum levels degeneracies and nuclear spin states transition. We showed that H_2 adsorption on stepped Pd surface is governed by a highly anisotropic potential energy surface (PES) that favors adsorption of parallel- over perpendicular-oriented molecule. By solving the quantum motion of H_2 in this anisotropic PES, we found that the two lowest energy states correspond to para and ortho nuclear spin isomers, respectively. Upon comparing the gas and the adsorbed phase rotational energy levels, we found that ortho-H_2 have higher desorption energy compared to para-H_2, implying the separation of the nuclear spin isomers by adsorption on stepped metal surface. We further showed that the presence of steps on metal surfaces promotes H_2 nuclear spin transition by enhancing the surface-molecule hybridization. We have concluded that the key factor to faster ortho-para conversion is to bring H_2 to the so-called molecular chemisorbed state where there is a significant overlap of surface and molecule wave functions. This is only realized by introducing steps on surfaces. The results of this dissertation have significant direct impacts on the design and development of spintronics materials as well as important contributions to the realization of hydrogen-based society.

Contents

List of Figures

List of Tables

Abbreviations

DMS	**D**ilute **M**magnetic **S**emiconductors
DMO	**D**ilute **M**agnetic **O**xides
DFT	**D**density **F**unctional **T**heory
xc	e**x**change **c**orrelation
LDA	**L**ocal **D**ensity **A**pproximation
GGA	**G**eneralised **G**radient **A**pproximation
VASP	**V**ienna **A**b-initio **S**simulation **P**ackage
PAW	**P**rojector **A**ugmented Plane **W**ave
PBE	**P**erdew **B**urke **E**rnzerhoff
vdW	**v**an **d**er **W**aals
DOS	**D**ensity **O**f **S**tates
PDOS	**P**rojected **D**ensity **O**f **S**tates
LDOS	**L**ocal **D**ensity **O**f **S**tates
TM	**T**ransition **M**etals
RT	**R**oom **T**emperature
DoF	**D**grees of **F**reedom
TPD	**T**emperature **P**rogrammed **D**esorption
REMPI	**R**esonance **E**nhanced **M**ulti**P**hoton **I**onization
XMCD	**X**ray **M**agnetic **C**ircular **D**ichroism
CM	**C**enter of **M**ass
FM	**F**erro**M**agnetic
AFM	**A**nti**F**erro**M**agnetic
MFA	**M**ean **F**ield **A**pproximation

Chapter 1

Spin: Electrons and Nuclei

Similar to planets revolving around the sun, an electron possesses aside from orbital angular momentum $\mathbf{l}$, a property analogous to a planet's rotation around its axis, called spin. The electron spin $\mathbf{s}$ is directly coupled to its moment by $\mathbf{m}_e = -g_s\mu_B\,(\mathbf{s}/\hbar)$, where $\mu_B = \frac{e\hbar}{2m_e}$ is the Bohr magneton and $g_s \approx 2$ is the electron spin g-factor. An electron's spin can have two states depending on the projection at some quantization axis, $\pm\hbar\frac{1}{2}$. The positive and negative signs are often called "up" and "down" spins, respectively. This quantization of electron's spin in two directions has been discovered by Otto Stern and Walther Gerlach in the 1920s[2–4]. It is due to this property of electrons that magnetism in a material arises. For instance, nonmagnetic materials have equal number of electrons that are in spin up and down states. However, this is not the case for magnetic materials, in which the density of states (DOS) is split due to different number of spin up and down electrons, schematically shown in Fig.1.1.

Unlike in electrons in which there is a clear distinction between the electron spin and orbital angular momentum, nuclei often behave as one particle and characterized by the total intrinsic angular momentum $\mathbf{I}$, called *nuclear spin*. The magnetic moment associated with nuclear spins of individual protons(neutrons) is $\mathbf{m}_{p(n)} = -g\mu_N\,(\mathbf{I}/\hbar)$, where $\mu_N = \frac{e\hbar}{2m_{p(n)}}$ is the nuclear magneton, $g = 5.5856947$ for proton, and $g = -3.8260837$ for neutron. The magnitude of the nuclear spin of combinations of protons and neutrons in a nuclei depends on the mass number of the nucleus on three cases: 1) when both protons and neutrons in the nucleus are even in number, the nuclear spin is zero, 2) when the total number of protons and neutrons is odd, I takes half-integer values, and

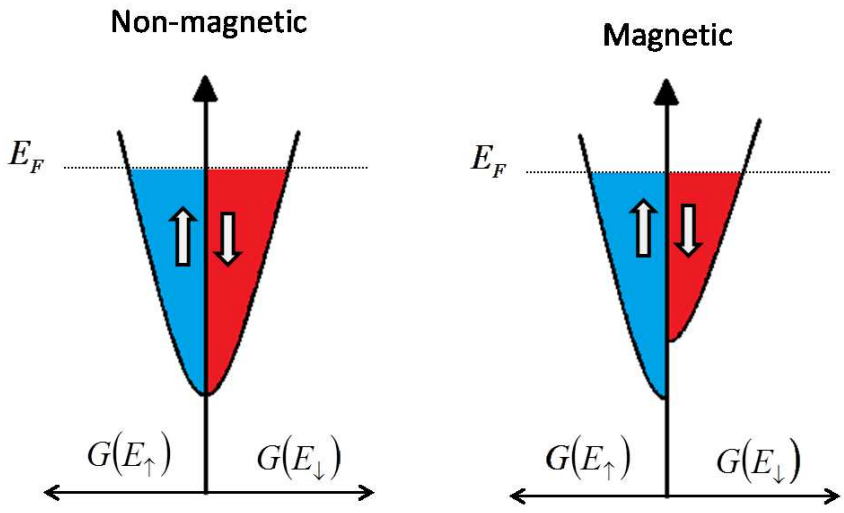

FIGURE 1.1: Schematic diagram of DOS of magnetic and non-magnetic materials. The blue and red shades correspond to up and down spin polarized DOS denoted by $G(E_\uparrow)$ and $G(E_\downarrow)$, respectively. The up and down DOS are filled up the Fermi level E_F.

3) when both protons and neutrons in the nucleus are odd in number, I has integer values. As an example, iron (Fe) (atomic number $Z = 26$) has nuclear spins of either 0 or half-integers depending on whether the isotope mass is even or odd, respectively, e.g. $I = 0$ for ^{54}Fe and $I = 3/2$ for ^{55}Fe. For diatomic molecules such as H_2, the total (*molecular*) nuclear spin $\mathbf{I} = \mathbf{I_1} + \mathbf{I_2}$, where $\mathbf{I}_1(\mathbf{I}_2)$ is the nuclear spin of atom 1(2). The magnitude of the total nuclear spin is 0 for antisymmetric and 1 for symmetric nuclear spin wavefunctions, respectively. The total nuclear wavefunction is composed of spatial and spin parts. The symmetric and antisymmetric properties of the spatial part is govern by the parity $(-1)^J$, where J is the angular momentum quantum number of the molecule. Even and odd values of J result in symmetric and antisymmetric spatial wavefunctions, respectively. This means that $I = 0$ corresponds to even angular momentum J and $I = 1$ corresponds to odd J values.

Chapter 2

Spin in Spintronics and Catalysis

2.1 Electron spin states and spintronics

Even in the early years following its discovery by Stern and Gerlach, spin has played a central role in many branches of condensed matter physics through its incorporation in quantum mechanics by the works of Pauli[5] and Dirac[6]. In practical applications such as in electronics however, this property of electron did not garner much attention until the discovery of giant magnetoresistance (GMR)[7, 8] by Fert and Grünberg. GMR is a quantum mechanical effect in a system consisting of alternating ferromagnetic (FM) and non-magnetic (NM) metal junctions. Depending on the orientation of the magnetization in magnetic layer, the resistance changes from low (parallel orientation) to high (antiparallel orientation). This eventually gave birth to the field of solid state physics called *spintronics*. The realization of electronic devices in which quantum information is carried through an electron's spin rather than its charge is at the heart of an intensive investigation in this rapidly developing field [9–11]. In particular, this field aims to understand how one can exploit the particle's spin degrees of freedom interacting with magnetic properties of a material to reduce power consumption and store and manipulate data above room temperature (RT). It is expected that the next generation spintronic devices will incorporate the creation and control of spin-polarized electrons in a semiconductor [12, 13]. For these devices to be operational, a requirement that electrons are spin-polarized as they travel through the semiconductor (SC) should be achieved. A direct way to do this is by injection of spin-polarised electrons from a ferromagnetic metal to a semiconductor in a FM metal/SC junction. The problem however

with spin injection is the difficulty of preserving the electron spin across the interface because of large differences in the electronic properties of the two materials[9], which can be addressed if one utilizes magnetic semiconductors (instead of metal FM/SC junctions). The challenge therefore is the development and design of materials that are able to combine FM and SC into one functional device that can operate above the room temperature as dictated by today's electronics technology[14]. Traditionally, the creation of such devices starts with the introduction of magnetic ions into conventional semicoductors or semiconducting oxides schematically drawn in Figure 2.1. These magnetic impurities are kept in small amounts to preserve the crystal structure of the host material. A semiconductor with minimal magnetic dopants is called dilute semiconductor (DMS). In these materials, doped ions with partially filled d or f shells serve as

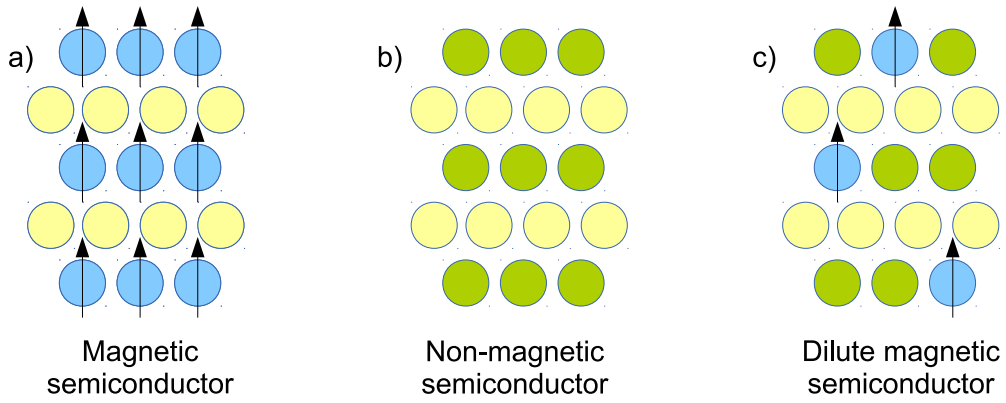

FIGURE 2.1: Schematic diagram showing a) magnetic semiconductor, b) non-magnetic semiconductor and c) dilute magnetic semiconductor (adapted from [1])

sites for localized spins. The interactions between them are believed to be mediated by intrinsic defects that contribute to the overall observed magnetism[15] that persists up to a certain temperature, T_c called Curie temperature. However, the low value of T_c compared to room temperature (typically, $T_c < 100K$) presents a huge challenge for DMS' operations and ultimately, its realistic applications.

It has been proven that ferromagnetism in DMS are generally carrier mediated[16] which allows the modification of magnetic behavior by manipulation of charges. Moreover, theoretical understanding of the relationship between the magnetic and transport properties of material and disorder[17–20] have provided significant insights on the design of DMS. This has inspired a persistent quest for materials with higher T_c and ferromagnetism mediated by carriers and has led to the hypothesis that DMOs would be the

key to bring room temperature T_c[21]. Indeed, groundbreaking experiments by Matsumoto and coworkers observed room temperature ferromagnetism in transition metal (TM)-doped semiconducting oxides[22, 23]. This pioneering work has set the stage for searching similar behavior in other oxides such as ZnO[24], SnO_2[25], Cu_2O[26], and $In_{1.8}Sn_{0.2}O_3$[27] which yield T_c higher than RT. While DMOs with significantly higher T_c around $300K$ have been successfully fabricated, the issue of replicability and poor understanding of the origin of ferromagnetism remain unresolved [28]. Putting these issues into consideration, it is therefore necessary to continue exploring new routes on inducing magnetism to nonmagnetic semiconductors.

2.2 Spin in Catalysis

Energy and angular momentum (spin) are said to be the fundamental parameters that control chemical reactions[29]. In principle, the total spin of the reactants must be equal to the total spin of the products after the reaction. This angular momentum conservation results in spin selective chemical reactions. Typically, chemical reactions are forbidden if the process requires changing of spins. However, some molecular systems with strong spin-orbit interactions may result in electron spin changing along the reaction path[30]. On the other hand, even in the absence of spin-orbit coupling, spin transformation during chemical reactions is still possible by virtue of other magnetic interactions such as hyperfine Fermi contact, Zeeman interaction, etc. For example, consider a pair of molecules or radicals that are initially in triplet state and combine to form a product with zero spin. This entails a spin transformation from the nonreactive triplet radicals to the more reactive singlet radicals that combine to form the diamagnetic, zero-spin product[29]. These spin dependent chemical reactions are also present in many heterogenous catalysis. Some of these involve magnetic nanoparticle catalysts that are found effective towards acetylene and ethylene dehydrogenation[31] and hydrogen production[32]. Other spin dependent reactions on the other hand, do not involve magnetic surface catalysts. A curious case is the rather seemingly simple reaction of O_2 with metal surfaces. Several independent experiments[33–35] have shown that the initial sticking probability during dissociative adsorption of O_2 on Al(111) is very low. Succeeding adiabatic potential energy surface (PES) calculations[36–38] based on DFT were not able to find a dissociation barrier comparable to that of the experiments. This

peculiar property of O_2 adsorption on Al(111) was associated to the hindering of spin transitions of O_2 as it approaches the surface[39]. This effect is also prevalent in the gas-phase reactions in which the triplet O_2 is inert towards singlet reactants.

Equally interesting is the behaviour of the nuclear spins of molecules as they interact with solid surfaces. Similar to electron spins in heterogenous and homogenous catalyses, nuclear spin transitions are possible by means of electronic and magnetic interactions with surface catalysts. Spectroscopic techniques[40, 41] have shown that bound H_2 on a stepped Cu surface is confined as a two-dimensional (2D) quantum rotor on top of step-edge Cu atoms due to large anisotropic adsorbate-surface potential. This hindering of rotational motion along the polar orientation is associated with the differential adsorption on the surface of the two nuclear spin (I) isomers ($I = 0, para$ and $I = 1, ortho$) of H_2[42, 43]. This also means that $ortho(o)$- and $para(p)$-H_2 can now be separated[42–50], an essential step to efficiently store liquid hydrogen. Much of these methods[42, 44, 46–48, 51] of separation involve chromatographic techniques that measure the retention times of o- and p-H_2 on activated alumina columns, and reports on $o - p$ separation using metal catalysts are lacking.

In isolated H_2, the transition between the two nuclear spin isomers is practically forbidden. Theoretically, the rate of transition takes about 10^{20} s. However, the presence of electromagnetic fields, other molecules and solid surfaces generate perturbation potentials that can promote o-H_2 to p-H_2 spin conversion. H_2 has two possible states when interacting with solid surfaces: a) molecularly adsorbed ranging from physisorbed governed mostly by van der Waals interaction to weakly chemisorbed states, and b) dissociated individual hydrogen atoms chemisorbed on the surface. Therefore, the initial prominent picture of nuclear spin isomer transitions imagined o-H_2 in either physisorption state interacting with surface magnetic moments or dissociated state and later on recombine as p-H_2. High resolution electron energy loss (EELS) studies[52–54] have observed for the first time the rotational excitations of diatomic molecules on metal surfaces. From the examination of the rotational spectra of H_2, these researches have concluded that the nature of adsorption can be attributed to purely physisorption state. In spite of the fact that the surfaces used in the study lack magnetic moments, nuclear spin isomer conversion rates were found to be fast. The estimated transition rate is about 2 order of magnitudes faster for H_2 on Ag surfaces[52] than on Cu(100)[53]. These observation of nuclear spin conversions on clean metal surfaces do not fit to any

previous theoretical models for two obvious reasons: 1) H_2 is molecularly physisorbed on metal surfaces and spin conversion via dissociative adsorption and recombination is impossible, and 2) spin conversions via magnetic dipole interactions are only present when the surfaces involved are magnetic. An alternative mechanism[55] involving hyperfine and Coulomb interactions of H_2 with metal surfaces have provided a solid theoretical basis for the observed spin isomer transitions. In this process, an electron from the surface band transfers to the anti-bonding state of H_2 and back to an excited state of the metal surface. The energy release from conversion equivalent to the difference of the two ortho and para states (14.7 meV) is dissipated to formation of electron-hole pairs resulting to triplet metal surface state. This leads to a theoretical estimate of the $o-p$ conversion rate to be ≈ 54 s. Over the years, improved measurement techniques have been employed to accurately estimate the $o-p$ transtition rates on metal surfaces. Some of these are the rotational state selective resonance-enhanced multiphoton ionization (REMPI)-desorption studies of H_2 on solid diamagnetic surfaces[56, 57] which estimated the conversion time be $\approx 600-800$ s. Further, theoretical calculations[58] have shown the importance of molecular orientation to the conversion probability. The transition yield is found to be higher in H_2 oriented perpendicular than the one parallel to the surface. On a stepped metal surface, an EELS study[59] of the rotational populations of H_2 have shown a fast $o-p$ transition rate of 1 s. This conversion time is faster than that predicted by theoretical calculations[55] and has been attributed to the adsorption state characterized by short H_2-surface bond. This suggests that a more refined theoretical model calculation is needed in order explain the observed $o-p$ transition rate.

2.3 Intelligent design of solid surfaces: a means to manipulate electron and nuclear spins

The ability to manipulate electron and nuclear spins provides opportunities to tune different physical properties of materials that are important towards specific applications. For example, electrons and nuclear spins states can be manipulated by electromagnetic fields to gain basic understanding of ultrafast magnetization dynamics of thin films as well as probing the nuclear magnetic resonance (NMR) spectra of atoms and molecules.

On a similar footing, engineering solid surfaces can provide ways to effectively manipulate and control these spin states. To do this, we make use of one of the most fundamental cornerstones of physics: symmetry. Symmetry and its breaking processes have been central to many advances in physics such as superconductivity and cooperative phenomena. Further, symmetry has been the basis for some important scientific contributions such as the exact solution of the Anderson impurity model[60] as well as in heavy electrons systems[61] where an exotic superconducting phase exists.

A solid surface is an example of a system in which symmetry plays an important role. Introduction of a surface imposes a translational symmetry breaking in a crystal. This broken symmetry strongly modifies the electronic, magnetic, and structural properties from the bulk. Another example is the ferromagnetic ordering of spins which occurs as a spontaneous symmetry breaking. When an impurity occupies a site in a crystal, it breaks the local symmetry by changing its surrounding crystal fields. If these impurities are magnetic ions imbeded in a semiconductor, localized spins can couple by exchanging electrons through neighboring atoms, causing magnetic ordering. This mechanism that stabilizes magnetic order is called Zener's double exchange. On the other hand, when the crystal is metallic, conduction electrons can couple with the localized spins leading to a different exchange mechanism called RKKY interactions. Magnetic adatoms coupling on metallic surfaces systems also exhibit these effects through Kondo resonances[62–64]. Symmetry is also important in some molecule and surface interactions. Some organic molecules such as metal pthalocyanides exhibit orbital degeneracies that often survive upon adsorption on metal surfaces. These orbital degrees of freedom lead to a SU(4) symmetric Kondo effect by adjusting the coupling between the molecule and the electron reservoir or the metal surface[65]. Symmetries possessed by metal surfaces can also influence some catalytic reactions. Steps and kinks break the four-fold rotational symmetry (C_4) of surfaces which leads to drastic changes in the adsorption profiles of molecules. On flat transition metals with intact C_4 rotational symmetry, H_2 molecules are found to adsorb dissociatively. On the contrary, the changes in the electronic structure induced by steps of vicinal surfaces allow these molecules to be in molecular adsorption states. As we will show in the succeeding chapters, by inducing a highly anisotropic potential energy surface (PES) steps on metal surfaces influence the quantum dynamics of nuclear spin states of H_2. This PES lifts the degeneracy of rotational states which leads to the difference in desorption energies of the nuclear spin isomers of H_2. Further, by tuning

the electronic properties of metal surfaces, we will show how steps can promote nuclear spin states transitions of H_2.

In this thesis, we present in the following case studies how changing the physical properties of the surface allows one to manipulate the electrons and nuclear spins. By taking

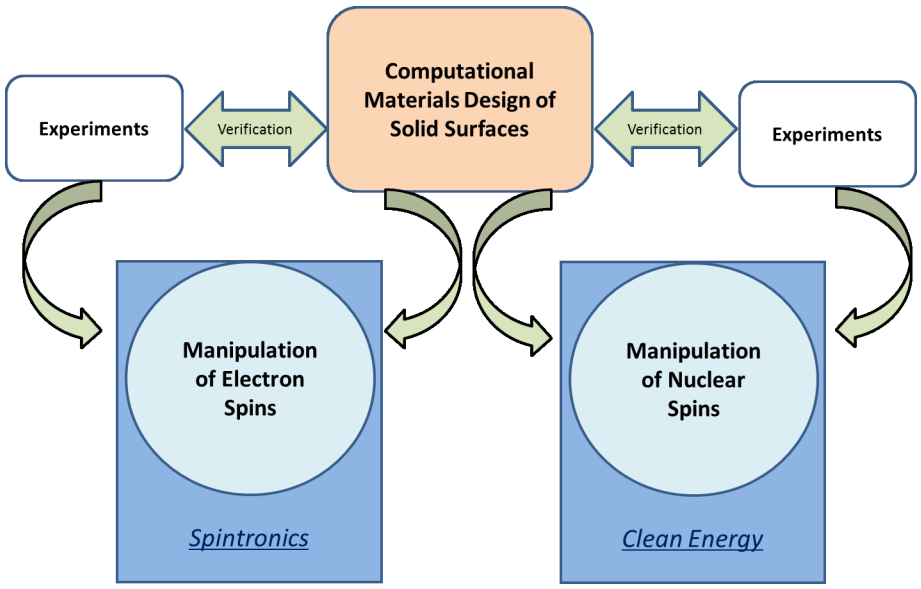

FIGURE 2.2: Proposed design methodology to manipulate electron and nuclear spins using solid surfaces.

advantage of the increasing computational power of computers, we are able to theoretically tweak the physical properties of solid surfaces to directly influence the spin states as shown in Figure 2.2. Our results give insights and help in minimizing the trial and error factors that may arise in experimental methodologies. Our design methodology also enables us to confirm and clarify experimental results by exploring mechanisms that can only be achieved through computational modeling.

In this dissertation, we focused on the two possible applications of spin states manipulations: 1) improving the design of magnetic semiconductors by surface engineering, and 2) tuning the quantum dynamics of nuclear spin states of diatomic molecules by varying the surface electronic profile. In the first case study, we show that by deliberately introducing inhomogeneities in a solid surface, we can promote ferromagnetic ordering of electron spins. Our results give important implications on the design and realization of magnetic semiconductors for spintronics. In most cases, nuclear spin states of atoms in light molecules are easier to manipulate than those in solids. In first principles calculations, these nuclear spin states are can be correlated to the molecules' rotational states.

By influencing the molecules' angular momenta, we can indirectly affect the molecular nuclear spins. In the second case study, we present the effects of steps in metal surfaces in the quantum dynamics and spin state transitions of nuclear spin isomers of hydrogen molecules. Our results find find useful applications such as the design and development of hydrogen storage technologies that are essential in the realization of the so-called hydrogen-based society.

Chapter 3

Surface magnetism in αPbO: A case study

3.1 Interstitial impurity-induced spin-polarization in αPbO

3.1.1 Background

Perfect crystaline surfaces are idealized systems and do not exist in nature. While atoms in solids prefer perfect crystal structures that favor energy minimization, imperfections on the regular geometrical arrangements can form for a variety of reasons. Crystaline defects form due to deformation of solid under excessive pressure, rapid temperature changes during crystal growth and ionizing radiations. The simplest type of a crystal imperfection is called *point* defect. Vacancies, interstitials and impurities belong to this class. A vacancy is formed when an atom is removed or migrate from its original position in the lattice to other areas in the solid. Migrating and extra atoms that cannot be accomodated in lattice sites occupied by other atoms tend to squeeze into interstices and are called interstitials. Impurities are foreign atoms that may substitute the ones comprising the host crystal or occupy the interstitial sites. These defects together with other inhomogeneities such as *dislocations*, *steps* and *kinks* are found in high densities when a crystal is cleaved to form a surface. Even under careful fabrication methods that involve ultra high vacuum condition and and subsequent annealing cannot effectively remove these defects[66]. Understanding how these defects influence the different physical properties of the surface and interfaces opens up possible useful applications in various

fields, most importantly in electronics and catalysis. In electronics, point defects have far greater importance than the rest of the surface defects mentioned above. This is because unlike steps, dislocations and kinks that are localized only at the top most surface layer, point defects can occur at the surface, sub- surface and even in the bulk region of the slab. In some cases, these defects in particular, impurities are deliberately introduced to engineer the electronic properties such as the band gaps of some materials. Pure (*intrinsic*) semiconductors such as silicon (Si) poorly conducts electricity when used in transitors. When the temperature is increased or electrostatic potential difference is applied, some electrons of intrinsic semiconductors are excited to the conduction band, leaving electron vacancies in the valence band called holes. These excited electrons can then move through the semiconductor as a current. For practical applications, semiconductors are often doped with impurity atoms, which depending whether they are *donors* or *acceptors*, shift the position of the valence or the conduction band with respect to the Fermi level. For example, extra electrons from the donor atom when doped into a semiconductor shift the valence band level nearer to the Fermi level, shrinking the band gap. This smaller band gap makes it easier for electrons in the valence band to jump to the conduction band and results to larger current. The opposite effect happen when an acceptor atom is introduced into a semiconductor. In addition, the presence of vacancies in the semiconductor also contribute to these band shiftings and in general to electron/hole mobilities.

3.1.1.1 Interstitial impurities in bulk lead oxides

Lead oxide or PbO has a rich history as photoconductive materials in imaging devices. In recent studies of Bershevich and Reznik on litharge (α-PbO), the low temperature polymorph of lead oxide, it is shown that magnetism can be induced by non-magnetic impurities situated at the interstitial sites between crystal layers[67, 68]. Litharge in its bulk form is thermodynamically stable at room temperature and has a layered structure (shown in Fig.3.1), with a space group $P4/nmm - D$[69].

In this structure, each layer has oxygen atoms sandwiched in between two lead sublayers, with each O atom surrounded tetrahedraly by four Pb atoms. The unique bonding process between the host and the impurity atoms located at the interstitial is said to be responsible for the calculated $2.0\mu_B$ value of local magnetic moment in this material

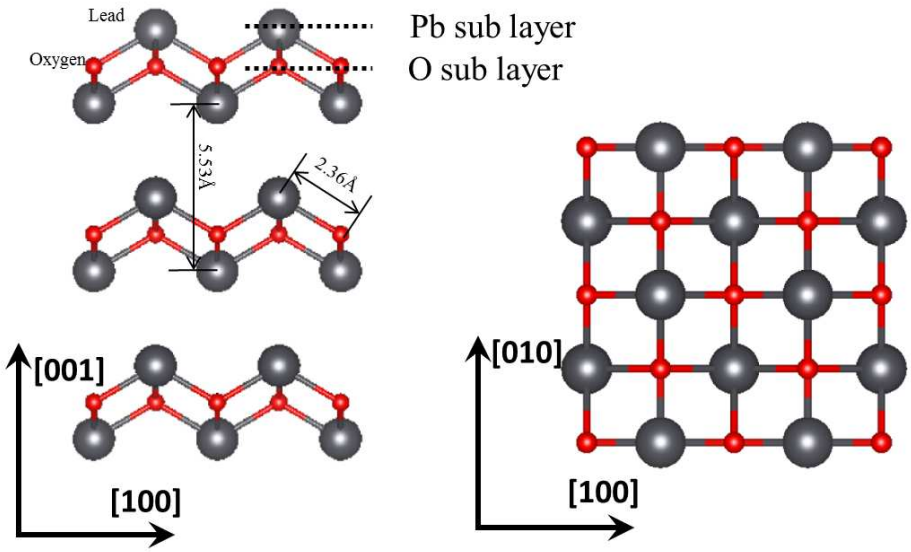

FIGURE 3.1: Bulk of structure of α-PbO. The tetragonal structure has the dimensions, $a = b = 4.06$Å, $c = 5.53$Å and bond length of 2.35Å.

which eventually is considered as one of the routes to the so-called d^0 magnetism[70]. Having known that it is possible to use litharge as a DMO similar to ZnO, TiO and other oxides, a rather common approach is proposed in this thesis in which the intrinsic magnetic nature of $3d$ transition metal oxides are exploited and introduced as interstitial impurities. Furthermore, since RT ferromagnetism is easily realized using thin films and nanoparticles and that ferromagnetic signals are believed to be linked to states near surfaces, interfaces and grain boundaries [71, 72], the study presented here is relatively pioneering in terms of subsurface impurity induced magnetism of α-PbO surface.

3.1.2 Electronic properties of pristine PbO surface

The breaking of symmetry imposed by the surface has introduced a small energy shift of the Fermi level of the system's density of states (DOS) in Figure 3.2. In this figure, the red and blue lines are total DOS of O and Pb respectively while the black line denotes the total DOS per unit cell. Oxygen's p-states dominates the valence band while Pb's p-states take over the conduction band. The deepest energy regions are occupied by s-states of the oxygen atoms with very small contribution coming from the p-states of the lead atoms. Further analysis of this DOS show that these states are located at almost the same energies consistent with sp^3 hybridization in this material. In the bonding process, Pb forms five degenerate hybrid orbitals, four of which forms overlaps with

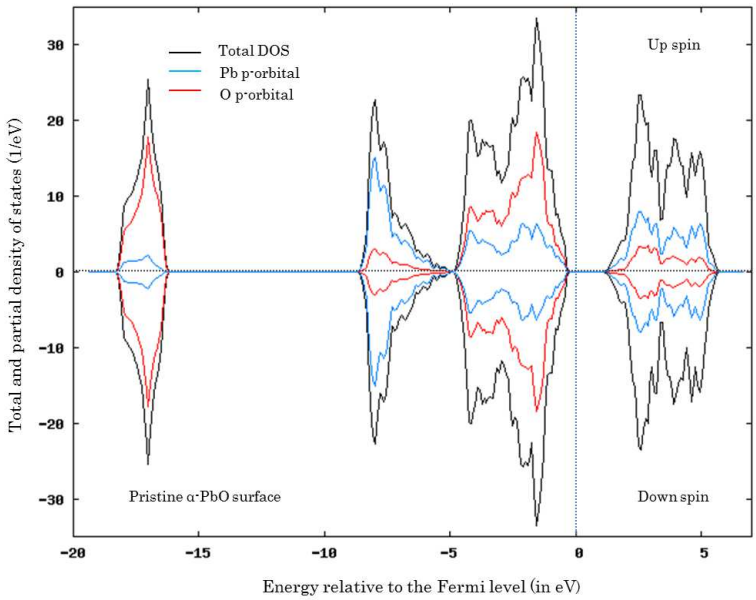

FIGURE 3.2: Total density of states (DOS) per unit cell (black line) and densities of states of Pb (blue line) and O (red line) atoms. The Fermi level is shown as the dashed line.

oxygen's sp^3-hybrids. The other remaining orbital comprising of $6s$ do not participate to bonding and are located deep below the Fermi level

3.1.3 Surface spin polarization induced by magnetic interstitial impurities

Interstitial defects are generated by placing impurities in between 2 layers oxygen atoms and allowing to relax until the system reaches the minimum energy configuration. After optimization, the system is found to be stable when bonded with oxygen atoms with the oxygen-impurity-oxygen (O-I-O) bond length given in table 2. Generally, the impurities tend to bond effectively with the oxygen atom located at the upper layer O_u, than the one in the lower layer, O_l as shown by the bond values in Table 3.1. For the cases of transition metal elements, the O-I-O bond lengths are quite short; Fe forming the shortest bond of 1.88 Å with O_u atom in the upper layer. The non-magnetic Pb interstial however forms a relatively longer bond of around 2.54 Å with O_u but still shorter compared to that of (cf. ref[67]) where the impurity is bonded with Pb atoms instead of oxygen, suggesting an increase in stability of the present system.

Calculated magnetic moments per supercell (and local magnetic moments) for system with Fe, Mn and Pb are $2.25(2.32)\mu_B$, $3.11(3.12)\mu_B$, and $0.94(0.514)\mu_B$ respectively,

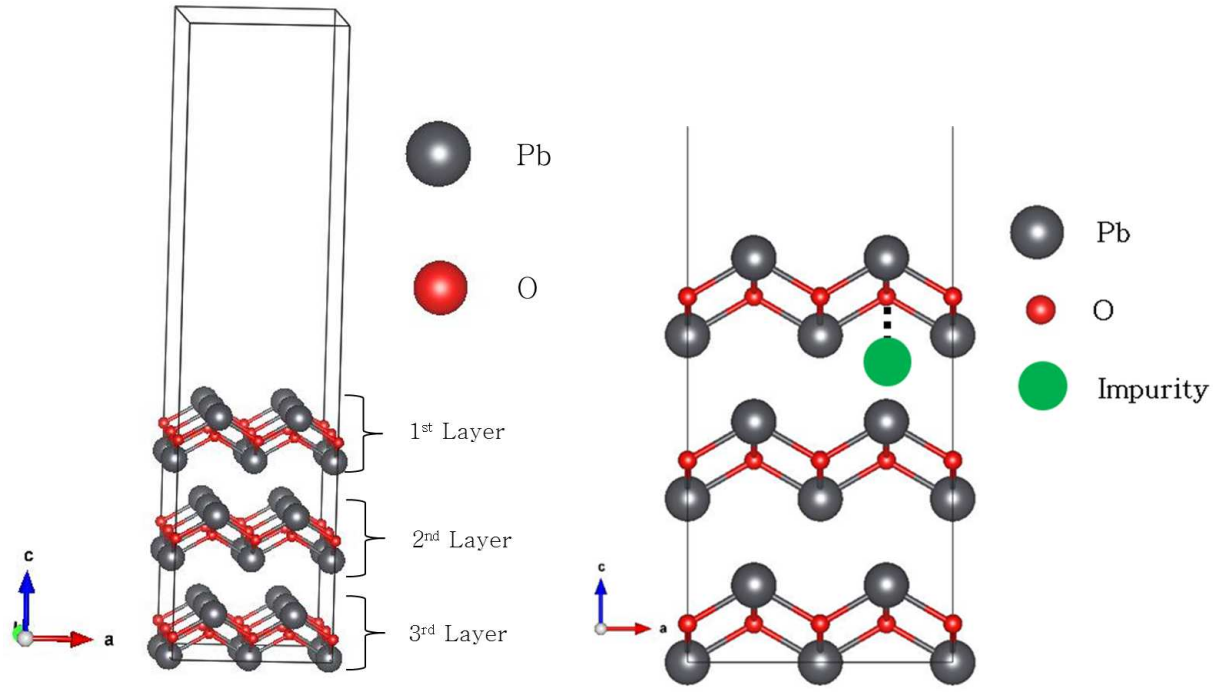

(A) (B)

FIGURE 3.3: (a) Litharge slab model consisting of three layers of lead monoxide with 20Å separation distance between slabs. (b) Interstitial impurity model. (The Fermi level is shown as the dashed line.)

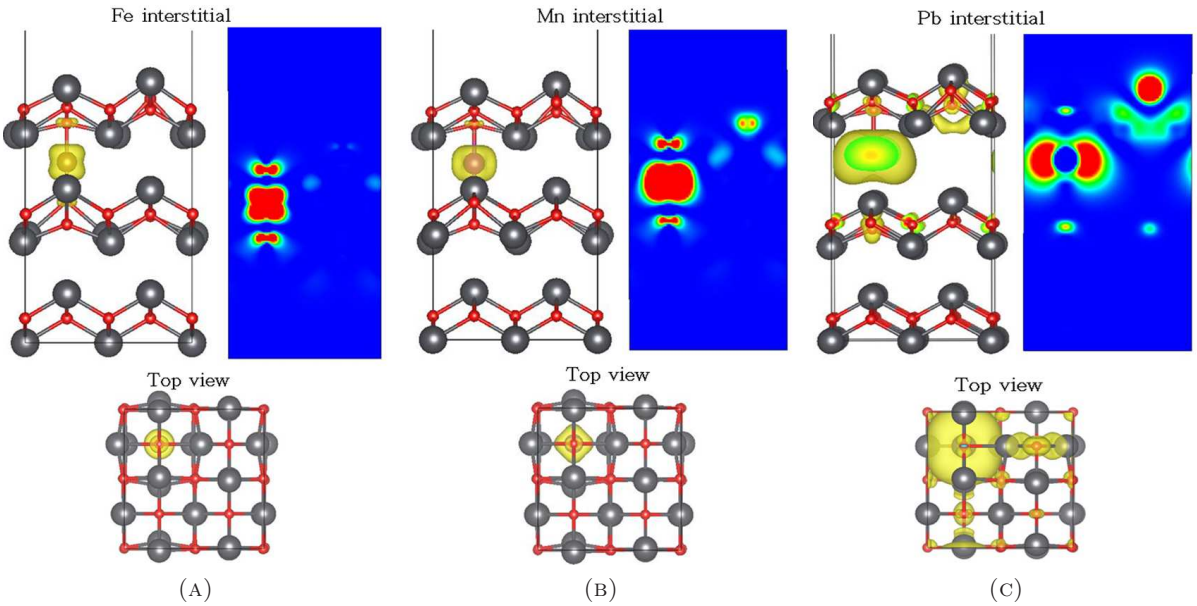

(A) (B) (C)

FIGURE 3.4: Spin density plots for (a) Fe, (b) Mn, and (c) Pb interstitials plotted with isovalues of $0.05e/\text{Å}^{-3}$.

Impurity	O_u(upper) bond (in Å)	O_l(lower) bond (in Å)	Magnetic moment (in μ_B/supercell)
Fe	1.881	1.888	2.250
Mn	1.937	1.945	3.100
Pb	2.538	3.493	0.940

TABLE 3.1: Host impurity bond lengths and magnetic moments per supercell for Fe, Mn and Pb interstitials. The impurity atoms are bonded with two Oxygen atoms, one located at the upper layer and the other at the second layer.

and the corresponding spin density plots are shown in Figures 3.4a-c. These magnetic moments are highly localised in the case of transition metals (Fe and Mn) and overly dispersed for Pb. The strong bonding between transition metals and the host's oxygen atoms create distortions at the surface (Figures 3.4(a) and 3.4(b)) as these oxygen are drawn closer towards the impurities to form O-I-O bonds. Upon bonding, these oxygen atoms gained magnetic moments of $0.036\mu_B$ for O_u and $0.037\mu_B$ for O_l induced by Mn and $0.062\mu_B$, for both O_u and O_l atoms induced by Fe. These defect effects can be traced up to far away neighbouring atoms located at the surface and especially pronounced in the case of Mn in Figure 3.4(b). While the calculated magnetic moment localised at the Pb interstitial is the smallest among impurities, its introduction to the system has induced long range disorder effects (Figure 3.4(c)) which tail up to the surface atoms. The shifting of DOS to the lower energy region is a notable feature among all cases upon the introduction of interstitials as illustrated in Figure 3.5 indicating n-type nature, with the gap occupied by d (TM) or p (Pb)states due to impurities (right hand side panel).

Although this feature is evident for all cases, the bonding mechanisms are different for each case. The t_{2g} (d_{xy}, d_{yz}, d_{zx}) orbitals of $3d$-transition metals hybridise with the host's s and p orbitals forming antibonding and bonding states. The Fermi level lies at the non-bonding e_g (d_{z^2}, d_{x^2}) states for the case of Fe interstitial. This is however different for Mn impurity. Due to the strong hybridisation between the host's oxygen atoms and the non-magnetic Pb impurity, a local magnetic moment which extends up to several neighbouring atoms is induced. When Pb interstitial bonds with the nearest oxygen atom of the host, a whole new different picture emerges that results to spin polarisation of both the host matrix and impurity. Firstly, the minority of Pb impurity's states are excited in energy leaving some of the majority antibonding p states at the Fermi level more than half-filed (bottom right hand of Figure 3.6). A mixed of Pb s and p states overlap with oxygen's bonding p states below the Fermi level with some of

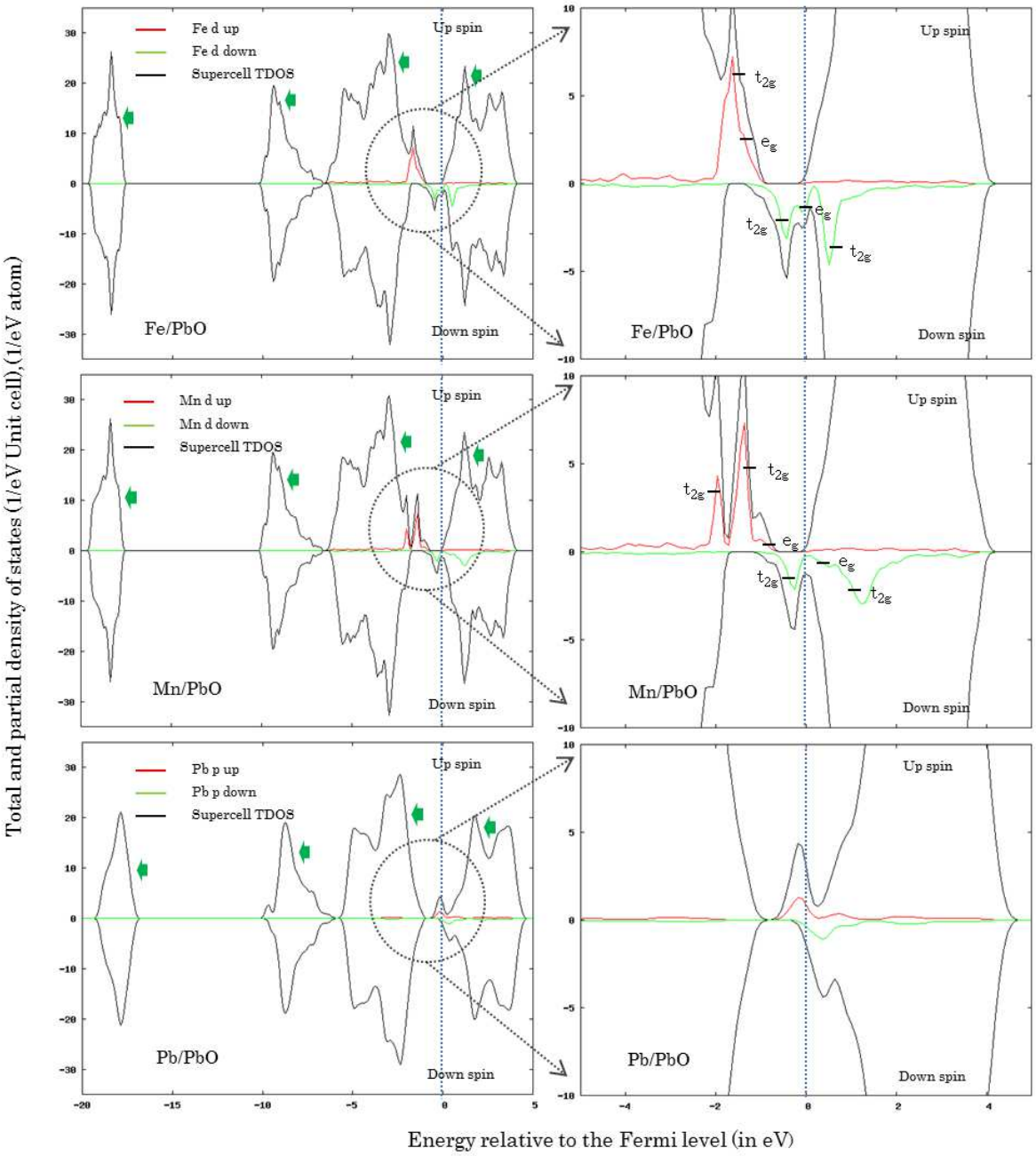

FIGURE 3.5: The densities of states for α-PbO slab with transition metals (Fe and Mn) and Pb interstitials. The right panel shows the calculated DOS near the Fermi level (shown as blue vertical dashed line). Coloured lines (red and green) show the partial density of states per impurity atom's d or p orbitals at the interstitial and the solid black lines are the total averaged DOS per unit cell.

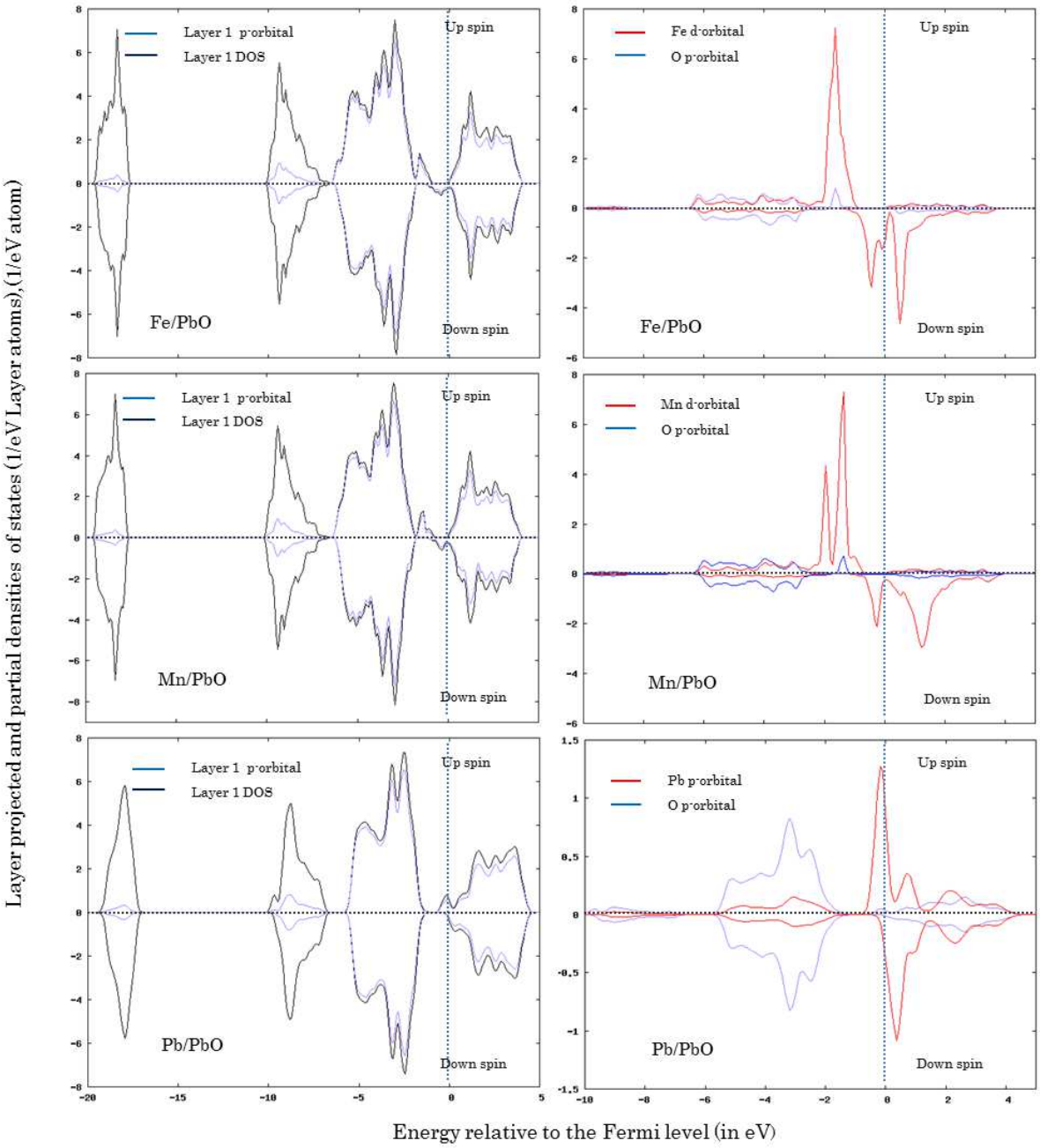

FIGURE 3.6: Calculated 1st layer DOS (left panel) and partial DOS of impurity and nearest neighbor oxygen atom (please see the scale)

Pb's s states dominates the lower energy regions and are spin split. These in turn give rise to the calculated magnetic moment and defect states tailing far away from the Pb interstitial. Remarkably, even in the absence of unpaired electrons, a 0.94 μ_B supercell magnetic moment can be generated by Pb interstitials in PbO. The immediate effects of these defects on the surface layer of α-PbO are illustrated in Figures 3.4 and 3.6. Geometrically, they induce subtle lattice distortions at the surface that cause elongation and shortening of some Pb-O bonds (Figure 3.4), particularly notable for TM impurities. Furthermore, the layer resolved densities of states in Figure 3.6 show almost neglible splitting of states at the lower energy regions and split impurity states are located either at or near the Fermi level. Moreover, the impurities' spin split d or p states overlap with the host oxygens' p valence bond states and additional impurity states are present in the band gap as shown in Figure 3.6. The magnetic moments for the case of magnetic impurities induce slight spin polarization of the surface layer's oxygen p states illustrated at the left-hand side of Figure 3.6.

3.1.4 Summary and Conculsions

Given the strong evidence that ferromagnetism is closely associated with near surface and interfaces, litharge surface or α-PbO (001) has been investigated as a candidate material for spintronics application. In particular the introduction of 3d transition metal impurities (Fe and Mn) traditionally used in other DMSs and DMOs into litharge surface results in supercell magnetic moment values of 2.25 μ_B and 3.11 μ_B for Fe and Mn intersitials respectively. These magnetic moments are highly localised at the interstitals although small polarisation effects run up to a few neighbouring atoms. In addition, although lower in value compared to the cases with transition metal interstitials, the 0.94μ_B magnetic moment generated by Pb interstitial defect in litharge is of longer range and present an equally interesting mechanism. The interstitial impurities polarise the p states of the surface layer resulting to spin split impurity states at the Fermi level. In the future, this study aims to explore the exchange interactions between magnetic impurities in this material and the effects of disorder in the magnetic properties. It is expected that similar to other oxides, manipulating α-PbO either by substitutional doping or interstitial with appropriate elements will also lead to the much coveted room temperature ferromagnetism.

3.2 Surface magnetism induced by magnetic interstitials in αPbO

3.2.1 Background

In recent years, intensive research efforts have been focusing on dilute magnetic semiconductors (DMS) to design electronic materials that can be used for spintronics applications. These materials must be able to combine high Curie temperature and significant spin-polarisation of charge carriers as well as compatibility with existing electronics technology to be employed industrially[14]. The introduction of ions with partially filled d or f shells as substitutional dopants has been the traditional choice to induce magnetism in non-magnetic semiconductors. These partially filled orbitals can serve as sites for localised spins and the interactions between them are believed to be mediated by intrinsic defects in these materials[15, 20]. X-ray magnetic circular dichroism (XMCD) measurements on semiconducting oxides doped with magnetic atoms on the other hand, reveal ferromagnetic order that persists above room temperature[21, 73–77] and a paramagnetic interaction between magnetic impurities, suggesting that the dopants may not be responsible for the observed room temperature (RT) ferromagnetism[78–83]. It is therefore necessary to continue exploring new frontiers in designing DMS.

In the previous section we discussed the electronic properties of α-PbO with magnetic and non-magnetic interstitials and show that due to the layered structure and unique bonding mechanism between the host crystal and impurities, large magnetic moments of values $2.25\mu_B$, $3.11\mu_B$ and $0.94\mu_B$ for Fe, Mn and Pb interstitial ions respectively, can be realized. Further, structural calculations show that with respect to layered structure, the interstitial impurities possess low formation energies as is shown by our work consistent with the findings of Berashevich and Reznik who extensively studied interstitial defects in the bulk αPbO [84]. In this section, we present a realization of ferromagnetic order in αPbO surface with interstitial Fe impurity and its possible exchange mechanism using *ab-initio* calculations based on density functional theory (DFT)[85, 86] implemented in Vienna Ab-initio Simulation Package (VASP)[87]. The magnetic properties are calculated by employing a 4×4 supercell consisting of a three-layered, 194-atom slab with $20\mathring{A}$ vacuum simulating the surface. A single Fe interstitial in a 2×2 supercell is used in calculating the electronic properties which determine the bonding mechanism that

gives rise to the induced magnetic moment in the system. The readers are refered to Appendix B for a comprehensive discussion on its calculation details. Furthermore, to discuss the exchange mechanism in the system, 1×1 and 3×3 supercells are employed to simulate 25% and 2.78% impurity concentrations repectively.

3.2.2 Electronic and magnetic properties of αPbO with magnetic interstitials

We consider a pristine, non-magnetic, αPbO semiconductor with an indirect band gap of 1.95 eV, and a layered structure belonging to space group of P4/nmm-D[88] as a host crystal. The interstitial impurities are modelled by sandwiching Fe ions in between two layers of PbO slab, which upon structural optimization are found to bond effectively with the oxygen atom located at the upper layer. In the bonding process, the five-fold degenerate Fe $3d$ states split into $d_{x^2-y^2}$, $d_{z^2-r^2}$, d_{xy} and the doubly degenerate d_{yz}/d_{xz} orbitals shown in Figure 3.7. Following Hund's rule, two up electrons occupy the majority spin d_{yz}/d_{xz} orbital while its minority spin states are empty. The $d_{x^2-y^2}$'s minority spin states near the Fermi level on the other hand is partially occupied. This partial occupation and level splitting induce the calculated magnetic moment of $2.25\mu_B$ in this system upon the introduction of Fe interstitials.

3.2.3 Magnetic order and exchange mechanism

Using supercell approach, we determine the order of magnetism in the system by considering the energy difference between antiferromagnetic (AFM) and ferromagnetic (FM) configurations of two Fe interstitial atoms separated by a distance of 4 Å from each other. This energy difference is given by $E_M = E_{AFM} - E_{FM} = 0.068$eV at 3.125% concentration. Because the sign of E_M enables us to ascertain the type of magnetic coupling between two Fe atoms; positive(negative) means FM(AFM), the resulting positive energy difference between magnetic states suggest FM order is stabilized in this system.

Furthermore, it is equally interesting to determine the dominant exchange mechanism that stabilizes ferromagnetic coupling between Fe atoms in αPbO. The calculated density of states shown in Figure 3.8 at different Fe concentrations namely, 2.78% and 25% which represent the dilute and high concentration limits, may in principle be used for this

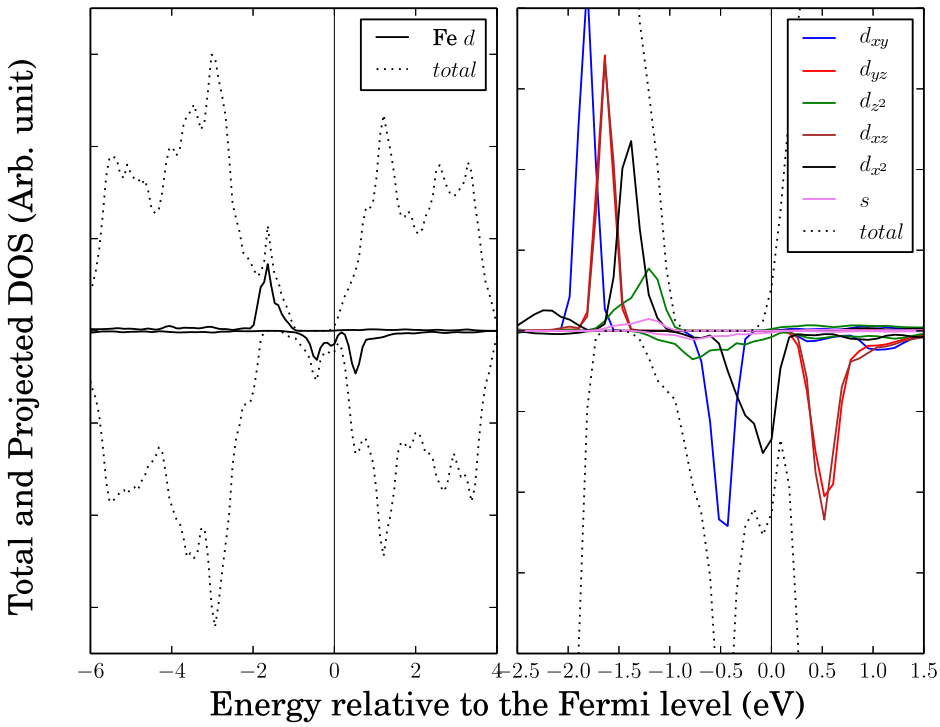

FIGURE 3.7: (Colour online) Total and projected densities of states of αPbO surface with Fe interstitial. The Fermi level is set to zero and the vertical black lines are guides for the eyes.

purpose [89, 90]. Our calculation shows that as the concentration of Fe interstitials in αPbO surface increases, the d_{xz} which lies around the Fermi level and partially occupied, broadens. This broadening shifts the density of states towards lower energies that leads to energy gain which is proportional to the bandwidth of the impurity band. The ferromagnetic state is stabilized by this energy gain due to band broadening and is associated with Zener's double exchange mechanism[89, 91] which is dominant in our system.

3.2.4 Curie temperature

We further show that this ferromagnetic order may persist above room temperature and the classical Heisenberg Hamiltonian,

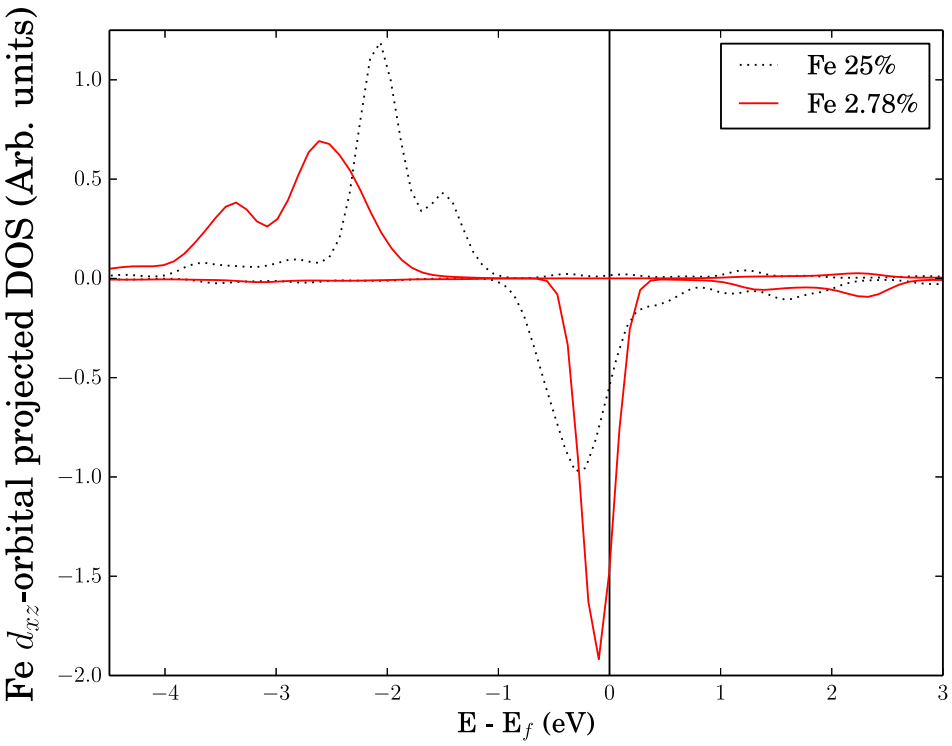

FIGURE 3.8: Density of states projected on Fe's d_{xz} state for 2.78% (solid) and 25% (dotted) concentrations. The broadening of the DOS at higher Fe concentration corresponds to an energy gain that stabilizes ferromagnetism.

$$H = -\sum_{ij} J_{ij} \mathbf{e}_i \cdot \mathbf{e}_j \tag{3.1}$$

where $\mathbf{e}_i(\mathbf{e}_j)$ is the unit vector pointing at the direction of the local moment at site $i(j)$ and J_{ij} is the exchange integral between two magnetic atoms at sites i and j, may be used to estimate the Curie temperature. In the mean-field approximation (MFA), it is expressed in a simplified form[92] as $k_B T_C^{MFA} = \frac{2}{3} E_M$ (k_B is the Boltzmann constant). The estimated mean field Curie temperature for our system is 532 K. Moreover, using Monte Carlo (MC) simulation of Eq.(3.1), a more accurate Curie temperature of around 472 K is obtained which is well above the room temperature, highlighting the possibility of employing αPbO surface with Fe interstitials as a DMS device for spintronics applications. Finally, it is worth noting that the surface p states are spin-polarised by the interstitial impurity and are spin split at the Fermi level (not shown), which is important in realising spin-dependent current injection devices.

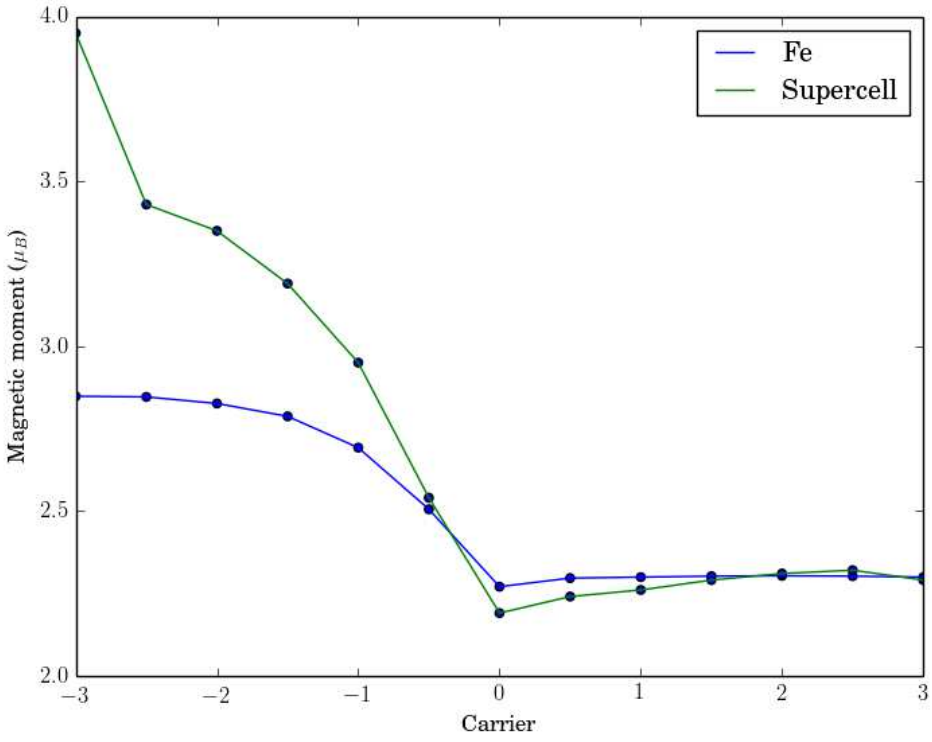

FIGURE 3.9: Effects of carrier concentration on the magnetic moment at the interstitial impurity site (blue curve) and surface (green curve).

3.2.5 Effects of carrier concentration

We present in Figure 3.9 the effects of carrier concentration to the magnetic moments localized at the interstitial impurity and induced at the surface. When the change in the charge carrier concentration (δN) is zero, the interstitial Fe has larger magnetic moment than the solid surface. However, when the concentration of hole is increased corresponding to $\delta N < 0$, the magnetic moment localized at the Fe impurity increases and then suddenly plateaus for more negative δN. On the other hand, we can see a monotonic increase in the magnetic moment at the surfae with increasing hole concentration. This increase in spin polarization clearly cannot be attributed to the magnetic interstitial impurities. On the contrary, electrons concentrations do not significantly change the magnetic moments of both interstitial and surface. In order to gain further insights we show in Figure 3.10 the DOS projected on the different d states of Fe together with the scaled total DOS of the surface for $0 \leq \delta N$ and $\delta N \geq 0$. Initially, before electron and hole doping, both the majority and minority d_{xy} states (blue curve) and d_{z^2} (green

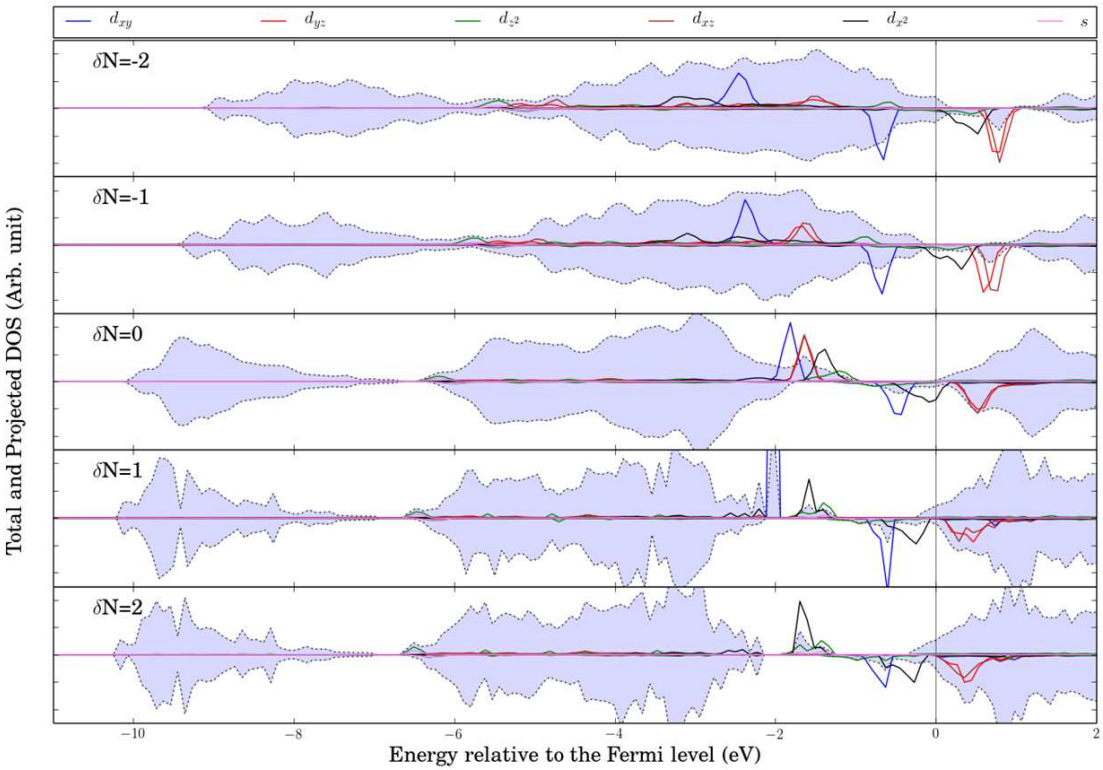

FIGURE 3.10: Total (scaled, shaded) and projected densities of states for different hole and electron concentrations in αPbO with Fe interstitials.

curve) are filled. The doubly degenerate d_{xz} and d_{yz} majority spin states are occupied while the minority spin states are empty. The d_{x^2} majority spin states (black curve) are occupied and its minority spin states lie in the Fermi level and partially occupied (half metallic). When the hole concentration is increased, $\delta N \leq 0$, the total and partial DOS of the system shift above the Fermi level. This shifting of the Fermi level causes the partially occupied minority d_{x^2} spin states to be empty, incuding spin polarization at Fe interstitial and hence, the initial increase in the magnetic moment at the impurity site in Figure 3.9. Similarly, the total DOS of the αPbO slab exhibit the same emptying of the minority spin states, inducing spin polarization at the surface. These spin polarizations are experienced by Pb and O atoms located at the surface layers through the splitting of their respective p and s states. Since more of states are spin polarized at the surface, the increase in magnetic moment of the slab is more dramatic than that of the interstitial site. On the other hand, electron doping concentrations shift the DOS to energies below the Fermi level. This causes the full occupation of the previously partially occupied minority d_{x^2} spin states. The other orbitals are not affected by this shifting of the DOS and hence, the almost constant magnetic moment at the interstitial site. The split states

of the surface exhibit the same nature as that of the interstitial site and therefore there are neglible changes in the slab's magnetic moment. What remains to be seen are the effects of charge carrier concentration to the magnetic ordering of spins in αPbO. This entails collinear supercell calculations for different electrons and holes concentrations in the presence of interstitial impurities. This will be the subject of future calculations.

3.3 Summary and Conclusions

In summary, the electronic and magnetic properties of αPbO with Fe interstitial is theoretically investigated. Upon bonding with the host's oxygen atom located at the surface layer, the d states of Fe interstitial spin split inducing spin polarisation in the slab. In addition, we predict a ferromagnetic order stabilized by double exchange mechanism in the system with a high Curie temperature in both MFA and MC simulation. These findings have important implications not only in designing DMS for spintronics applications but also in studying magnetism in surfaces. Aside from substitutional doping, we introduce a new way of inducing magnetism in DMS through magnetic interstitial defects. We have also investigated the effects of electron and hole doping in αPbO with Fe interstitials. Our results show that increasing hole concentrations promote an increase of the magnetic moment of both the impurity and surface. The electron doping on the other hand does not completely affect the magnetic moment at the impurity site and the surface. These effects on the magnetic moments of electron and hole doping has been explained by the shifting of the DOS below and above the Fermi level, respectively, that cause the occupation and emptying of the d orbitals of Fe and the total DOS of the surface.

Chapter 4

H_2 nuclear spin dynamics on stepped Pd surface: A case study

4.1 Model and Theory

4.1.1 Isolated H_2

4.1.1.1 Hamiltonian

The hydrogen molecule is composed of 2 electrons and 2 protons and can be described be the following 4-body Hamiltonian

$$H = -\frac{\hbar^2}{2m}\sum_{i=1}^{2}\nabla^2_{\mathbf{r}_i} - \frac{\hbar^2}{2M}\sum_{j=1}^{2}\nabla^2_{\mathbf{R}_j} + \frac{1}{4\pi\epsilon_0}\left(-\sum_{i=1}^{2}\sum_{j=1}^{2}\frac{Z_j e^2}{r_{ij}} + \sum_{i=1,i'\neq i}^{2}\frac{1}{2}\frac{e^2}{r_{ii'}} + \sum_{j=1,j'\neq j}^{2}\frac{1}{2}\frac{Z_j Z_{j'} e^2}{R_{jj'}}\right). \quad (4.1)$$

The first and second terms correspond to the kinetic energies of electrons and protons respectively. The third term is the potential energy between electrons and protons with $r_{ij} = \mathbf{r}_i - \mathbf{R}_j$, and ϵ_0 is the permittivity of free space. $\mathbf{r}_i(\mathbf{R}_j)$ is the coordinate of the $i(j)$th electron(proton). The fourth and fifth terms are the repulsive potentials between ith and i'th electrons and between jth and j'th protons, respectively, where

$r(R)_{ii'(jj')} = \mathbf{r}(\mathbf{R})_{i(j)} - \mathbf{r}(\mathbf{R})_{i'(j')}$. We invoke the Born-Oppenheimer approximation which assumes that the lighter electrons adjust adiabatically to the motion of the much heavier nucleus and remains instantaneously in it ground state. With this, the electronic state depends on the nuclear coordinates $\mathbf{R}_j$ only parametrically and allows us to write the total wavefunction as

$$\Psi = \psi_n(\mathbf{r}_i; \mathbf{R}_j)\varphi_{n;N}(\mathbf{R}_j) \tag{4.2}$$

where the indices n and N correspond the quantum states of electrons and nuclei, respectively. If we operate the Hamiltonian (4.1) on the total molecular wavefunctions (4.2), we obtain two equations describing the motion of the electrons,

$$\left[-\frac{\hbar^2}{2m}\sum_{i=1}^{2}\nabla^2_{\mathbf{r}_i} + V(r_i, R_j)\right]\psi_n(\mathbf{r}_i; \mathbf{R}_j) = U(\mathbf{R}_j)\psi_n(\mathbf{r}_i; \mathbf{R}_j) \tag{4.3}$$

where $V(r_i, R_j) = \frac{1}{4\pi\epsilon_0}\left(-\sum_{i=1}^{2}\sum_{j=1}^{2}\frac{Z_j e^2}{r_{ij}} + \sum_{i=1,i'\neq i}^{2}\frac{1}{2}\frac{e^2}{r_{ii'}} + \sum_{j=1,j'\neq j}^{2}\frac{1}{2}\frac{Z_j Z_{j'} e^2}{R_{jj'}}\right)$ and of the nuclei,

$$\left[-\frac{\hbar^2}{2M}\sum_{j=1}^{2}\nabla^2_{\mathbf{R}_j} + U(\mathbf{R}_j)\right]\varphi_{n;N}(\mathbf{R}_j) = E_{n,N}\phi_{n;N}(\mathbf{R}_j). \tag{4.4}$$

$E_{n,N}$ is the total energy that corresponds to the eigenvalues of the full molecular Hamiltonian (4.1). The eigenvalues $U(\mathbf{R}_i)$ of the electronic Schrödinger equation can be considered as an adiabatic potential energy surface (PES) of the nuclear motion and can be obtained from electronic ground state calculations.

4.1.1.2 Rotational states

The eigenvalue equation of the nuclear motion can be written in terms of the centre of mass (CM) and H_2 bond length using the following transformations,

$$\mathbf{R} = \frac{1}{M}\left(M_1\mathbf{R}_1 + M_2\mathbf{R}_2\right) \tag{4.5}$$

$$\mathbf{r} = \mathbf{R}_1 - \mathbf{R}_2, \tag{4.6}$$

where $M = M_1 + M_2$ is the total nuclear mass, $|\mathbf{r}| = r$ is the H-H nuclear distance, and $\mathbf{R}$ is the centre of mass (CM). Equation (4.4) reads

$$\left\{-\frac{\hbar^2}{2}\left[\frac{1}{M}\nabla^2_{\mathbf{R}} + \left(\frac{1}{M_1} + \frac{1}{M_2}\right)\nabla^2_{\mathbf{r}}\right] + U(\mathbf{R},\mathbf{r})\right\}\varphi_{n;N}(\mathbf{R},\mathbf{r}) = E_{n,N}\varphi_{n;N}(\mathbf{R},\mathbf{r}). \quad (4.7)$$

In spherical polar coordinates, $\nabla^2_{\mathbf{r}}$ can be written as

$$\nabla^2_{\mathbf{r}} = \frac{1}{r^2}\frac{\partial}{\partial r}r^2\frac{\partial}{\partial r} + \frac{1}{r^2\sin\theta}\frac{\partial}{\partial\theta}\sin\theta\frac{\partial}{\partial\theta} + \frac{1}{r^2\sin^2\theta}\frac{\partial^2}{\partial\phi^2}. \quad (4.8)$$

Setting $\frac{1}{\mu} = \frac{M_1+M_2}{M_1 M2}$, the equation for nuclear motion can be expressed as

$$\left[-\frac{\hbar^2}{2}\left(\frac{1}{M}\nabla^2_{\mathbf{R}} + \frac{1}{r^2}\frac{\partial}{\partial r}r^2\frac{\partial}{\partial r} + \frac{1}{\mu r^2}\mathbf{L}\right) + U(\mathbf{R},r,\theta,\phi)\right]\varphi_{n;N}(\mathbf{R},r,\theta,\phi) = E_{n,N}\varphi_{n;N}(\mathbf{R},r,\theta,\phi), \quad (4.9)$$

where

$$\mathbf{L} = \frac{1}{\sin\theta}\frac{\partial}{\partial\theta}\sin\theta\frac{\partial}{\partial\theta} + \frac{1}{\sin^2\theta}\frac{\partial^2}{\partial\phi^2} \quad (4.10)$$

If we take the position of the CM for the nuclear motion arbitrarily, Equation (4.9) is reduced to the rotational eigenvalue equation of isolated H_2 in gas phase given by

$$\left[-\frac{\hbar^2}{2}\left(\frac{1}{r^2}\frac{\partial}{\partial r}r^2\frac{\partial}{\partial r} + \frac{1}{\mu r^2}\mathbf{L}\right)\right]\varphi_N(r,\theta,\phi) = E_N\varphi_N(r,\theta,\phi). \quad (4.11)$$

We then assume that H_2 is a rigid rotor by fixing $r = r_e$, where r_e is the equilibrium bonding length and neglecting the corresponding kinetic energy. We obtain the equation of purely rotational states

$$\left[-\frac{\hbar^2}{2\mu r_e^2}\left(\frac{1}{\sin\theta}\frac{\partial}{\partial\theta}\sin\theta\frac{\partial}{\partial\theta} + \frac{1}{\sin^2\theta}\frac{\partial^2}{\partial\phi^2}\right)\right]\varphi_{J,m}(\theta,\phi) = E_{J,m}\varphi_{J,m}(\theta,\phi), \quad (4.12)$$

whose eigenvalues

$$E_{J,m} = \frac{\hbar^2}{2\mu r_e^2}J(J+1) \quad (4.13)$$

are obtained by considering the solutions $\varphi(\theta,\phi) = Y^{J,m}(\theta,\phi)$ where $Y^{J,m}(\theta,\phi)$ are spherical harmonics.

4.1.1.3 Correlation between rotational and nuclear spin states

The total nuclear spin $I = I_1 + I_2$ of H_2 can have two possible configurations, depending on weather the spins are *parallel* ($I = 1$) or *anti-parallel* ($I = 0$) with each other. $I = 1$, called *ortho* (o-H_2) is associated with three ($I_z = -1, 0, 1$) symmetric spin eigenfunctions, $\chi(I = 1) = |\uparrow,\uparrow\rangle, \frac{1}{\sqrt{2}}\left(|\uparrow,\downarrow\rangle + |\downarrow,\uparrow\rangle\right), |\downarrow,\downarrow\rangle$. $I = 0$, called *para* (p-H_2) is associated with the anti-symmetric spin eigenfunction $\chi(I = 0) = \frac{1}{\sqrt{2}}\left(|\uparrow,\downarrow\rangle - |\downarrow,\uparrow\rangle\right)$. There exists a correlation between the total nuclear spin I and rotational states of H_2. The total wavefunction of the nuclear motion has spatial and spin components, *i.e.*,

$$\Phi = \varphi_N(r, \theta, \phi)\chi(I). \tag{4.14}$$

We can decompose further the spatial part as $\varphi_N(r, \theta, \phi) = R(r)Y^{J,m}(\theta, \phi)$. If the spin part is symmetric, the spatial part must be anti-symmetric and vice versa. Since the two protons of H_2 are fermions and are indistiguishable, interchanging these particles should give an anti-symmetric spatial wavefunction. Particle interchange is ilustrated by the transformation of the polar and azimuthal angles as $\theta \to \pi - \theta$ and $\phi \to \pi + \phi$. Under the exchange of positions of the nuclei, the spatial wavefunction transforms as

$$Y^{J,m}(\theta, \phi) \to Y^{J,m}(\pi - \theta, \pi + \phi) \to (-1)^J Y^{J,m}(\theta, \phi), \tag{4.15}$$

$$R(r) \to R(r) \tag{4.16}$$

It is evident in the transformation (4.16) that the $R(r)$ component of the spatial wavefunction is invariant under particle exchange. The symmetric and antisymmetric properties of the spatial nuclear wavefunction shows in the angular component in (4.15). Even(odd) values of the angular momentum J correspond to (anti)symmetric $Y^{J,m}(\theta, \phi)$. The spatial part $\varphi_N(r, \theta, \phi)$ of the total wavefunction (4.14) must be symmetric for $I = 0$ since $\chi(I)$ is antisymmetric. Similarly, $\varphi_N(r, \theta, \phi)$ must be antisymmetric for $I = 1$ since $\chi(I)$ is symmetric. We can therefore establish the correlation between the rotational states J of H_2 with its total nuclear spin I as follows: Even(odd) Js correspond to $I = 0(1)$ or $p(o)$-H_2. This relationship is summarised in Figure 4.1. From the eigenenergies in Equation (4.13), we obtain two lowest energy states of o- and p-H_2 as $E^p_{J=0} = 0$ and $E^o_{J=1} = 2B$, where $B = \frac{\hbar^2}{2\mu r_e^2}$ is the rotational constant of H_2. The energy difference is calculated as $\Delta E_{o-p} = 14.7$ meV.

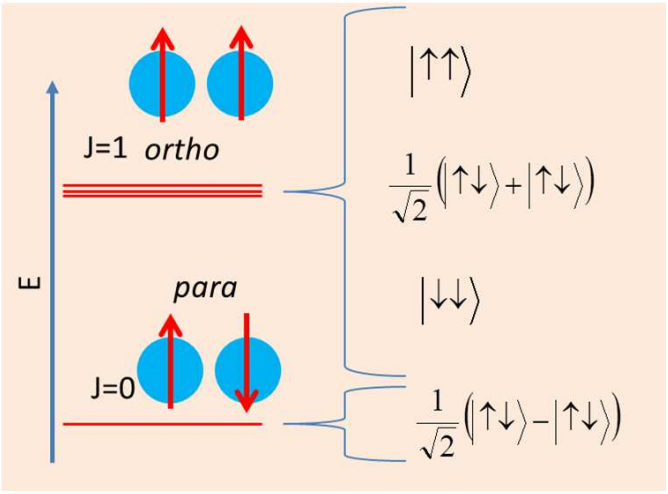

FIGURE 4.1: Rotational energy diagram of the two lowest J levels of free H_2 corresponding to ortho ($J = 1$) and para ($J = 0$) nuclear spin isomers. Ortho- and para-H_2 are associated with three degenerate symmetric (triplet) and anti-symmetric nuclear spin eigen functions, respectively.

4.1.2 Rotational states of H_2 adsorbing on a solid surface

We consider a model system depicted in Fig. 4.4 wherein an H_2 approaches the surface at different polar (θ) and azimuthal (ϕ) orientations. We may take the origin of the coordinate system to be the top of a specific adsorption site on the surface. Using this model, we re-express the six-dimensional (6D) Hamiltonian of Equation (4.9) that describes the quantum motion of H_2 on a surface as[93]

$$H_{6D} = -\frac{\hbar^2}{2M}\frac{\partial^2}{\partial X^2} - \frac{\hbar^2}{2M}\frac{\partial^2}{\partial Y^2} - \frac{\hbar^2}{2M}\frac{\partial^2}{\partial Z^2} - \frac{\hbar^2}{2\mu}\left(\frac{1}{r^2}\frac{\partial}{\partial r}r^2\frac{\partial}{\partial r} - \frac{1}{r^2}\mathbf{J}^2\right) + U\left(X, Y, Z, r, \theta, \phi\right), \quad (4.17)$$

where $\mathbf{J}^2 = \frac{1}{\sin\theta}\frac{\partial}{\partial\theta}\sin\theta\frac{\partial}{\partial\theta} + \frac{1}{\sin^2\theta}\frac{\partial^2}{\partial\phi^2}$, $M = m_1 + m_2$, $\mu = \frac{m_1 m_2}{m_1+m_2}$, and $U\left(X, Y, Z, r, \theta, \phi\right)$ is the relevant potential energy surface (PES) from the ground state energy of the electron system. This model completely describes all the degress-of-freedom (DoF) of H_2 as it approaches the surface, as long as the PES U is known. In this study we will be dealing with a system in which the nature of adsorption process may be sufficiently described by a fewer number of DoF. With this we will make use of the two limiting cases of interest: 1) the rational states of H_2 at the equilibrium bonding distance and 2) the effects of molecule-surface distance to the rotational motion of H_2.

4.1.2.1 H_2 hindered rotation when $U = U(X_e, Y_e, Z_e, r_e, \theta, \phi)$

We want to obtain a simple form of Equation (4.17) that allows us to calculate the rotational energies at the H_2-Pd(210) equilibrium bonding distance, Z_e by assuming the following: first, we write $r = r_e$ where r_e is the equilbirium H-H bond length obtained from ground state electronic calculations, and neglect its corresponding kinetic energy. This means our calculations are performed at the internal vibrational ground state of H_2. Then, we assume that our potential is azimuthally symmetric and the z component of J (m) is conserved. Next, we take the potential U to be a function of $\cos^2\theta$ and set $R = (X, Y, Z)$. We then perform a Taylor series expansion of the potential at $R = R_e$ and $\eta^2 = \cos^2\theta = 0$

$$U(R, \theta) = U(R_e) + \eta^2 \frac{\partial U}{\partial \eta^2} + (R - R_e)^2 \frac{\partial^2 U}{\partial R^2} + \cdots . \tag{4.18}$$

And lastly, we assume that H_2 remains in its equilibrium adsorption coordinates and ignore the effects of the molecule's motion along $\hat{x}$, $\hat{y}$ and $\hat{z}$ axes set their corresponding kinetic energies to zero. With this, we only consider the first two terms in the expansion (4.18), and neglect the higher order terms. We will justify this assumption in the following sections.

The 6D Hamiltonian in (4.17) finally becomes

$$H^m(\eta) = \frac{\hbar^2}{2\mu r_e^2}\left[\frac{\partial}{\partial \eta}\left(1 - \eta^2\right)\frac{\partial}{\partial \eta} - \frac{m^2}{1 - \eta^2}\right] + Q\eta^2, \tag{4.19}$$

where $Q = \frac{\partial U}{\partial \eta}$ = constant is the magnitude of the hindering potential of H_2 in the middle of the adsorption well for different polar orientations[94]. The corresponding wave function, $\Psi(\theta, \phi)$ can then be expressed as

$$\Psi(\theta, \phi) = \sum_{J,m} \langle \theta, \phi | J, m \rangle \langle J, m | \Psi \rangle, \tag{4.20}$$

where, $\langle \theta, \phi | J, m \rangle = Y^{J,m}(\theta, \phi)$ and $\langle J, m | \Psi \rangle = c_{J,m}$ are the spherical harmonics and expansion coefficients, respectively. To compute for the energy levels $E^{J,m}$, we fixed m and multiplied both sides of (4.19) with (4.22) and its complex conjugate then evaluated numerically the resulting expression within the framework of the variational method.

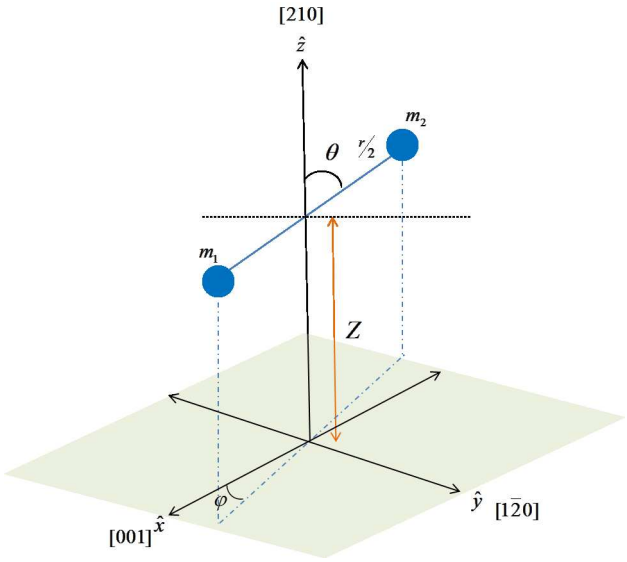

FIGURE 4.2: Model of H_2 adsorbing on Pd(210) surface. The $x-y$ plane corresponds to the surface plane made by [1$\bar{2}$0] and [001] axes. r, Z are the bond length and molecule's center of mass (CM)-surface distance. The molecular orientation with respect to the surface normal is given by θ and ϕ is azimuthal angle.

4.1.2.2 H_2 hindered rotation when $U = U\left(X_e, Y_e, Z, r_e, \theta, \phi\right)$

The corrugation of the surface described by X and Y components of the PES and the molecular internal vibration in principle are important to completely describe the quantum motion of H_2 adsorbing on a surface. However, obtaining the full 6D PES is oftentimes computationally demanding and cumbersome. In addition, these effects are often present at higher energy regimes and neglible if one is only concern about the dynamics at low temperatures. In this case, we assume that the molecule is confined at the equilibrium values of X, Y and r and express the PES as $U\left(X, Y, Z, r, \theta, \phi\right) = U\left(X_e, Y_e, Z, r_e, \theta, \phi\right)$. This assumption effectively neglects the corresponding kinetic energies along X, Y and r, and we may drop X_e, Y_e and r_e in U. The 6D Hamiltonian is then reduced to

$$H = -\frac{\hbar^2}{2M}\frac{\partial^2}{\partial Z^2} + \frac{\hbar^2}{2\mu r_e}\mathbf{J}^2 + U\left(Z, \theta, \phi\right). \tag{4.21}$$

$U\left(Z, \theta, \phi\right)$ may be obtained from electronic ground state total energy calculations. The eigen solutions of Hamiltonian (4.21) can be obtained expanding the wavefunction as

$$\Psi(Z, \theta, \phi) = \sum_{J,m,n} \langle \theta, \phi | J, m \rangle \ \langle Z | n \rangle \langle J, m, n | \Psi \rangle, \tag{4.22}$$

where, $\langle\theta,\phi|J,m\rangle = Y^{J,m}(\theta,\phi)$, $\langle Z|n\rangle = G_n(Z)$ and $\langle J,m|\Psi\rangle = c_{J,m,n}$ are the spherical harmonics, Gaussian functions and expansion coefficients, respectively. Similar to the previous section, we assume that U is azimuthally symmetric and the z component of the angular momentum m is conserved. The eigenvalues of (4.21) are calculated numerically for a given $U(Z,\theta,\phi)$ within the framework of variational method.

4.1.3 Nuclear spin isomers conversion of H_2 on a solid surface

To calculate the nuclear spin conversion of H_2 on a solid metal surface, we consider the adsorption model depicted in Figure 4.4. In this figure, H_2 is seen to be impinging the surface at the distance Z away (measured from the CM) and molecular orientation θ. At large Z, two electrons occupy the bonding orbital of H_2 and the metal surface is in the ground state $|F\rangle = c^\dagger_{k\sigma}c^\dagger_{k-\sigma}|0\rangle$ where $|0\rangle$ is the vacuum state, k is the surface electron Bloch states, and σ is the electron's spin. $c^\dagger_{k\sigma}(c^\dagger_{k-\sigma})$ is the single electron creation(annihilation) operator in the energy band of the metal surface with wave vector k. The Hamiltonian for the electrons of impinging H_2 molecule may be written as[95]

$$H_M = \sum_\sigma \varepsilon_a \left(a^\dagger_{1\sigma}a_{1\sigma} + a^\dagger_{2\sigma}a_{2\sigma}\right) + t\sum_\sigma \left(a^\dagger_{1\sigma}a_{2\sigma} + h.c.\right) + U_a\left(n_{1\uparrow}n_{1\downarrow} + n_{2\uparrow}n_{2\downarrow}\right) + J_a\left(n_{1\uparrow}+n_{1\downarrow}\right)\left(n_{2\uparrow}+n_{2\downarrow}\right) \quad (4.23)$$

where ε_a denotes the energy level of the electron in the localized orbital of atoms 1 and 2, t is the hybridization energy, U and J are the intra- and inter-atomic Coulomb interactions, respectively and $n_{i\sigma} = a^\dagger_{i\sigma}a_{i\sigma}$. $a^\dagger_{i\sigma}(a_{i\sigma})$ corresponds to the single electron creation(annihilation) operator in the orbital localized at $i = 1,2$ atoms. The metal surface Hamiltonian is given by the kinetic energy of the conduction electrons

$$H_S = \sum_{k\sigma} \epsilon_k c^\dagger_{k\sigma}c_{k\sigma}. \quad (4.24)$$

The electrons of substrate and H_2 are coupled through

$$H_{M-S} = \sum_\sigma \left[V_{11}(Z,\theta)a^\dagger_{1\sigma}c_{O_1\sigma} + V_{22}(Z,\theta)a^\dagger_{2\sigma}c_{O_2\sigma} + h.c.\right], \quad (4.25)$$

where $c_{O_1\sigma} = \frac{1}{\sqrt{N}}\sum_{k\sigma} c_{k\sigma}\exp\left(ik\frac{r}{2}\sin\theta\right)$ and $c_{O_2\sigma} = \frac{1}{\sqrt{N}}\sum_{k\sigma} c_{k\sigma}\exp\left(-ik\frac{r}{2}\sin\theta\right)$ are Warnier orbitals of the surface sites located nearest to atoms 1 and 2, respectively. r is

the H-H bond length and N is the number of lattice sites of the substrate. $V_{11}(Z,\theta)$ and $V_{22}(Z,\theta)$ are the hybridization potentials between the substrate and orbital electrons and are assumed to have exponential forms $V_{11} = V_0 u(Z)$ and $V_{22} = V_{11}\exp(-\gamma r\cos\theta)$, where γ is a parameter that determines Z dependence of the hybridization potentials and $u(Z) = \exp(-\gamma Z)$. We re-express H_{M-S} in terms of bonding and anti-bonding states as

$$H_{M-S} = \sum_{k\sigma}\left[V_{ak}(Z,\theta)c^\dagger_{a\sigma}c_{k\sigma} + V_{bk}(Z,\theta)c^\dagger_{b\sigma}c_{k\sigma} + h.c.\right], \tag{4.26}$$

where

$$V_{ak}(Z,\theta) = \frac{\sqrt{2}}{2\sqrt{N}}V_0 u(Z)\left[f_-(\theta)\cos\left(k\frac{r}{2}\sin\theta\right) + if_+(\theta)\sin\left(k\frac{r}{2}\sin\theta\right)\right], \tag{4.27}$$

$$V_{bk}(Z,\theta) = \frac{\sqrt{2}}{2\sqrt{N}}V_0 u(Z)\left[f_+(\theta)\cos\left(k\frac{r}{2}\sin\theta\right) - if_-(\theta)\sin\left(k\frac{r}{2}\sin\theta\right)\right], \tag{4.28}$$

$f_\pm(\theta) = 1 \pm e^{-\gamma r\cos\theta}$, $c^\dagger_{a\sigma} = \frac{1}{\sqrt{2}}\left(a^\dagger_{1\sigma} - a^\dagger_{2\sigma}\right)$ and $c^\dagger_{b\sigma} = \frac{1}{\sqrt{2}}\left(a^\dagger_{1\sigma} + a^\dagger_{2\sigma}\right)$. We assume that the electron and nuclear system are interacting via the hyperfine Fermi contact interaction

$$H_F = \sum_{k\sigma}\left[\Delta_{ak}(Z,\theta)c^\dagger_{a\sigma}c_{k'-\sigma} + \Delta_{bk}(Z,\theta)c^\dagger_{b\sigma}c_{k'-\sigma} + h.c.\right], \tag{4.29}$$

where

$$\Delta_{ak'}(Z,\theta) = \frac{\sqrt{2}}{2\sqrt{N}}\lambda\left[\Delta_-\cos\left(k'\frac{r}{2}\sin\theta\right) + i\Delta_+\sin\left(k'\frac{r}{2}\sin\theta\right)\right], \tag{4.30}$$

$$\Delta_{bk'}(Z,\theta) = \frac{\sqrt{2}}{2\sqrt{N}}\lambda\left[\Delta_+\cos\left(k'\frac{r}{2}\sin\theta\right) + i\Delta_-\sin\left(k'\frac{r}{2}\sin\theta\right)\right], \tag{4.31}$$

$\lambda = 5.9\times10^{-6}$ Å^3 is the Fermi contact constant, $\Delta_\pm = \Delta_1 \pm \Delta_2$, and Δ_1 and Δ_2 are given by

$$\Delta_1 = \left[\phi^*_1(\mathbf{R}_1)\varphi_1(\mathbf{R}_1) + \phi^*_1(\mathbf{R}_2)\varphi_1(\mathbf{R}_2)\right]\mathbf{S}_i\cdot(\mathbf{I}_1 - \mathbf{I}_2), \tag{4.32}$$

$$\Delta_2 = \left[\phi^*_2(\mathbf{R}_1)\varphi_2(\mathbf{R}_1) + \phi^*_2(\mathbf{R}_2)\varphi_2(\mathbf{R}_2)\right]\mathbf{S}_i\cdot(\mathbf{I}_1 - \mathbf{I}_2). \tag{4.33}$$

$\phi^*_i(\mathbf{R}_\alpha)\varphi^*_i(\mathbf{R}_\alpha)$ represents the overlap of the molecule orbitals ϕ_i and the metal surface orbitals φ_i at the molecule's nucleus located at $\mathbf{R}_\alpha$ ($\alpha = 1,2$). $\mathbf{S}_i$ is the spin of the ith electron of the molecule and the surface, and $\mathbf{I}_\alpha$ is the nuclear spin of αth nucleus. In calculating the $o-p$ transition probability, we consider a two-step process[55] described in Figure 4.3. Upon adsorption, one electron in the conduction band of the metal surface

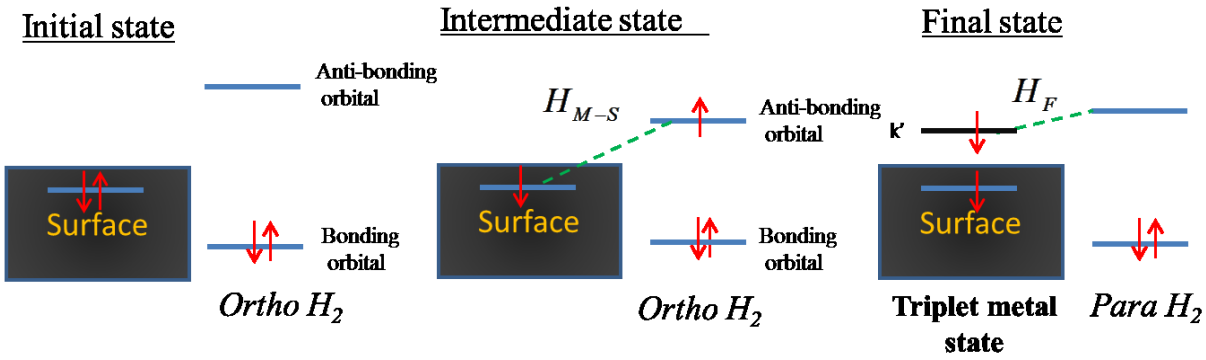

FIGURE 4.3: Mechanism or $o-p$ conversion on metal surfaces. The $\uparrow$ and $\downarrow$ shown in red denote electrons with up and down spins, respectively. The positions of the bonding and anti-bonding levels as well as the surface electrons states are not to scale.

with a wave vector k is excited to the antibonding state of the molecule, resulting to ionized metal and H_2^-. This virtual transfer of electrons is governed by H_{M-S}. In the next step, an electron in the anti-bonding orbital of H_2 transfers back to the metal in a state k' above the Fermi level, while simultaneously flips its spin, resulting in a triplet metal state. This process is governed by the H_F which induces the nuclear spin transition.

The initial state wave function is described by

$$|\Psi_i\rangle = |\Phi_i\rangle|\chi_i\rangle, \tag{4.34}$$

where

$$|\Phi_i\rangle = c^\dagger_{b\uparrow} c^\dagger_{b\downarrow} |F\rangle \tag{4.35}$$

is the initial state electronic wavefunction and $|\chi_i\rangle$ is one of the three o-H_2 ($I_z = -1, 0, 1$) nuclear spin eigenstates $|\uparrow,\uparrow\rangle$, $\frac{1}{\sqrt{2}}(|\uparrow\downarrow\rangle + |\downarrow,\uparrow\rangle)$ and $|\downarrow,\downarrow\rangle$. Similarly, the intermediate H_2-metal surface wave function is given by

$$|\Psi_p\rangle = |\Phi_p\rangle|\chi_p\rangle, \tag{4.36}$$

where

$$|\Phi_p\rangle = \frac{1}{\sqrt{2}} c^\dagger_{b\uparrow} c^\dagger_{b\downarrow} \left(c^\dagger_{a\uparrow} c_{k\uparrow} - c^\dagger_{a\downarrow} c_{k\downarrow} \right) |F\rangle, \tag{4.37}$$

and $|\chi_p\rangle = |\chi_i\rangle$. The final state is composed of a triplet metal surface and a neutral p-H_2 described by the wave function

$$|\Psi_f\rangle = |\Phi_f\rangle|\chi_f\rangle, \tag{4.38}$$

where

$$|\Phi_f\rangle = \frac{1}{\sqrt{2}} c^\dagger_{b\uparrow} c^\dagger_{b\downarrow} \left(c^\dagger_{k'\uparrow} c_{k\downarrow} + c^\dagger_{k'\downarrow} c_{k\uparrow} \right) |F\rangle, \tag{4.39}$$

and $|\chi_f\rangle = \frac{1}{\sqrt{2}} \left(|\uparrow\downarrow\rangle - |\downarrow,\uparrow\rangle \right)$. We employ second order perturbation theory to obtain the conversion rate from o-H_2 to p-H_2. The transition probability of this process is given by

$$P_{f\leftarrow i} = \frac{2\pi}{\hbar} \sum_{k,k'} \left| \frac{\langle \Psi_f | H_F | \Psi_p \rangle \langle \Psi_p | H_{M-S} | \Psi_i \rangle}{E_i - E_p} \right|^2 \delta \left(\epsilon_{k'} - \epsilon_k - \varepsilon_{op} \right), \tag{4.40}$$

where $E_i - E_p = \varepsilon_{M,i} + \epsilon_{S,i} - \varepsilon_{M,p} - \epsilon_{S,p}$. $\varepsilon_{M,i}$ and $\epsilon_{S,i}$ are the initial state energies of the isolated H_2 and the metal substrate, respectively. $\varepsilon_{M,p}$ is the resonance level corresponding to the anti-bonding state of H_2 upon adsorption, and $\epsilon_{S,p}$ is the metal substrate intermediate state energy level. We work out the matrix elements of Coulomb interactions in Equation (4.40) as

$$\langle \Psi_p | H_{M-S} | \Psi_i \rangle = \frac{2}{\sqrt{2}} V_{ak}(Z,\theta) \langle \chi_p | \chi_i \rangle \tag{4.41}$$

Similarly, the matrix elements of the hyperfine interactions are expressed as

$$\langle \Psi_f | H_F | \Psi_p \rangle = \frac{2}{\sqrt{2}} \tilde{\Delta}_{ak'}(Z,\theta) \left[1 - f(\epsilon_{k'}) \right], \tag{4.42}$$

where $f(\epsilon_{k'})$ is the Fermi-Dirac distribution function,

$$\tilde{\Delta}_{ak'}(Z,\theta) = \frac{\sqrt{2}}{2\sqrt{N}} \lambda \left[\tilde{\Delta}_- \cos\left(k' \frac{r}{2} \sin\theta \right) + i \tilde{\Delta}_+ \sin\left(k' \frac{r}{2} \sin\theta \right) \right], \tag{4.43}$$

$$\tilde{\Delta}_1 = \left[\phi_1^*(\mathbf{R}_1)\varphi_1(\mathbf{R}_1) + \phi_1^*(\mathbf{R}_2)\varphi_1(\mathbf{R}_2) \right] \langle \chi_f | \mathbf{S}_i \cdot (\mathbf{I}_1 - \mathbf{I}_2) | \chi_p \rangle, \tag{4.44}$$

$$\Delta_2 = \left[\phi_2^*(\mathbf{R}_1)\varphi_2(\mathbf{R}_1) + \phi_2^*(\mathbf{R}_2)\varphi_2(\mathbf{R}_2) \right] \langle \chi_f | \mathbf{S}_i \cdot (\mathbf{I}_1 - \mathbf{I}_2) | \chi_p \rangle, \tag{4.45}$$

and

$$\mathbf{S}_i \cdot (\mathbf{I}_1 - \mathbf{I}_2) = \langle \sigma_i | S_i^z | \sigma_i' \rangle (I_1^z - I_2^z) + \frac{1}{2} \left[\langle \sigma_i | S_i^+ | \sigma_i' \rangle \left(I_1^- - I_2^- \right) + \langle \sigma_i | S_i^- | \sigma_i' \rangle \left(I_1^+ - I_2^+ \right) \right]. \quad (4.46)$$

$|\sigma_i\rangle$ correspond to the spin eigen states of the metal substrate and molecule electrons. The spin operators A^+ and A^- $(A = S, I)$ are

$$A^{\pm} = A^x \pm iA^y. \quad (4.47)$$

The factor $1-f(\epsilon_{k'})$ appearing in (4.42) is due to the occupation of the $|k'\rangle$ electron state of the metal surface in the final state, which should be initially empty. The nuclear spin operators I_i^q $(q = z, +, -$ and $i = 1, 2)$ act only on $|\chi_p\rangle$ and $|\chi_f\rangle$ and their corresponding matrix elements are calculated as

$$\langle \chi_f | (I_1^z - I_2^z) | \chi_p \rangle = 1, \quad (4.48)$$

$$\langle \chi_f | \left(I_1^- - I_2^- \right) | \chi_p \rangle = -\frac{\sqrt{2}}{2}, \quad (4.49)$$

$$\langle \chi_f | \left(I_1^+ - I_2^+ \right) | \chi_p \rangle = 0. \quad (4.50)$$

4.2 Bound nuclear spin states of H_2 on Pd(210)

4.2.1 Background

Early physical models of surfaces are typically flat planes which represent a termination from the bulk structure along one of the Miller indices. These models were sufficient enough to describe the charge densities on surfaces[96] and the changes in the work function for different facets[97]. Further, these models also satisfactorily contributed in the formulations of surface thermodynamic conditions explaining Langmuir adsorption isotherms[98]. However, cleaving the crystal structure to form a surface results in the constant presence of surface irregularities such as steps and kinks. These surface imperfections have been found to play major roles in many catalytic reactions[99, 100] and partly on surface structure sensitivity of various catalytic processes[101]. For example, Auger electron spectroscopy and low energy electron diffraction study[102] have shown

that adsorbed oxygen concentration is far greater on the surface with kinks compared to other defects. However, it also has shown that kinks on surfaces reconstructs when heated to around 800 K whereas steps are found to be thermodynamically stable. This implies that during careful sample preparations which involve annealing of the surface, steps would tend dominate in concentration compared to other defects. Subsequent study[103] on the adsorption of H_2O on stepped Rhenium has shown that molecular dissociation can happen on step sites even at low temperature. It has also shown that H_2O appears to be in molecular structure when adsorbed on terraces even at higher temperatures. This implies that surface defects have greater catalytic reactivity compared to flat surfaces. The preferential adsorption/dissociation surface defect sites also holds true even for relatively larger sized molecules such as C_2H_4[104, 105]. In order to understand the mechanism of adsorption on surface defect sites, it is always useful to study both experimentally and theoretically the simplest possible model systems. To get rid of the complexity brought about by larger molecules, molecule-surface reactions are often sufficiently modelled by hydrogen adorption on metal surfaces.

4.2.1.1 H_2 adsorption on stepped metal surfaces

Models of H_2 adsorption on smooth and flat (transition) metal surfaces have found very low activation barrier[106] and in some cases none at all[107, 108] towards dissociation. On noble metals such as gold (Au) on the other hand, H_2 has been found to be not active towards dissociation on (111) and (100) facets[109]. These models suggest a correlation between the electronic properties of the metal surface and adsorption dynamics of the molecules. This correlation has been discussed in the so-called *d*-band model[110, 111] in which the position of the metal's *d*-bands or the average density of states (DOS) with respect to the Fermi level can in principle predict the reactivity of a certain surface. This model has shown that the closer the *d*-bands to the Fermi level, the more reactive the surface towards adsorption/dissociation. H_2 dissociation on nano-sized Au clusters on the other has been found to be activated[109]. Further, this study has shown that adsorbed dissociated atoms has significantly deformed the metal clusters. Nano clusters are rich in atomic edges or sites wherein the coordination number of the surface atoms are lesser compared to the flat facets. These low coordination number has been attributed to higher reactivity towards dissociation and oxidation of some diatomic molecules on Au clusters[112]. On stepped transition metal surfaces

such as nickel (Ni) and copper (Cu), H_2 has been identified to exist in stable molecular configuration[40, 41, 113]. Similarly, on Pd(210), another stepped surface, temperature programmed desorption (TPD) measurements[114, 115] have identified three atomic and two molecular adsorption configurations of hydrogen. These three atomic configurations of hydrogen has been supported subsequent DFT calculations[116] which showed that H_2 dissociates on a clean Pd(210). The study has also revealed that the top of the step-edge Pd atom is the most reactive among all adsorption sites on Pd(210). This has been attributed to the fact that the step-edge Pd atom has the least coordination number among all the other sites on the surface. Low coordination number implies smaller hybridizations among the *d*-orbitals of the step-edge Pd and it nearest neighbour atoms. These results in a narrower and localised *d* states compared to lower layered atoms as shown by the local DOS (LDOS). The LDOS of Pd atoms located in the lower layers with more nearest neighbours are more spread (delocalised) compared to the step-edge Pd. Therefore, the *d*-band centres of these sites are located farther away from the Fermi level and are associated with lower reactivity. This is the reason why the step-edge Pd is the most reactive site on Pd(210). It is interesting to note that these LDOS profiles approaches that of the bulk with increasing number of nearest neigbours. These effectively explains the higher reactivity observed in the nano-sized clusters. On the other hand, the adsorbed (dissociated) H atoms effectively block the dissociation channels, hindering further H_2 dissociation, or the so called, "self-poisoning" effect. From electronic structure standpoint, the presence of hydrogen atoms shift the *d*-band centre of the step-edge Pd atom to energies deep below the Fermi level, decreasing its reactivity towards dissociation, consequently allowing stable H_2 adsorption on Pd(210). This means that molecular H_2 adsorption can only happen on Pd(210) after the passivation of a layer of atomic hydrogen.

4.2.1.2 Nuclear spin states of H_2 on stepped metal surfaces

In the previous section, surface defects such as steps has been attributed to some interesting outcomes of surface molecules interactions. It was discussed that H_2 initially dissociates on stepped metal surface and after the atomic adsorption sites have been completely occupied, molecular adsorption can happen. These effects do not happen on idealised flat metal surfaces where H_2 has only two possible configurations: either weakly physisorbed or dissociated. One can take advantage of this strong step-edge

atom-molecule coupling to investigate other physical properties such as the rotational states of H_2 which are closely related to the total nuclear spin states. To do this one has to consider the orientation of the molecule as it adsorbs on the stepped surface. It has been known that molecule-surface reactions are typically orientation dependent processes (see ref[117] and the references therein for a comprehensive review) which should also hold true for molecular H_2 adsorption on metal surfaces. Additionaly, it has already been shown[40, 41] that bound H_2 on Cu(510) is confined as a two-dimensional (2D) quantum rotor on top of step-edge Cu atoms due to large anisotropic adsorbate-surface potential. This hindering of rotational motion along the polar orientation is associated with the differential adsorption on the surface of the two nuclear spin (I) isomers ($I = 0, para$ and $I = 1, ortho$) of H_2[42, 43]. This also means that $ortho(o)$- and $para(p)$-H_2 can now be separated[42–50], an essential step to efficiently store liquid hydrogen. Much of these methods[42, 44, 46–48, 51] of separation involve chromatographic techniques that measure the retention times of o- and p-H_2 on activated alumina columns, and reports on $o-p$ separation using metal catalysts are lacking. In this paper, we report a possible separation of the two nuclear spin isomers of H_2 adsorbed on top of the step-edge of Pd atoms of Pd(210) that is passivated by a layer of pre-adsorbed atomic H. The relatively strong step-edge Pd-H_2 interaction restricts the molecule's polar rotation, resulting to the preferential adsorption of o-H_2.

4.2.2 Hindered rotation at H_2Pd(210) equilibrium bonding distance

We considered a model system depicted in Fig. 4.4 wherein an H_2 approaches the surface along the [210] direction perpendicular to $[001] \times [1\bar{2}0]$ plane at different polar (θ) and azimuthal (ϕ) orientations. We took the origin of the coordinate system to be the top of the step-edge Pd atom. Using this model, the quantum motion of H_2 on Pd(210) can be described by Hamiltonian (4.19)

$$H^m(\eta) = \frac{\hbar^2}{2\mu r_e^2}\left[\frac{\partial}{\partial\eta}\left(1-\eta^2\right)\frac{\partial}{\partial\eta} - \frac{m^2}{1-\eta^2}\right] + Q\eta^2. \tag{4.51}$$

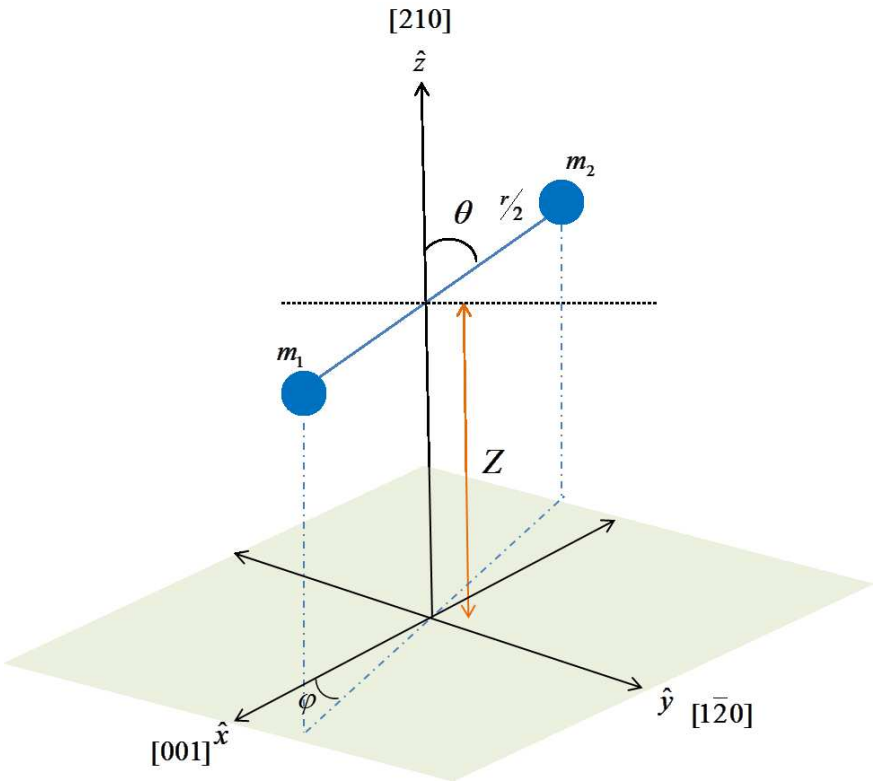

FIGURE 4.4: Model of H_2 adsorbing on Pd(210) surface. The $x-y$ plane corresponds to the surface plane made by [1$\bar{2}$0] and [001] axes. r, Z are the bond length and molecule's center of mass (CM)-surface distance. The molecular orientation with respect to the surface normal is given by θ and ϕ is azimuthal angle.

4.2.2.1 Potential energy curves and anisotropic potential

Our total energy calculations (discussed in Appendix B) of H_2 adsorption on different sites on Pd(210) surface with different coverages of atomic H ($\Theta = 1/3, 2/3, 1$ ML), revealed that the most stable site for molecular adsorption is on top of the step-edge Pd atom. This is consistent with the previous study[116]. We note that this preferential adsorption on the step-edge atom also holds true even for larger molecules such as C_2H_4 adsorbing on other stepped metal surface (Cu) with the same facet and is attributed to the blocking of the step atoms of other reactive sites[104]. We show the potential energy curves (PEC) for different θ, ϕ and Θ in Fig. 4.5. We can clearly see that the most energetically favorable H_2 adsorption molecular orientation is when $\theta = \pi/2$ and $\phi = 0, \pi/2$ for $\Theta = 1/3$ and $2/3$ ML. We shall henceforth call this configuration *parallel*-H_2, since the molecule sits parallel to the plane formed by [1$\bar{2}$0] and [001] in Fig. B.1; the opposite shall be *perpendicular*-H_2. The adsorption energy, ($\Theta = 1/3$ ML), E_{ads} for *parallel*-H_2 is -241 meV and the molecule-surface bonding distance is quite short, *ca.* 1.90 Å. After geometry optimizations, we find the adsorption well

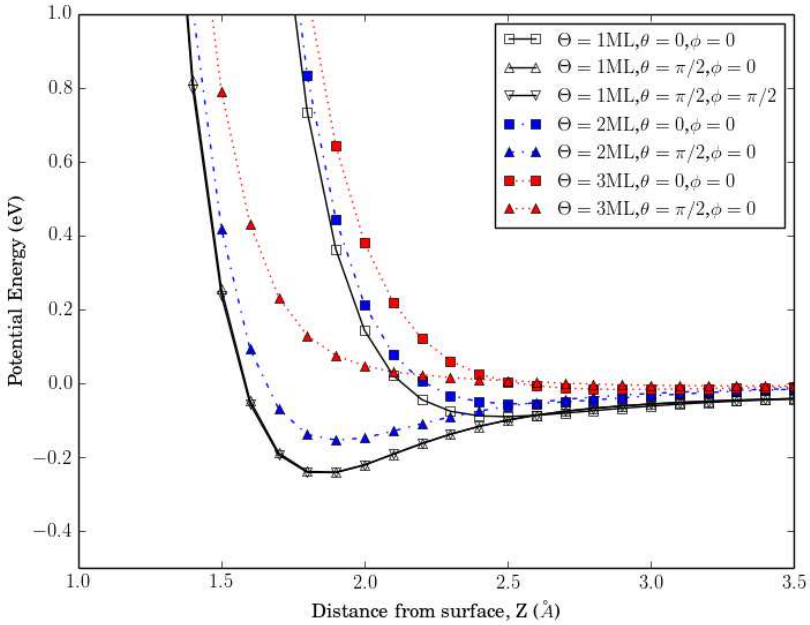

FIGURE 4.5: Potential energy curves (PEC) of H_2 adsorbing on the top of step-edge Pd atom of Pd(210) surface for different molecular orientations and coverages of atomic H ($\Theta = 1/3, 2/3, 1$ ML). $\theta = 0$ and $\theta = \pi/2$ correspond to H_2 oriented parallel and perpendicular to the plane made by $[1\bar{2}0]$ and [001] (cf. Fig.B.1).

minimum at 1.80 Å with a depth of 300 meV. Furthermore, the H_2 bond length is found to be elongated by around 0.071 Å ($r_e = 0.81$ Å) with respect to its equilibrium gas phase value, indicating that the antibonding orbital of H_2 is populated. This H-H bond elongation and closer surface-molecule distance suggest that the GGA is sufficient enough to describe the adsorption potential and the correlation effects (van der Waals attractive forces) are insignificant in the bond making process[41]. We note, that from Fig.4.5, we can see that the potential curves for $\theta = \pi/2$, $\phi = 0$ and $\theta = \pi/2$, $\phi = \pi/2$ are almost degenerate. We confirm this by performing total energy calculations of H_2 at the equilibrium surface-molecule distance, Z_e for different values of the azimuthal angle, while artificially freezing θ at $\pi/2$. Our results show a very small energy difference (≈ 0.2 meV) between $\theta = \pi/2$, $\phi = 0$ and $\theta = \pi/2$, $\phi = \pi/2$. This means that the ϕ motion is essentially free and the rotation is only hindered along θ. To see the effects of surface corrugation, we plot in Fig. 4.6a the contour of the potential energy surface computed for *parallel*-H_2 along the $x - z$ plane. The bottom of the potential well is located at $X = X_e = 0, Z = Z_e = 1.9$ Å, or the top of the step-edge Pd atom, with a depth of -241 meV. As we go away (increasing X) from the step-edge Pd, this potential gradually increases and peaks at the top of the pre-adsorbed atomic H (Figure 4.6(b)),

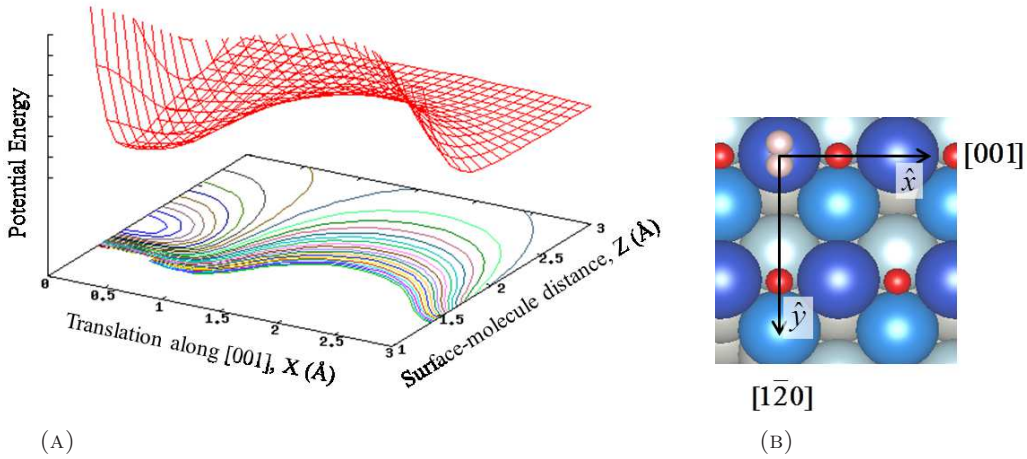

(A) (B)

FIGURE 4.6: (a) Contour plot of the potential energy surface along the $x - z$ plane. (b) top view of H_{1ML}/Pd(210) showing the calculation path along $\hat{x}$ axis.

Mode	Energy (meV)
$\rightarrow$ $\leftarrow$ (Internal vibration)	404
$\uparrow\downarrow$ ($\hat{y}$ rotation)	152
$\uparrow\uparrow$ ($\hat{z}$ translation)	96.4
$\leftarrow\leftarrow$ ($\hat{x}$ translation)	31.2
$\otimes\otimes$ ($\hat{y}$ translation)	23.3
$\otimes\odot$ ($\hat{z}$ rotation)	19.4

TABLE 4.1: Vibrational modes and their corresponding energies of H_2 adsorbed at the step-edge Pd atom of Pd(210) for $\Theta = 1/3$ ML. The symbols used for vibrational modes depict the motion of H_2 as viewed from the *haty* axis. The energy values are in meV.

then decreases again up to the next step-edge atom. We estimated the barrier of the movement of H_2 from the top of step-edge Pd to another step-edge atom as ≈ 500 meV. We can therefore think of H_2 to be well localized within the equilibrium position X_e and expect similar arguments for the Y and Z translations. This justifies our assumption of neglecting the higher order terms of expansion (4.18). We present in Table 4.1 the calculated vibrational modes of H_2 adsorbed at Z_e distance from the top of the step-edge Pd atom using harmonic approximation. We find that the internal vibrational energy is 404 meV, an order of magnitude larger than the translational modes along $\hat{x}$, $\hat{y}$ and $\hat{z}$ directions. The rotation along $\hat{y}$ also has a large energy of 152 meV, localizing the H_2's polar orientation at $\theta = \pi/2$. On the contrary, we obtained an energy of 19.4 meV for the rotation along $\hat{z}$ which is insufficient to localize the H_2 orientation at $\phi = \pi/2$, consistent with our total energy computations.

When the coverage of pre-adsorbed hydrogen atoms on the surface is increased to

$\Theta = 2/3$ ML, we find very similar adsorption characteristics of H_2 with that of the $\Theta = 1/3$ ML case. The only difference is the shallowing of the depth of the adsorption potential wells for both *parallel-* and *perpendicular*-H_2 (*cf.* Fig. 4.5). We also find that the positions of the adsorption energy minima (surface-molecule bond) are unchanged from the $\Theta = 1/3$ ML, indicating that the presence of another hydrogen atom only weakens the molecule-surface interactions. When we further increased the atomic coverage to $\Theta = 1$ ML, we find very shallow adsorption potential wells for both molecular orientations in the PEC (red dotted lines in Fig. 4.5). From this we obtained $V(R_e)$ as -241 and -150 meV for $\Theta = 1/3$ and $\Theta = 2/3$ ML, respectively. We note that $H_2/H_{1ML}/Pd(210)$ corresponds to a configuration which is way below the γ_1 and γ_2 molecular state peaks in the TPD measurements of ref[115] and therefore readily desorbs at very low temperatures. Since we are interested only in the rotational states of the two metastable molecular thermal desorption peaks, we will neglect this configuration in the computations of rotational states in the following.

While adsorbed on $H_{nML}/Pd(210)$, the H_2-surface interaction hinders its rotational (θ) motion with potential strength described by Q, which confines the molecular rotation to 2D. From the PEC in Fig. 4.5 we obtained Q as 603 and 594 meV for $\Theta = 1/3$ and $\Theta = 2/3$ ML, respectively. These values differ only by 9 meV because aside from the relative sizes of the Pd atoms and H_2 the position of the two pre-adsorbed H atoms in $\Theta = 2/3$ ML are located just below the step-edge Pd atom of $H_{2/3ML}/Pd(210)$ and do not significantly change the electronic charge density profile of the surface and its corresponding corrugation in the neigborhood of R_e.

4.2.2.2 H_2 nuclear spin isomers separation

Table 4.2 shows the computed rotational energies. In the calculations, we assumed a system at liquid hydrogen temperatures (< 20 K) so that only the lowest J levels are important.

The rotational energies of H_2 for $J = 0$ (*para*), $J = 1, m = 0$ (*ortho*) and $J = 1, m = \pm 1$ (*ortho*) states are 60.9, 186 and 68.7 meV, respectively for $\Theta = 1/3$ ML. We can clearly see the splitting of rotational energy levels of *o*-H_2 that are otherwise degenerate in the gas phase at thermal equilibrium. On the other hand, the rotational energy levels of H_2 for the case of $\Theta = 2/3$ ML are 60.4, 184 and 68.2 for $J = 0$ (*para*), $J = 1, m = 0$ (*ortho*)

Coverage (ML)	State	$E^{J,m}$ (meV)	$E^{J,m}_{ads}$ (meV)
$\Theta = 1/3$	$J = 0$	60.9	-180
	$J = 1, m = 0$	186	-55.0
	$J = 1, m = \pm 1$	68.7	-172
$\Theta = 2/3$	$J = 0$	60.4	-89.6
	$J = 1, m = 0$	184	34.41
	$J = 1, m = \pm 1$	68.2	-81.8

TABLE 4.2: Rotational, $E^{J,m}$ and adsorption $E^{J,m}_{ads} = E^{J,m} + V(R_e)$ energies, of H_2 for different Θ of pre-adsorbed H atoms on Pd(210) surface.

and $J = 1, m = \pm 1$ (*ortho*), respectively which are smaller compared to the $\Theta = 1/3$ ML. This is due to a decrease in the hindering potential Q with an increase of the pre-adsorbed atomic H. Furthermore, p- has higher adsorption energy for both $\Theta = 1/3$ and $\Theta = 2/3$ ML compared to o-H_2. We also investigate the thermal desorption of $o-$ and $p-H_2$ on H_{nML}/Pd(210). We defined the desorption energy $E^{J,m}_{des}$ as the magnitude of the difference between the adsorption energy level $E^{J,m}_{ads}$ of different J and m states with their corresponding rotational energies $E^{J,m}_{g}$ in the gas phase (free rotor)[118],

$$E^{J,m}_{des} = E^{J,m}_{g} - E^{J,m}_{ads} \tag{4.52}$$

The desorption energies are $E^{J=0}_{des} = 180$ meV ($p-$), $E^{J=1,m=0}_{des} = 69.0$ meV ($o-$) and $E^{J=1,m=\pm1}_{des} = 187$ meV ($o-H_2$) for $\Theta = 1/3$ ML. In a similar manner, we obtained $E^{J=0}_{des} = 89.6$ meV ($p-$), $E^{J=1,m=0}_{des} = -19.7$ meV ($o-$) and $E^{J=1,m=\pm1}_{des} = 96.5$ meV ($o-H_2$) for $\Theta = 2/3$ ML. The negative sign of $E^{J=1,m=0}_{des}$ means that this state is no longer bound to the surface due to its very large (184 meV) rotational energy compared to the potential energy well depth at $\Theta = 2/3$ ML. From these values of $E^{J,m}_{des}$ we can see that $o-$ has higher desorption energy than $p-H_2$ for both coverages. For example, the difference between the desorption energies of the bound $o-$ and $p-H_2$ ($\delta^{o-p} = E^{J=1}_{des} - E^{J=0}_{des}$) are 7.0 and 6.9 meV for $\Theta = 1/3$ and $\Theta = 2/3$ ML, respectively. These values are larger compared to H_2 physisorbed on Ni(111)[118] due to the stronger surface-molecule interaction in H_2/H_{2ML}/Pd(210). We note further that an angular momentum analysis of the two molecular peaks (γ_1 and γ_2) in the TPD spectra of refs[114, 115] should reveal two peaks separated by a few Kelvin corresponding to the differences in the

desorption energies of o and p isomers of H_2 on Pd(210). This is indeed the case as confirmed by a recent resonance multiphoton ionization (REMPI)-TPD experiment[**?**] on H_2 adsorption on Pd(210). In this study, $o{-}H_2$ has been found to desorb at a higher temperature compared to $p{-}H_2$, with $\delta^{o-p} \approx 17$ meV.

4.2.3 Dynamics of nuclear spins of H_2 in a 2D PES

4.2.3.1 Hamiltonian

We may describe the quantum motion of H_2 as it impinges the Pd(210) by the full 6D Hamiltonian (4.17). However, we make use of the assumptions made in the previous section, the dynamics of the molecular motion may be described by the effective 3D Hamiltonian (4.21)

$$H = -\frac{\hbar^2}{2M}\frac{\partial^2}{\partial Z^2} + \frac{\hbar^2}{2\mu r_e}\mathbf{J}^2 + U\left(Z,\theta,\phi\right). \tag{4.53}$$

As in the previous section, the adsorption of H_2 on Pd(210) is azimuthally independent. By introducing the exact quantum number m, the 3D eigenfunctions can be expressed as

$$\Psi(Z,\theta,\phi) = \sum_{J,m,n} e^{im\phi}\Phi_{Jmn}(Z,\theta), \tag{4.54}$$

where

$$\Phi(Z,\theta) = c_{J,m,n}G_n(Z)\sqrt{\frac{(2J+1)\,(J-m)!}{4\pi\,(J+m)!}}P_J^m(\cos\theta), \tag{4.55}$$

and $P_J^m(\cos\theta)$ are the associated Legendre polynomials. From this the corresponding 2D Hamiltonian reads

$$H_{2D} = -\frac{\hbar^2}{2M}\frac{\partial^2}{\partial Z^2} + \frac{\hbar^2}{2\mu r_e}\left(-\frac{1}{\sin\theta}\frac{\partial}{\partial\theta}\ \sin\theta\frac{\partial}{\partial\theta} + \frac{m^2}{\sin^2\theta}\right) + U_{2D}\left(Z,\theta\right). \tag{4.56}$$

We evaluate the eigenvalues of this Hamiltonian using the basis function $\Phi(Z,\theta)$ where we used the Gaussian-type wavefunctions of the form

$$G_n(Z) = \left(\frac{\beta}{\pi}\right)^{1/4}\exp\left[-\beta\left(Z-z_n\right)\right]. \tag{4.57}$$

The parameter β is adjusted to account for sufficient overlap between the nearest neighboring wavefunctions and n labels the nth Gaussian-type orbital centered at z_n.

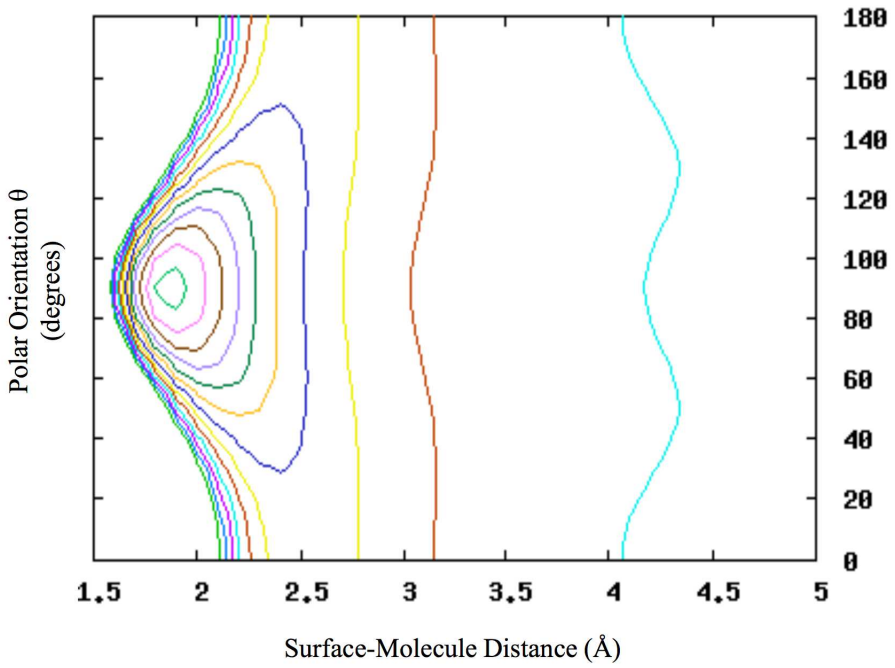

FIGURE 4.7: 2-dimensional (2D) potential energy surface describing H_2 adsorption on top of stepped Pd atom of Pd(210) for different surface-molecule distance, Z and polar angle θ. This 2D PES is calculated for $\Theta = 1/3$ ML.

4.2.3.2 2D Potential energy surface: $U_{2D}(Z, \theta)$

We construct the 2D adiabatic potential energy surface (PES), $U_{2D}(Z, \theta)$ from total energy calculations scheme in DFT described in the previous section. In the computations, we determined the total energy at different values of the CM positions, Z and polar orientation, θ and the coverage of pre-adsorbed atomic H $\Theta = 1/3$ ML. The contour representation of this 2D PES is shown in Figure 4.7. This PES has a minimum at $(Z = 1.9\text{Å}, \theta = \pi/2)$. It is highly anisotropic in the sense that the adsorption is favored towards parallel-H_2 than perpendicular-H_2. We may obtain an analytical form of this potential by fitting with the 2D Morse potential-like function

$$U_{2D}(Z, \theta) = D(\theta)\{[\exp[-\alpha(\theta)(Z - Z_e(\theta))] - 1] - 1\}. \tag{4.58}$$

$D(\theta)$, $\alpha(\theta)^{-1}$ and $Z_e(\theta)$ describe the potential well depth, the potential well width and the equilibirium bonding distance between H_2 and step-edge Pd atom. From the fitting, we found that $D(\theta) = V_0 \cos^2\theta$ where $V_0 = D_{\theta=0} - D_{\theta=\pi/2}$. Here we recovered the anisotropic potential Q in the previous section when we neglect the molecular vibration with respect to the H_2 CM-step-edge Pd atom distance Z. Figure 4.7 shows that U

n	E_n (meV)	E_{des} (meV)	Rotational State	Spin State
0	-202.3	202.3	$J=0, m=0$	para
1	-197.6	212.3	$J=1, m=1$	ortho
2	-183.5	44.1	$J=2, m=2$	para
3	-170.2	170.2	$J=0, m=0$	para

TABLE 4.3: Rotational eigen energies, nuclear spin states and desorption energies of H_2 adsorbing on top of step-edge Pd atom of Pd(210). The calculations are done for $\Theta = 1/3$ ML.

is highly symmetric with respect to θ and can be effectively described by the following minimal 2D potential function

$$U_{2D}\left(Z,\theta\right) = U_{\pi/2}(Z) + \left[U_0(Z) - U_{\pi/2}(Z)\right]\cos^2\theta, \tag{4.59}$$

where $U_{\pi/2}(Z) = D_{\pi/2}\left\{\left[\exp\left[-\alpha(\theta=\pi/2)\left(Z - Z_e(\theta=\pi/2)\right)\right] - 1\right] - 1\right\}$ and similar expression for $U_0(Z)$. We make a substitution of (4.59) into (4.56) and multiply the resulting expression with $\Phi(Z,\theta)$ and its complex conjugate. We diagnolalize numerically the resulting secular matrix within the framework of variational method.

4.2.3.3 Nuclear spin bound states

We present in Figure (4.8) the calculated wavefunctions for the ground, first excited and third excited states, respectively. Since the angular momentum quantum number J is no longer a good quantum number in our calculations, its values are mixed and it is not possible to calculate the eigenvalues for a definite and specific J. We therefore assign the rotational state by taking the J values with the highest contribution in the expansion coefficients $c_{J,m,n}$ of $\Phi(Z,\theta)$. The ground state energy is $E_0^{J=0,m=0} = -202.3$ meV and its wavefunction displayed in Figure 4.8a has a para ($J=0$) character and is localized at $Z = 1.9$ Å, $\theta = \pi/2$. The corresponding desorption energy $E_{0,des}^{J=0,m=0} = 202.3$ meV. Similarly we find the 1st excited state energy as $E_1^{J=1,m=1} = -197.6$ meV and its wavefunction in Figure 4.8b has an ortho ($J=1$) character with the same localization points as in the para case. We calculate the desorption energy of this state as $E_{0,des}^{J=0,m=0} = 212.3$ meV. We summarized these results in Table 4.3. The energy difference between o- and p-H_2 $\delta^{o-p} = 10$ meV. The desorption peaks corresponding to these desorption energies are $T_{J=0} = 78$ K and $T_{J=1} = 82$ K. From the profile of the square of the wavefunctions of these states, we found that they correspond to $\nu = 0$ of

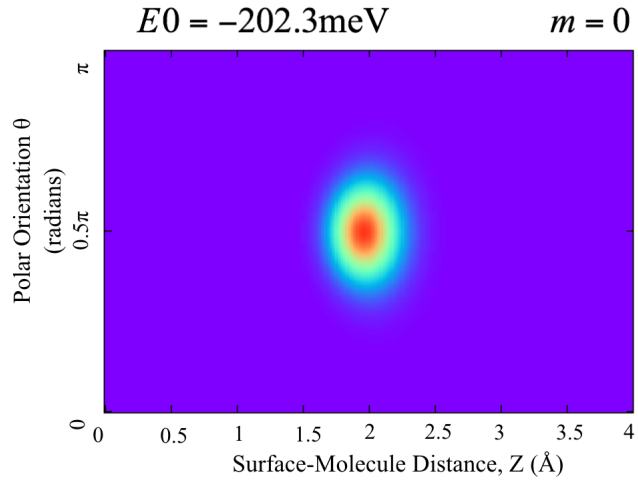

(A)

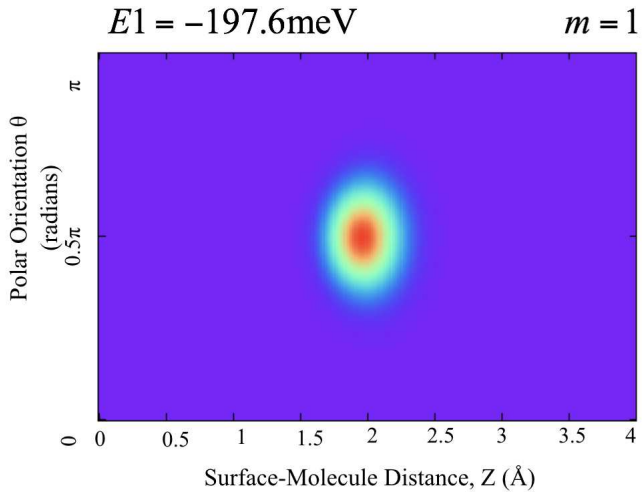

(B)

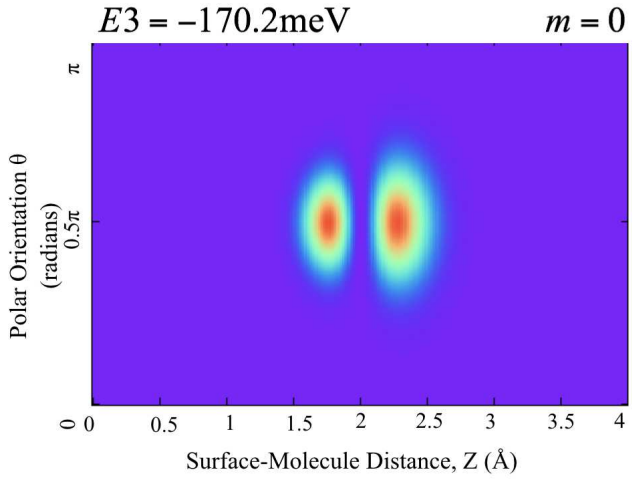

(C)

FIGURE 4.8: (a) Ground state wavefunction, $J = 0, m = 0$. (b) 1st excited state wavefunction, $J = 1, m = 1$. (c) 3rd excited state wavefunction $J = 0, m = 0$

the Morse potential function. We identified the dominant angular momentum quantum number of the 2nd excited state as $J = 2$ and at energy level $E_{0,des}^{J=2,m=2} = -183.6$ meV. Its wavefunction has a node along θ and still localized at $Z = 1.9$ Å along the Z direction. We show the 3rd excited state wavefunction in Figure 4.8c. We found $J = 0$ as the dominant rotational state of this wavefunction whose energy level is at $E_3^{J=0,m=0} = -170.2$ meV (para-H_2). If we look closely at the profile of the wavefunction of this state, we can clearly see a node along the Z direction. Further, the lobes of this wavefunction are asymmetric along Z in resemblance with the $\nu = 1$ state of the one-dimensional (1D) Morse potential schematically shown in Figure for $\nu = 0, 1, \cdots, 5$. In the inset, we show the plot of 3rd excited state, $\Phi(Z, \theta)$ along the Z. This asymmetry in the rotational state wavefunction can be traced back to the anharmonicity of the 2D Morse-like potential function (4.59). It is worth mentioning that the wavefunctions are

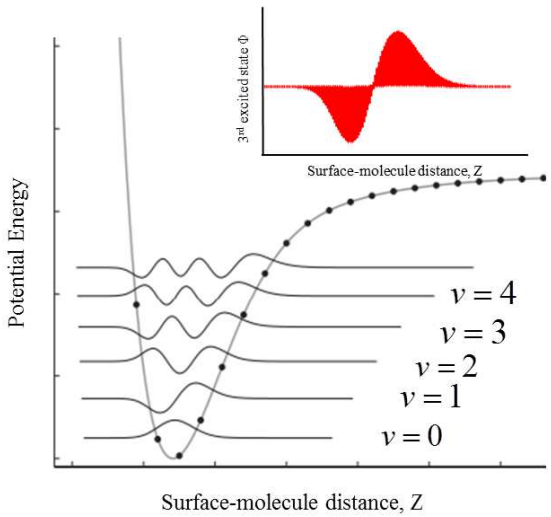

FIGURE 4.9: Schematic diagram of vibrational states of the Morse potential. The inset shows the plot of $\Phi(Z, \theta)$ along Z.

rather symmetric along θ. From the contour plot of our calculated 2D PES, we can clearly see that our potential is harmonic in θ direction. This results to the symmetric component of the wavefunctions along θ as shown by the lobes in Figure 4.8. We present in Figure 4.10 the wavefunction (upper panel) associated with the energy level -121.5 meV. From the plot of the contributions (in %) of J to the expansion coefficient, we can assign this state to be para-H_2 with $J = 1$ character. The node located at $Z \approx 2.0$ Å shows that this wavefunction has $\nu = 1$ character similar to that in Figure 4.9. We can therefore assign this state as $(\nu, J, m) = (1, 1, 0)$. We note that the quantum number n

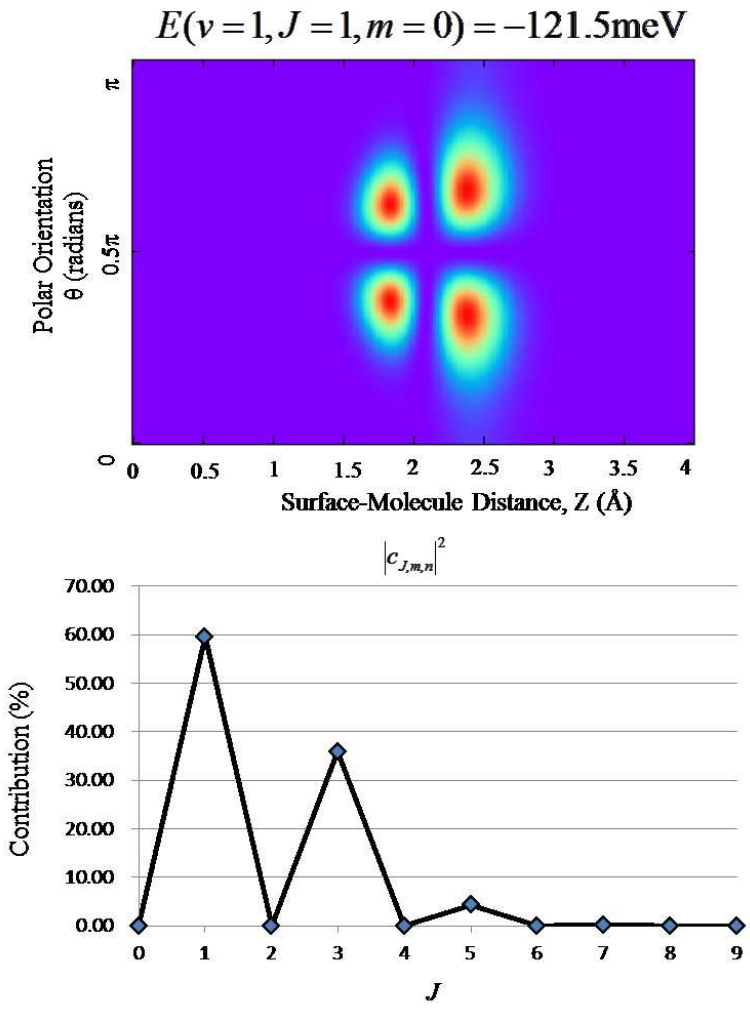

FIGURE 4.10: (Upper panel) shows the 2D plot of the probability density $|\Phi(Z,\theta)|^2$ of the wavefunction for energy level -121.5 meV. The lobes of this wavefunction are highly symmetric along θ and asymmetric along Z. Each direction has a node located in the Z at $Z \approx 2.0$ Å and in θ at $\theta \approx \pi/2$. (Lower panel) shows the contribution (in %) of individual angular momenta J to the expansion coefficient $|c_{J,m,n}|^2$. Only odd numbered J have non-vanishing contributions to $|c_{J,m,n}|^2$, therefore we identify this state as ortho-H_2.

labels the eigenvalues $E_n^{J,m}$ in increasing order and do not characterize the vibrational state of H_2 on the surface. These vibrational states must be decided based on the nodes and the profiles of the wavefunctions. We summarized in Table 4.4 the rotational and vibrational energy levels of H_2 on Pd(210). Our analysis technique is consistent with the solutions of the rotational-vibrational (rot-vibro) Morse oscillator in which different vibrational states ν exist at different energy levels and different rotational states J.

$m=0$		$m=1$		$m=2$	
(ν, J, m)	Energy (meV)	(ν, J, m)	Energy (meV)	(ν, J, m)	Energy (meV)
$(0,0,0)$	-202.3	$(0,1,1)$	-197.6	$(0,2,2)$	-183.5
$(1,0,0)$	-170.2	$(1,1,1)$	-165.5	$(1,2,2)$	-151.2
$(0,1,0)$	-150.0	$(0,2,1)$	-143.8	$(0,3,2)$	-126.3
$(2,0,0)$	-140.8	$(2,1,1)$	-135.9	$(2,2,2)$	-121.5
$(1,1,0)$	-121.5	$(1,2,1)$	-114.8	$(1,3,2)$	-96.70
$(3,0,0)$	-114.0	$(3,1,1)$	-109.0	$(3,2,2)$	-94.40

TABLE 4.4: Rotational-vibrational energy levels of H_2 adsorbing on the top of step-edge Pd atom of Pd(210).

Rotational State (J)	Composition (in %) Exp[120]	Composition (in %) Theory
0 (*para*)	35.7	42.8
2 (*para*)	19.1	19.9
4 (*para*)	10.4	2.32
1 (*ortho*)	25.2	29.2
3 (*ortho*)	6.40	4.52
5 (*ortho*)	3.20	0.35

TABLE 4.5: Comparison between experimental and theoretically obtained rotational state J compositions.

4.2.3.4 Comparison with experiment

Temperature programmed desorption (TPD) spectroscopy and rotational state-resolved resonance enhanced multiphoton photo-induced (REMPI) desorption are powerful tools in quantum state-specific detection of atoms and molecules scattering on a solid surface as well as in studying the dynamics of desorption on surfaces. REMPI has been successfully used in studying nuclear spin flipping of H_2 on solid ice[119] by direct rotationally-resolved detection of desorbing molecules. Combined TPD-REMPI has also been used to clarify the mechanisms of ortho-para conversion of H_2 physisorbed on Ag(111)[57]. Recent REMPI experiment[120] on the quantum dynamics of H_2 under the influence of highly anisotropic adsorption potential on Pd(210) have measured the concentration of desorbing molecules based on their rotational states. They found that the desorbing H_2 is composed of 65.2% p-H_2 and 34.8% o-H_2. Based from our analysis of the J contributions to the expansion coefficient of the rotational wavefunctions, we are able to compare the composition of each J in the experiment with the ones obtained by our calculations in Table 4.5. Theoretical values in the table are obtained from expansion coefficients of

the ground (p-H_2) and 1st excited (o-H_2) states wavefunctions, respectively.

4.2.4 Isotope effects

We also investigated the isotope effects on the quantum dynamics of H_2 nuclear spin states on Pd(210). The deuterium molecule (D_2) nuclear spin states are $I = 1$ (p-D_2) and $I = 0$ (o-D_2) which correspond to odd and even J, respectively. We show

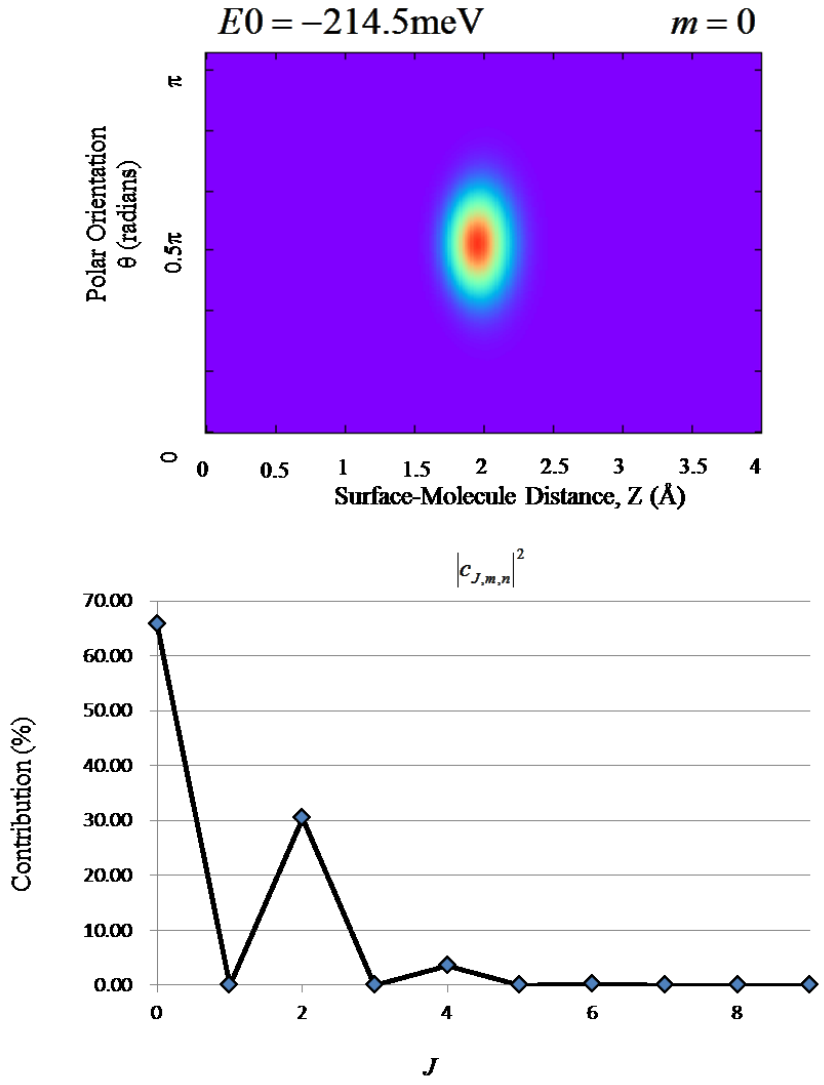

FIGURE 4.11: (Upper panel) shows the 2D plot of the probability density $|\Phi(Z,\theta)|^2$ of the wavefunction of $\mathbf{D_2}$ for energy level -214.5 meV. (Lower panel) shows the contribution (in %) of individual angular momenta J to the expansion coefficient $|c_{J,m,n}|^2$. Only even numbered J have non-vanishing contributions to $|c_{J,m,n}|^2$, therefore we identify this state as ortho-$\mathbf{D_2}$.

in Figure 4.11 the ground state wavefunction of D_2 with an energy level $E_0 = -214.5$ meV. This wavefunction has an ortho character with only the even J values are the

non-vanishing terms in the expansion coefficient. The largest contribution comes from $J = 0$. Although not clearly seen in the figure, this wavefunction has more degree of localization compared to H_2. This should be expected due to the larger mass of D_2 compared to H_2. The first excited state energy level is $E_1 = -214.5$. This state has a para character and the largest contribution to the expansion coefficient comes from $J = 1$. We found a significant difference of 12.2 meV of the rotational-vibrational (rot-vibro) energies of H_2 and D_2. The ratio $\frac{E_{D_2}}{E_{H_2}} = 1.06$. If we consider the zero point energies (ZPE) of the two isotopes, we find a much larger energy difference and ratio. In determining the ZPE, only the x and y translational energies are significant among the values of the vibrational energies in Table 4.1. We determine the ZPE for H_2 to be 27.3 meV. For D_2, this value is decreased to 19.3 meV. Therefore, the rot-vibro energies of H_2 and D_2 are 175 and 195 meV, respectively. This translates to energy difference of 20 meV and $\frac{E_{D_2}}{E_{H_2}} = 1.11$.

4.2.5 Summary and Conclusions

In summary, we presented with the aid of DFT-based calculations the rotation and nuclear spin isomer separation of H_2 on Pd(210) surface for different atomic H coverages ($\Theta = 1/3, 2/3, 1$ ML). We demonstrated that the H_2 molecular adsorption happens on the top of step-edge Pd atom in *parallel* orientation to the plane formed by $[1\bar{2}0]$ and [001] for $\Theta = 1/3$ and 2/3 ML. Using the results of our orientation-dependent potential energy calculations, we computed the rotational states and energies of H_2 on Pd(210) for different atomic converages. Our results showed that the rotational energies of hindered $J = 0$, $J = 1, m = 0$ and $J = 1, m = \pm 1$ states slightly decreased as we increased the coverage of pre-adsorbed atomic H from $\Theta = 1/3$ to 2/3 ML Furthermore, we found that the $p{-}H_2$ has higher adsorption energy compared to $p{-}H_2$ in both Θ. Finally, we showed that the desorption energy of $o-$ is larger than $p{-}H_2$ by around 7 meV for both Θ. We have also investigated the effects of anharmonicity of the highly anisotropic adsorption potential to the rotational and vibrational states of H_2 adsorbing on Pd(210). Using total energy calculations, we constructed the 2D PES of the adsorbing H_2 for different CM-surface distance Z and molecular oriention θ. Under the influence of this 2D PES, we calculate the quantum motion of H_2 on Pd(210). Our results show that the ground state energy of H_2 is -203.5 meV and first excited state energy level is -197.6 meV. Upon close examination of the corresponding wavefunctions, we identified that

the ground and first excited rotational and vibrational states are para-H_2 and ortho-H_2, respectively. The desorption energy difference is 10 meV, favoring desorption of para isomers. From the analysis of the nodes of the wavefunctions, we have identified the H_2 vibrational states in the adsorption potential well. We have also investigated the isotope effects. We found that the rotational-vibrational ground state energy level -214.5 meV belongs to ortho-D_2. This energy is 12.2 meV larger than H_2 due to the mass difference between the two isotopes of hydrogen. We further find this energy difference to be significantly enhanced by $\simeq 10$ meV when we considered the zero point energies of the molecules in the adsorption potential well.

4.3 H_2 nuclear spin isomer conversion on Pd(210)

4.3.1 Model

The H_2 nuclear spin isomer conversion on Pd(210) can be described by the general formulations discussed in preceeding section for a system composed of a diatomic molecule adsorbing on a metal surface. We consider an H_2 approaching the top of the step-edge Pd atom of Pd(210) depicted in Figure 4.4. In this model, the Hamiltonian of the approaching H_2 is given by

$$H_M = \sum_\sigma \varepsilon_a \left(a^\dagger_{1\sigma} a_{1\sigma} + a^\dagger_{2\sigma} a_{2\sigma}\right) + t \sum_\sigma \left(a^\dagger_{1\sigma} a_{2\sigma} + h.c.\right) + U_a \left(n_{1\uparrow} n_{1\downarrow} + n_{2\uparrow} n_{2\downarrow}\right) + J_a \left(n_{1\uparrow} + n_{1\downarrow}\right)\left(n_{2\uparrow} + n_{2\downarrow}\right). \quad (4.60)$$

Further, we describe electronic state of the metal surface with

$$H_S = \sum_{k\sigma} \epsilon_k c^\dagger_{k\sigma} c_{k\sigma}, \quad (4.61)$$

where ϵ_k describes the kinetic energy of electrons in the conduction band of the Pd(210). The interactions between the electrons of H_2 and Pd(210) are accounted by

$$H_{M-S} = \sum_{k\sigma} \left[V_{ak}(Z,\theta) c^\dagger_{a\sigma} c_{k\sigma} + V_{bk}(Z,\theta) c^\dagger_{b\sigma} c_{k\sigma} + h.c.\right], \quad (4.62)$$

where $V_{ak}(Z,\theta)$ and $V_{bk}(Z,\theta)$ correspond to the hybridization between the metal surface electrons and the anti-bonding and bonding orbitals electrons of H_2, respectively. The H_2 nuclear spin flipping is described by the Fermi contact interaction

$$H_F = \sum_{k\sigma} \left[\Delta_{ak}(Z,\theta) c^\dagger_{a\sigma} c_{k'-\sigma} + \Delta_{bk}(Z,\theta) c^\dagger_{b\sigma} c_{k'-\sigma} + h.c. \right]. \tag{4.63}$$

We assume the nuclear spin isomer conversion proceeds in a two-step process: 1) an electron from Pd(210) transfers to the anti-bonding state of H_2, creating a hole in the metal surface band and an ionic molecule, and 2) the electron occupying the anti-bonding orbital of H_2 transfers back to the metal surface at a state $|k'\rangle$ above the Fermi level, while simultaneously spin flips, resulting to a triplet metal surface and neutral H_2.

4.3.2 Transition probability

The conversion probability from the initially *o*-H_2 to the final state *p*-H_2 may be calculated by perturbation theory up to second order as

$$P_{f\leftarrow i} = \frac{2\pi}{\hbar} \sum_{k,k'} \left| \frac{\langle \Psi_f | H_F | \Psi_p \rangle \langle \Psi_p | H_{M-S} | \Psi_i \rangle}{E_i - E_p} \right|^2 \delta\left(\epsilon_{k'} - \epsilon_k - \varepsilon_{op}\right). \tag{4.64}$$

Using (4.41) and (4.42) we re-express (4.64) at absolute zero temperature as

$$P_{f\leftarrow i} = \frac{8\pi}{\hbar \Phi^2} \sum_{k,k'} |\tilde{\Delta}_{ak'}(Z,\theta)|^2 |V_{ak}(Z,\theta)|^2 \delta\left(\epsilon_{k'} - \epsilon_k - \varepsilon_{op}\right), \tag{4.65}$$

where $\Phi = \varepsilon_a + t + \frac{U_a+J}{2} - \phi_{wf}$ and ϕ_{wf} is Pd(210) work function. $|\tilde{\Delta}_{ak'}(Z,\theta)|^2$ and $|V_{ak}(Z,\theta)|^2$ are given by

$$|\tilde{\Delta}_{ak'}(Z,\theta)|^2 = \frac{1}{2}\lambda^2 \left[\tilde{\Delta}^2_- \cos^2\left(k'\frac{r}{2}\sin\theta\right) + \tilde{\Delta}^2_+ \sin^2\left(k'\frac{r}{2}\sin\theta\right) \right], \tag{4.66}$$

$$|V_{ak}(Z,\theta)|^2 = \frac{1}{2} V_0^2 u(Z)^2 \left[f^2_-(\theta) \cos^2\left(k\frac{r}{2}\sin\theta\right) + f^2_+(\theta) \sin^2\left(k\frac{r}{2}\sin\theta\right) \right]. \tag{4.67}$$

We transform the summation over k into an integration so that for any function $G(\epsilon_k)$

$$\sum_k \cos^2\left(k\frac{r}{2}\sin\theta\right) G(\epsilon_k) \simeq \int_0^\infty d\epsilon \rho(\epsilon) G(\epsilon) \left[1 + \frac{\sin\left(2\sqrt{\frac{2m(\epsilon+D)}{\hbar^2}} r \sin\theta\right)}{2\sqrt{\frac{2m(\epsilon+D)}{\hbar^2}} r \sin\theta} \right] \tag{4.68}$$

and

$$\sum_k \sin^2\left(k\frac{r}{2}\sin\theta\right) G(\epsilon_k) \simeq \int_0^\infty d\epsilon\rho(\epsilon)G(\epsilon)\left[1-\frac{\sin\left(2\sqrt{\frac{2m(\epsilon+D)}{\hbar^2}}r\sin\theta\right)}{2\sqrt{\frac{2m(\epsilon+D)}{\hbar^2}}r\sin\theta}\right]. \quad (4.69)$$

$\rho(\epsilon)$ is the local density of states of step-edge Pd atom and D is the width of the filled conduction bands. Substituting (4.66) and (4.67) into (4.65), and using the transformations (4.68) and (4.69), we express the $o-p$ transition probability as

$$P_{f\leftarrow i} = \frac{2\pi}{\hbar}\frac{\lambda^2 V_0^2 u(Z)^2}{\Phi^2}\int_{E_F=0}^{D} d\epsilon\rho(\epsilon)\rho(\epsilon+\varepsilon_{op})\Gamma_C(\epsilon)\Gamma_F(\epsilon+\varepsilon_{op}), \quad (4.70)$$

where

$$\Gamma_C(\epsilon) = f_-^2(\theta)\left[1+\frac{\sin\left(2\sqrt{\frac{2m(\epsilon+D)}{\hbar^2}}r\sin\theta\right)}{2\sqrt{\frac{2m(\epsilon+D)}{\hbar^2}}r\sin\theta}\right]+f_+^2(\theta)\left[1-\frac{\sin\left(2\sqrt{\frac{2m(\epsilon+D)}{\hbar^2}}r\sin\theta\right)}{2\sqrt{\frac{2m(\epsilon+D)}{\hbar^2}}r\sin\theta}\right] \quad (4.71)$$

$$\Gamma_F(\epsilon+\varepsilon_{op}) = \tilde{\Delta}_-^2\left[1+\frac{\sin\left(2\sqrt{\frac{2m(\epsilon+\varepsilon_{op}+D)}{\hbar^2}}r\sin\theta\right)}{2\sqrt{\frac{2m(\epsilon+\varepsilon_{op}+D)}{\hbar^2}}r\sin\theta}\right] + \tilde{\Delta}_+^2\left[1-\frac{\sin\left(2\sqrt{\frac{2m(\epsilon+\varepsilon_{op}+D)}{\hbar^2}}r\sin\theta\right)}{2\sqrt{\frac{2m(\epsilon+\varepsilon_{op}+D)}{\hbar^2}}r\sin\theta}\right] \quad (4.72)$$

To numerically evaluate (4.70), we assume that the hybridization energy V_0 can be obtained from the resonance level width $\Delta(\epsilon) = \pi\sum_k |V_{ik}|^2\delta(\epsilon-\epsilon_k)$ of a single hydrogen atom adsorbing on Pd(210). To simplify our calculations, we take the resonance level width as

$$\Delta(\epsilon) = \pi\frac{|V_0|^2}{D}\Theta(D/2-\epsilon), \quad (4.73)$$

where Θ is a step function. We estimate Δ from the difference in the widths of the DOS projected on the s orbital of a hydrogen atom adsorbed on top of step-edge Pd atom and isolted H obtained by fitting to our DFT calculations. Similarly, explicit expressions for $\tilde{\Delta}_\pm^2$ in $\Gamma_F(\epsilon)$ are derived using Slater-type orbitals (STO) for the hydrogen orbitals,

and surface state wave function are represented by plane waves. We show in Figure 4.12 the calculated $o-p$ transition probability as a function of H_2-Pd(210) distance Z for different molecular orientations θ. In this figure, we can clearly see the strong dependence of the $o-p$ transition probability to the polar orientation θ. $\theta = 0$ results in higher conversion probability than $\theta = 90°$. From $P_{f\leftarrow i}$, we can obtain the transition rate as $\tau = P^{-1}_{f\leftarrow i}$. This means that perpendicularly oriented H_2 on top of step-edge Pd atom has the fastest conversion rate than that one oriented parallel. This is due to our conversion mechanism which involves the occupation of H_2 anti-bonding states described by the hybridization V_{ak}. This hybridization potential is maximum when $\theta = 0°$. We note that the mechanism we considered in this study is consistent with the findings of a DFT study[116] of H_2/Pd(210) in which the molecule's antibonding states are occupied by surface electrons upon adsorption. From the PEC in Figure 4.5, H_2 is bound on top of the step-edge Pd at $z = 1.9$ Å and $\theta = \pi/2$. At this configuration, the corresponding o-p conversion time is $\tau = 1.7$ s. This value increases to $\tau = 7.4$ s for $z = 2.5$ Å and approaches to 10^3 order at large z. Our calculated τ at the MC state agrees well with our experimental data. When $\theta = 0$, the minimum of the PEC is shifted (see Fig. (S2)) to $z \approx 2.5$ Å and H_2 is in a molecular physisorption state. We computed the value of o-p conversion rate at this configuration as $\tau = 3.1$ s, which is faster compared to the value at the same H_2-Pd distance with $\theta = \pi/2$ orientation. These conversion times are quite fast compared to the ones obtained on flat metal surfaces[55]. τ also becomes longer when Z increases as dictated by γ. On H_2/Pd(210), REMPI-TPD study[121] have shown that the desorption intensities of the *o*- and *p*-H_2 follow the Arrhenius relations continously up to 75 K. Above this temperature, a significant deviation from the relations have been observed. This deviation has been attributed to the $o-p$ transition of H_2 adsorbed on top of step-edge Pd atom. From the analysis of this deviation, the $o-p$ conversion time has been estimated to be ≈ 0.5 s. This value is in good agreement with our results on the basis of perturbation theory.

4.3.3 Summary and Conclusions

We have investigated the $o-p$ conversion of H_2 adsorbed on stepped Pd surface by means of model Hamiltonian on the basis of second order perturbation theory. Our results show that the transition probability exponentially decays away from the adsorption site. We have also shown that the perpendicular oriented H_2 has higher conversion probability

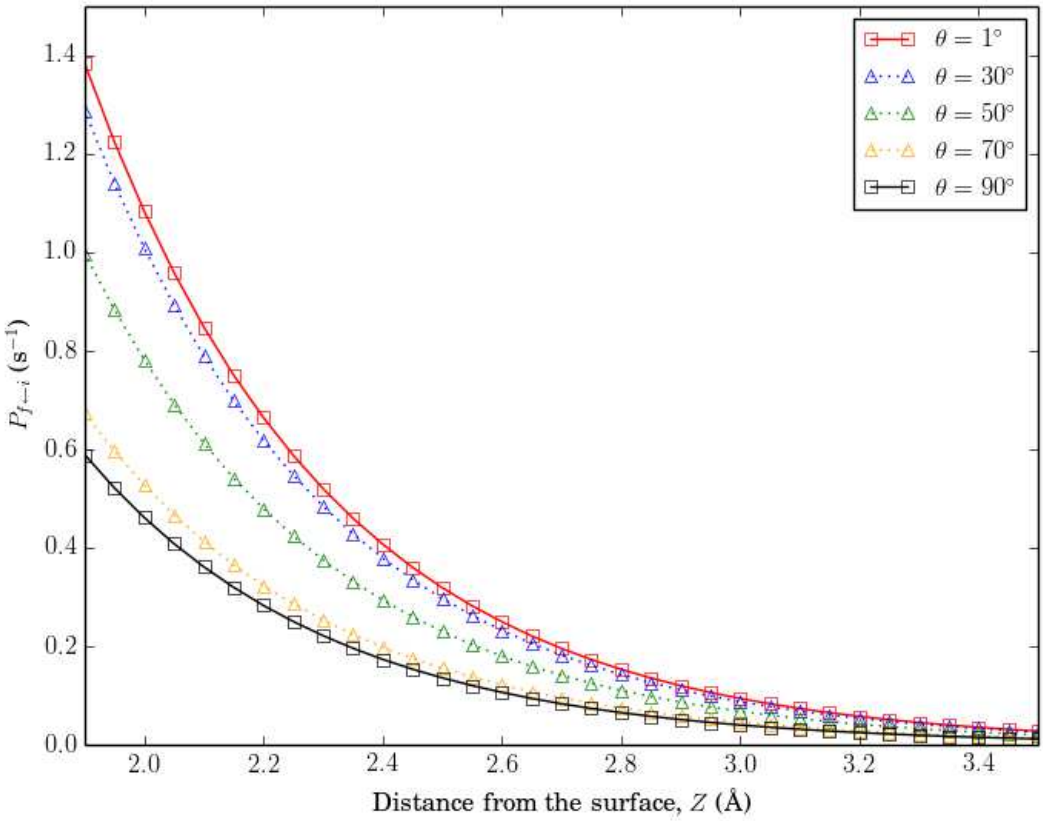

FIGURE 4.12: $o-p$ conversion probability as a function of H_2 CM- step-edge Pd atom distance Z for different polar orientations θ. The origin of the x-axis is set at the equilibrium bonding distance $Z_{eq} = 1.9$ Å.

compared to the one in parallel orientation. The calculated conversion times are 1.8 s and 10 s for perpendicular and parallel oriented molecule which are in good agreement with the observed experimental value of ≈ 0.5 s. Based from our model calculations, we can conclude that the conversion probability is highly dependent on the width of the occupied conduction electron states of the metal substrate and the H_2-Pd(210) bonding distance.

Chapter 5

Summary, Conclusions and Outlook

We have presented using two case studies how computational materials design of solid surfaces with symmetry consideration can be used to influence the electronic and nuclear spin states. Interstitial magnetic impurities in a layered semiconducting oxide surface broke the local symmetry around the magnetic ions by changing the local crystal field through $p-d$ orbital hybridization. This effectively splits the orbitals of the impurity and host crystal atoms inducing spin polarization on the system. By exchanging of electrons through neighboring atoms, we have shown in Chapter 4 that the spin states of electrons can achieve magnetic ordering that persists above room temperature. We have concluded that the magnetic double exchange mechanism stabilises ferromagnetic ordering of electronic spins in the solid surface. The results of our case study can be extended to materials that possess a geometric structure similar to the one that we considered. To test the possibility of practical implementation of our material as a spintronics device, further calculations are needed to evaluate the effects of charge carrier concentrations on the magnetic ordering of electronic spins. Our preliminary results have shown that increased hole concentrations increases the magnetic moment of the surface by shifting the DOS above the Fermi level. This in effect may destabilise the ferromagnetic ordering of electronic spins. The increase in electron concentrations on the other hand do not induce further magnetic moments in the surface by shifting the DOS below the Fermi level. This have shown to stabilise ferromagnetism although further collinear DFT study is needed to verify this hypothesis. Similarly, we have shown in

Chapter 5 that contrary to flat surfaces, H_2 can have a chemisorbed molecular adsorbed state. The steps on metal surfaces bring H_2 to a molecular chemisorbed (MC) state and break the rotational symmetry of the molecule. Using total energy calculations, we found a highly anisotropic potential energy surface (PES) of the adsorbing H_2 on Pd(210). From our calculations of H_2 quantum motion under the influence of this PES, we found that the ground and the first excited rotational and vibrational eigenvalues correspond to *para*- and *ortho*-H_2, respectively. We also found that the desorption energies of the two lowest energy nuclear spin isomers is around 10 meV, favoring *para*-H_2 desorption. Although our results are consistent with experimental findings, our picture of desorption dynamics can be further improved by considering other molecular degrees of freedom neglected in this study. On the basis of second order perturbation theory, we have found that the *ortho-para* nuclear spin isomer transition probability is highest in perpendicularly oriented H_2. Our calculated conversion times are in good agreement with experiments. Based from our model calculations, the transition probability is highly dependent on the width of the occupied electron states of the surface. Our results have shown that narrower local density of states of the metal substrate leads to faster *ortho-para* nuclear spin isomer transition. In order to verify this direct correlation between the surface occupied electronic state and the isomer conversion, calculations involving other stepped transition metal surfaces are needed.

Appendix A

Magnetism in Density Functional Theory (DFT)

In this Appendix, we discuss how spin-polarised calculations are implemented in DFT.

A.1 Collinear DFT

The concept of DFT can be extended to the spin-polarised systems by replacing the Kohn Sham density a 2×2 Hermitian matrix. Consider a particle with spin α and field operator $\psi_\alpha(\mathbf{r})$ a component of the spin density matrix can be expressed as

$$\rho_{\alpha\beta}(\mathbf{r}) = \left\langle \Psi \middle| \psi_\alpha^+(\mathbf{r})\ \psi_\beta^-(\mathbf{r}) \middle| \Psi \right\rangle . \tag{A.1}$$

It therefore required to also replace scalar potential $V(\mathbf{r})$ in the Kohn-Sham potential with $\bar{V}(\mathbf{r})$ which corresponds to the spin density matrix. One can then rewrite the Kohn-Sham equation as

$$\left[\left(-\frac{1}{2}\nabla^2 + \sum_\alpha \int \frac{\rho_{\alpha\alpha}(\mathbf{r}')}{\left|\mathbf{r}-\mathbf{r}'\right|} d\mathbf{r}' \right) \bar{I} + \bar{V}(\mathbf{r}) + \frac{\delta E_{xc}}{\delta \bar{\rho}(\mathbf{r})} \right] \begin{pmatrix} \phi_i^{(+)}(\mathbf{r}) \\ \phi_i^-(\mathbf{r}) \end{pmatrix} = \epsilon_i \begin{pmatrix} \phi_i^{(+)}(\mathbf{r}) \\ \phi_i^-(\mathbf{r}) \end{pmatrix} \tag{A.2}$$

where $\bar{I}$ is a 2×2 unitary matrix and by virtue of Eq.(A.1), the exchange-correlation potential now also becomes a 2×2 matrix. In terms of the Kohn-Sham orbitals, the spin density takes the form

$$\rho_{\alpha\beta}(\mathbf{r}) = \sum_{i=1}^{N} \phi_i^{\star\alpha}(\mathbf{r})\phi_i^{\beta}(\mathbf{r}) \,. \tag{A.3}$$

where $\alpha(\beta) = +(-)$ is the electron spin up(down). Pauli matrices allow the decomposition of the density matrix into scalar and vectorial parts which correspond to the charge and magnetisation density

$$\begin{aligned} \bar{\rho}(\mathbf{r}) &= \frac{1}{2}\left(\rho(\mathbf{r})\bar{I} + \bar{\sigma}\cdot\ \mathbf{m}(\mathbf{r})\right) \\ &= \frac{1}{2}\begin{pmatrix} \rho(\mathbf{r}) + m_z(\mathbf{r}) & m_x(\mathbf{r}) - im_y(\mathbf{r}) \\ m_x(\mathbf{r}) + im_y(\mathbf{r}) & \rho(\mathbf{r}) - m_z(\mathbf{r}) \end{pmatrix} . \end{aligned} \tag{A.4}$$

It is also possible to write the potential matrices in terms of magnetic field $\mathbf{B}$

$$\begin{aligned} \bar{V}(\mathbf{r}) &= V(\mathbf{r})\bar{I} + \ \mu_B\bar{\sigma}\cdot\mathbf{B}(\mathbf{r}) \\ \bar{V}_{xc}(\mathbf{r}) &= V_{xc}(\mathbf{r})\bar{I} + \ \mu_B\bar{\sigma}\cdot\mathbf{B}_{xc}(\mathbf{r}) \,. \end{aligned}$$

where μ_B is the Bohr magneton. Within this formalism, one can solve Eq.(A.2) by expanding the Kohn-Sham orbitals $\phi_i(\mathbf{r})$ in a linear combination of basis functions $\xi_j(\mathbf{r})$

$$\phi_i(\mathbf{r}) = \sum_i c_{ij}\xi_j(\mathbf{r}) \,, \tag{A.5}$$

which transforms Eq.(A.2) into an eigenvalue problem that solves the linear combination coefficients c_{ji}. Furthermore, if the potential matrices in Eq.(A.5) are diagonal, meaning the magnetic and exchange fields are pointing at z direction, Eq.(A.2) decouples into two equations that can be solved independently. This case is called the collinear magnetism. The spin density is expressed in spin-polarised DFT as

$$\mathbf{m}(\mathbf{r}) = -\mu_B \sum_{\alpha,\beta} \psi_\alpha^+(\mathbf{r})\ \sigma_{\alpha,\beta}\psi_\beta(\mathbf{r})\ , \tag{A.6}$$

and the integral of spin moment M is given by

$$M_{spin} = \int \mathbf{m}(\mathbf{r})d\mathbf{r} = \int \left(n^+(\mathbf{r}) - n^-(\mathbf{r})\right) d\mathbf{r}\ . \tag{A.7}$$

We obtain the magnetic state energy by fixing the value of the spin of the particular ions/atoms of interest and solving the Kohn-Sham equation. The total energy obtained is then subtracted to the result of the non- spin-polarised calculation. We determine the magnetic order by solving the KS equation for both ferromagnetic (FM) and antiferromagnetic (AFM) alignments of the electron spins in the atoms in the so-called supercell approach[122, 123]. The difference in FM and AFM energies is

$$\Delta E = E_{AFM} - E_{FM}. \tag{A.8}$$

Positive value of ΔE means FM order among the electron spins is more dominant than AFM, while negative value means the opposite.

A.2 Mapping DFT calculations to Heisenberg Model

Let us consider a diatomic molecule with two electrons corresponding to four spin states: a *singlet* $\frac{1}{\sqrt{2}}(|\uparrow\downarrow\rangle - |\downarrow\uparrow\rangle)$, and three degenerate *triplet* $|\uparrow\uparrow\rangle$, $|\downarrow\downarrow\rangle$, $\frac{1}{\sqrt{2}}(|\uparrow\downarrow\rangle - |\downarrow\uparrow\rangle)$ states. The total spin $\mathbf{S} = \mathbf{s}_1 + \mathbf{s}_2$ is an operator that commutes with the Hamiltonian of the system. Therefore, the eigenstates of the Hamiltonian of the system is also the eigenstates of $\mathbf{S}$. The Hamiltonian therefore has two eigenenergies E_s and E_t corresponding to $\mathbf{S} = 0$, singlet and $\mathbf{S} = 1$, triplet states, respectively. The square of the operator ca be written as

$$\mathbf{S}^2 = s_1^2 + s_2^2 + 2\mathbf{s}_1 \cdot \mathbf{s}_2 = \frac{3}{2} + 2\mathbf{s}_1 \cdot \mathbf{s}_2, \tag{A.9}$$

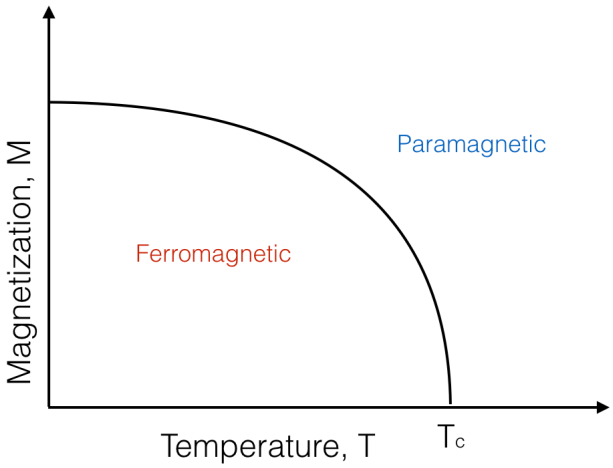

FIGURE A.1: Schematic diagram of magnetization as a function of temperature

where $\mathbf{s}_1 \cdot \mathbf{s}_2$ is equal to $\frac{1}{4}$ for $S = 1$ and $-\frac{3}{4}$ for $S = 0$. With this we can map the original Hamiltonian to the so called Heisenberg spin Hamiltonian as

$$H = \frac{1}{4}(E_s + 3E_t) - (E_s - E_t)\,\mathbf{s}_1 \cdot \mathbf{s}_2. \tag{A.10}$$

We may drop the first (constant) term in (A.11) and rewrite the Hamiltonian as

$$H = -2J\mathbf{s}_1 \cdot \mathbf{s}_2, \tag{A.11}$$

where $J = (E_s - E_t)/2$. This result may be generalised for arbitrary number of atoms and spins as

$$H = -\sum_{i,j} J_{i,j}\mathbf{S}_i \cdot \mathbf{S}_j, \tag{A.12}$$

where the sum i and j run over all lattice sites. The exact solution for the ground state of the Heisenberg model (A.12) is still unknown up to this moment and we are only able to decribe its physical properties by introducing the classical approximation. This entails replacing the spin operator $\mathbf{S}$ with a real, 3-dimensional vector whose magnitude is $|\mathbf{S}| = S$. Experiments often measure the material's magnetization curves over a wide range of temperatures as schematically drawn in Figure A.1. For ferromagnetic substances, the magnetization curve vanishes at some temperature value T_c, or the so called Curie temperature. At $0 \leq T \leq T_c$, the spin system form a ferromagnetic order, that is the spins of the atoms are aligned parallel to each other. At $T \geq T_c$, the spin

alignment becomes random, destroying the magnetic order and the system transitions from ferromagnetic to paramagmnetic state. Therefore, T_c is a direct measurement of the strength of ferromagnetism in a material. In this study, we will determine T_c from first principles calculations based on DFT. In the mean field approximation (MFA)[124], T_c can be calculated as

$$k_B T_c^{MFA} = \frac{2}{3} \sum_{i \neq 0} J_{0i}, \tag{A.13}$$

where J_{0i} is the magnetic exchange interaction between the 0th and the ith spins. From the previous discussions of the molecular Heisenberg model, J_{0i} can be viewed as the difference between the singlet and triplet eigenenergies. Similarly, we can obtain J_{0i} from collinear DFT calculations as the energy difference between the AFM and FM spin configurations, or $J = E_{AFM} - E_{FM}$.

Appendix B

DFT calculations details

B.1 DFT calculation details of interstitial impurities in PbO surface

All calculated physical properties presented here are obtained using ab-initio calculations, implemented on Vienna Ab-initio Simulation Package (VASP)[125, 126] based on the density functional theory (DFT)[127, 128]. Electron and core interactions are described using projector augmented plane wave (PAW) formalism with an energy cutoff of 500 eV. Charge densities in VASP are expressed using plane wave basis sets[129]. Spin polarised calculations are performed to derive the electronic and magnetic properties of the system in question within the generalised gradient approximation (GGA) using Perdew, Burke and Ernzerhoff (PBE) exchange correlation potential[130]. Brillouin-zone integration are performed using $5 \times 5 \times 5$ and $7 \times 7 \times 1$ Monhorst-Pack k-points meshes with Gaussian smearing for bulk and surface respectively[131]. Bulk structure is optimised by scanning possible values of lattice parameters close to experimental obtained $a = b = 3.947$ Å and $c = 4.988$ Å that give lowest energy configuration. From this structure, a surface is modelled using a 3-layer α-PbO (001) slab within a 2x2 supercell with 20 Å vaccuum area. The surface structure is obtained by allowing the upper two layers of the slab to relax whilst fixing the bottom layer. Since litharge is a layered structure, and each layer is composed of two sublayers (O and Pb sublayers), a possibility of having two types of surfaces based on termination arises; oxygen and lead terminated surfaces. However, energetic calculations incoporating van der Waals

Lattice Vectors	GGA	vdW-DFT	Experiment[134]
a	4.090Å	4.090Å	3.96Å
c	5.502Å	5.216Å	5.01Å
c/a	1.345	1.275	1.27

TABLE B.1: Calculated bulk lattice vectors with and without van der Waals correction compared with experimentally obtained results.

(vdW) corrections[132, 133] confirm the energetically unfavourability of the oxygen terminated surface and that upon structural relaxations, the system evolves in favour of lead termination. Hence, in all calculations presented herein, a Pb-terminated surface is utilised.

B.1.1 Bulk PbO

The calculated bulk lattice parameters with and without van der Waals corrections are shown in Table B.1. Both results for lattice vector a are in good agreement with experimental values of 3.96 Å[134] and 3.95Å[135] and in theoretical works of Canepa *et.al.*,[136] and Raulot *et.al.*,[137]. It also shows that GGA alone fails to replicate the experimental lattice vector along the c-axis since in its scheme, dispersive interactions are not considered and only local orbitals are properly treated. The addition of van der Waals effects provides a solution to this issue as exhibited in the computed lattice constant value in the c-axis of 5.216 Å which is in good agreement with experiment (5.01 Å). For litharge and other layered systems, this correction is crucial when constructing surfaces from bulk parameters as it could spell large amount of errors on energy and geometry calculations. This therefore suggests that the inclusion of vdW from the very beginning i.e. bulk structural optimisations, is required to arrive at the correct surface properties. Furthermore, the sensitivity of electronic and structural properties on the lattice parameters implies that one has to pay a great deal of attention to these details during computations. For instance, in calculations of defect formation energies, the authors in (cf. ref[138]) determined the lattice constants entirely by GGA which yielded a serious mismatch between the computed (5.51 Å) and experimentally obtained c vectors. In order to compensate for this problem, experimental value of the c lattice vector is used in their calculations. It is therefore stressed here that one can avoid these limitations by employing vdW corrections which can also allow to treat the system purely on theoretical grounds.

As discussed above, lattice parameters play important roles in the determination of many physical properties. Among these, a particular interest is in the system's electronic property not just because it gives someone insights on the nature of bonding and defect interactions, but also due to the fact that it serves as a window on the origin of magnetism induced by impurities in this material as will be shown in the following discussions. Litharge or α-PbO is a semiconductor with an experimentally obtained indirect band gap of 1.95 eV[139] measured at 300K. DFT calculated band gaps however can vary slightly from experiments depending on the chosen bulk lattice constants during relaxations, *i.e.* structure optimisations. If one chooses lattice constants from experiments as initial parameters during relaxation runs, a narrow gap value of 1.46 eV is obtained. This problem can be avoided if the GGA optimised lattice parameters are used as reported in [138] which obtained a gap of 1.8 eV, in good agreement with the experimental value. Furthermore, the GGA optimised lattice parameters with van der Waals corrections yields a relatively acceptable band gap value of 1.7 eV. A decrease in the c-axis lattice constant causes GGA to overestimate the interlayer orbital overlap of $6s^2$ lone pairs which weakly hold the layers together[69]. This overestimation leads to stronger interlayer forces and eventually to the shrinking of the gap as confirmed by the calculations of this study.

B.2 DFT calculations of H_2/Pd(210)

The temperature programmed desorption (TPD) spectra in Ref[115] point to three β and two γ peaks as atomic and molecular adsorptions, respectively. In order to simulate H_2 adsorption on Pd(210), we considered a clean surface illustrated in Figure B.1. We performed density functional theory[140, 141](DFT)-based calculations to explore the dissociative and molecular adsorptions of H_2 on Pd(210). In the calculations, we used projector augmented formalism (PAW)[142] with Perdew-Burke-Enzwerhoff (PBE) generalized gradient (GGA) exchange correlation functional[143, 144], and a cutoff energy of 500 eV. We adopted Monkhorst and Pack method[145] for Brillouin zone integrations. We modelled the clean Pd(210) (Figure B.1) as periodic slabs containing 9 layers of Pd atoms separated by 15 Å of vacuum. For the dissociative adsorption, we considered the dissociation sites in Figure B.2.

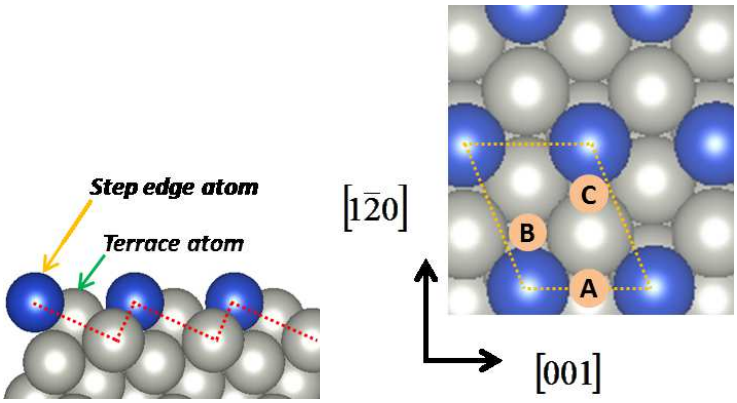

(A) (B)

FIGURE B.1: (a) Side view of the slab model of Pd(210) surface. The blue spheres correspond to the step edge atoms. The dashed red line traces the steps of the surface. (b) Top view of the Pd(210) surface model where the unit cell used is represented by the yellow-dotted parallelogram over the step edge atoms. The labels *A*, *B* and *C* are the adsorption sites of pre-adsorbed atomic H.

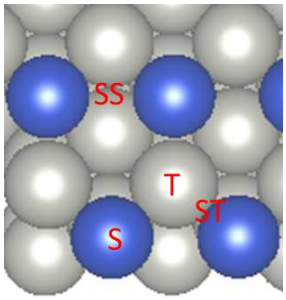

FIGURE B.2: Dissociation sites on clean Pd(210). S: step-edge Pd atom, T: terrace site Pd atom, ST: bridge between T and S sites and SS: bridge between two S sites. The dissociated atoms for S site adsorb on the SS site, while on T site, adsorb on the four-fold coordinated hollow site. The dissociated atoms on ST site go to the hollow and SS sites, while on SS, one hydrogen atom goes to top of the third layer Pd atom, while the other one goes to S.

B.2.1 H_2 dissociative adsorption on a clean Pd(210)

Figure B.3 shows the potential energy surfaces (PES) contour plots of the dissociative adsorption of H_2 on a clean Pd(210). Away from the surface, the S site is the most attractive of H_2 adsorption. However, as H_2 approaches near the top of the step-edge Pd atom, it goes to the ST site and dissociates with a ver minimal barrier. On the contrary, other sites exhibit no energy barrier towards H_2 dissociation. It therefore appears that the complete picture of H_2 adsorption on clean Pd(210) is as follows: initially, an H_2 molecule is attracted towards the S site due to its being the most reactive compared to all the other sites considered, then as the molecule approaches near the surface, it is attracted to the ST site where molecular dissociation happens. We performed

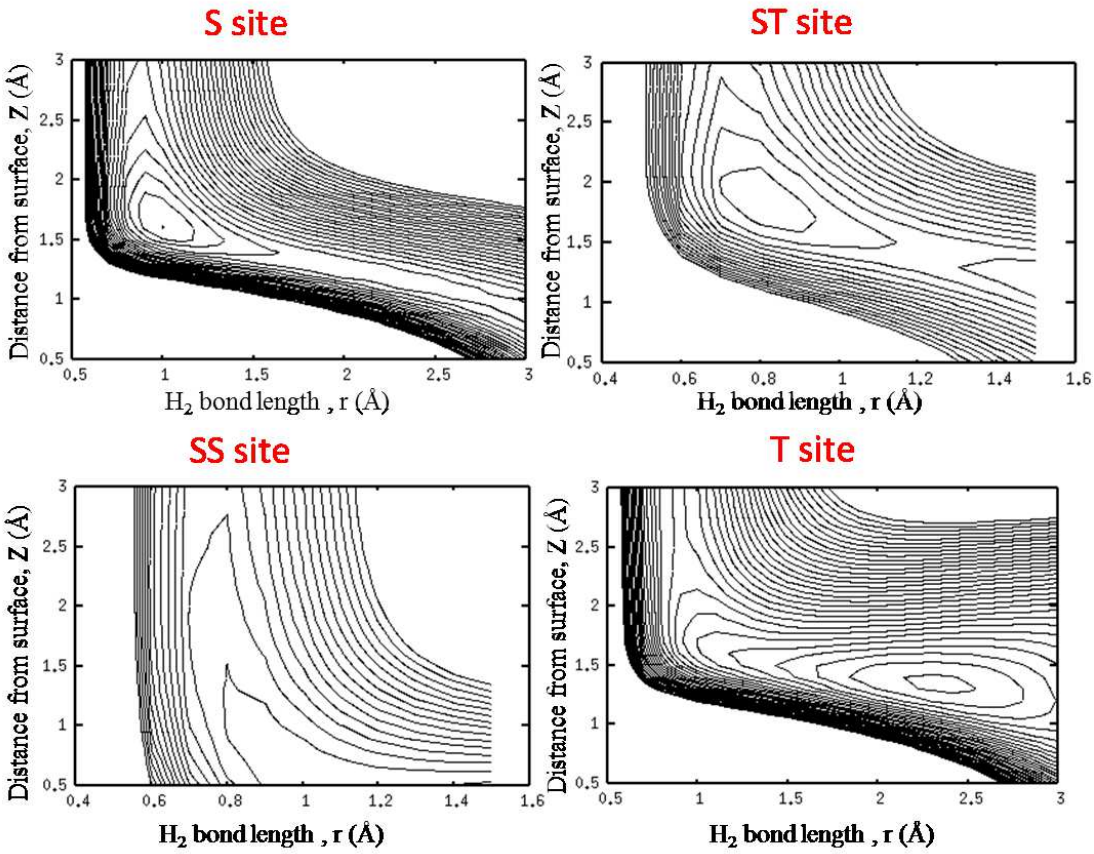

FIGURE B.3: Contour plot of dissociative adsorption potential energy surfaces (PES) of H_2 on S, T, ST, and SS sites of Pd(210). The contour spacing is 100 meV.

Coverage (ML)	Site	State	Binding Energy (This study)	Binding Energy (Ref[115])
$\Theta = 1/3$	A	β_3	580	410
$\Theta = 1/3$	C	β_3	560	410
$\Theta = 1/3$	B	β_3	490	410
$\Theta = 2/3$	A, B	β_2	440	330
$\Theta = 3/3$	A, B, C	β_1	330	230

TABLE B.2: Binding energies of different atomic adsorption sites and their TPD peak assignments.

relaxed calculations of the Pd(210) with adsorbed hydrogen atoms and found the most energetically favorable atomic adsorption site for an atomic coverage $\Theta = 1/3$ ML is on the A site in Figure B.1b. with a binding energy of 580 meV. This is followed by the three fold coordinated C site and the four-fold hollow B site. For $\Theta = 2/3$ ML, the most stable adsorption configuration is when both the A and B sites are occupied. For the full coverage $\Theta = 1$ ML, all atomic adsorption sites are occupied. This configuration has a binding energy of 330 meV. In Table B.2, we summarized the binding energies of

atomic adsorption sites and their corresponding TPD peak assignments. The β_3 peak of the TPD spectra can be assigned to a hydrogen atom occupying the SS site, while the β_2 peak can be assigned to two hydrogen atoms ($\Theta = 2/3$ ML) occupying the SS and the four-fold hollow sites. The β_1 peak can be assigned to a configuration where all of the atomic adsorption sites are occupied. This configuration corresponds to the $\Theta = 1$ ML coverage.

B.2.2 H_2 molecular adsorption on Pd(210)

We modelled the Pd(210) with different coverage (Θ) of pre-adsorbed H by adsorbing atomic hydrogen on different adsorption sites labelled A, B and C (see Figure B.1b). As discussed in the previous subsection, coverage of $\Theta = 1/3$ ML corresponds to the occupation of site A, sites A and B are populated for $\Theta = 2/3$ ML, and all sites are occupied for a full coverage of $\Theta = 1$ ML. Furthermore, we obtained the optimized $H_2/H_{nML}/Pd(210)$ (where $n = 1/3, 2/3, 1$) by relaxing all the degreess of freedom (DoF) of the molecule and that of the 3 top-most layers of Pd(210) including the pre-adsorbed H. When hydrogen atoms begin to occupy the different adsorption sites on Pd(210), succeeding adsorbing H_2 molecule dissociations are hindered as shown in Figure B.4. As can be seen in this figure, $\Theta = 1/3$ ML coverage of H atom is already sufficient to increase the barrier of H_2 dissociation on S and T sites of Pd(210). This is specially notable on the S site in which the H_2 adsorption profile is clearly molecular. On the T site, the energy barrier towards H_2 dissociation can be estimated to be around 800 meV. We can therefore conclude that molecular H_2 adsorption becomes possible only after one of the atomic adsorption sites have been occupied by hydrogen. This is because after hydrogen atom adsorption, the electronic profile of Pd(210) is drastically changed. We show this effect in Figure B.5. When atomic hydrogen adsorbs on the surface, it shifts the LDOS of step-edge Pd atom below the Fermi level. This shifting of the LDOS decreases the reactivity of the a particular adsorption site. This decrease in the reactivity of the adsorption sites on Pd(210) upon H atom adsorption gives way to molecular H_2 adsorption on the surface.

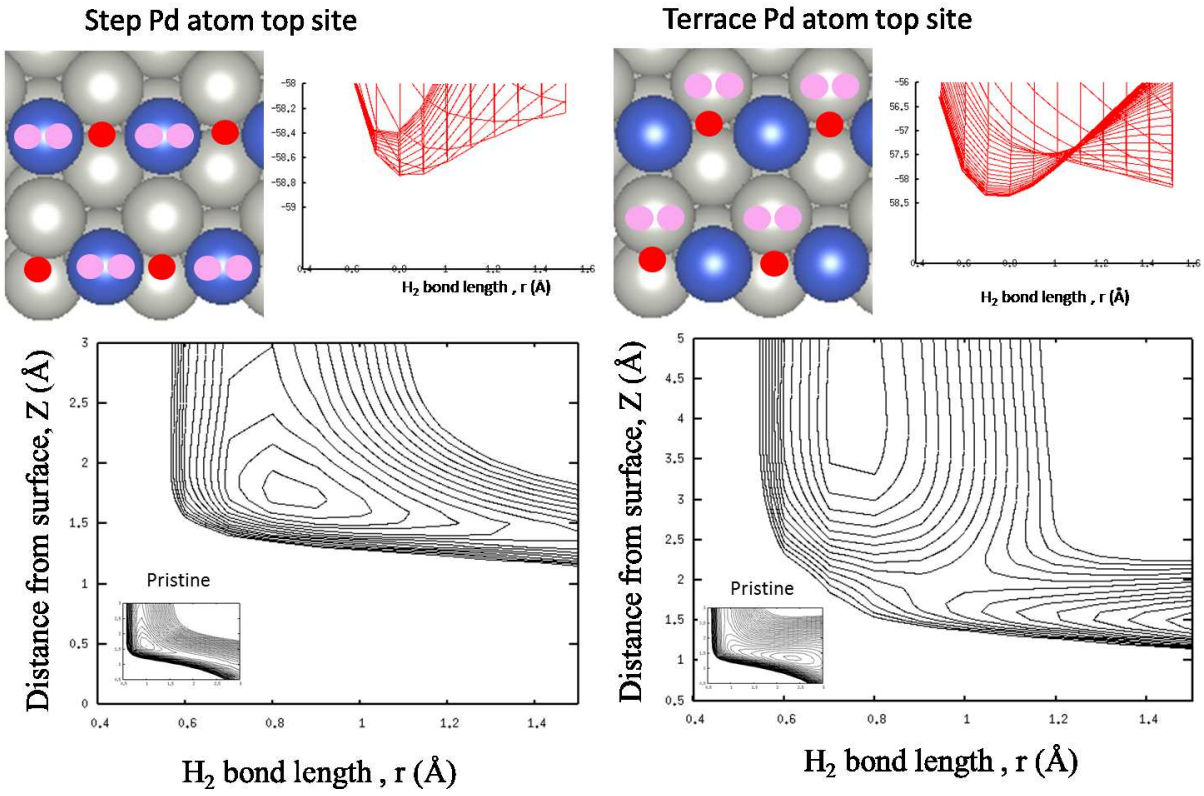

FIGURE B.4: Effects of adsorbed hydrogen atoms on the dissociation of H_2 molecules on Pd(210). The red dots correspond to adsorbed H atoms while the pink dots correspond to the atoms of H_2 molecules dissociating on top of step-edge Pd atom (S) and top of terrace atom (T) sites. The right panels are the plots of total energy vs the H_2 bond length r. The lower panels are the contour plots of the PES of H_2 dissociation on S (left panel) and T (right panel) sites, respectively.

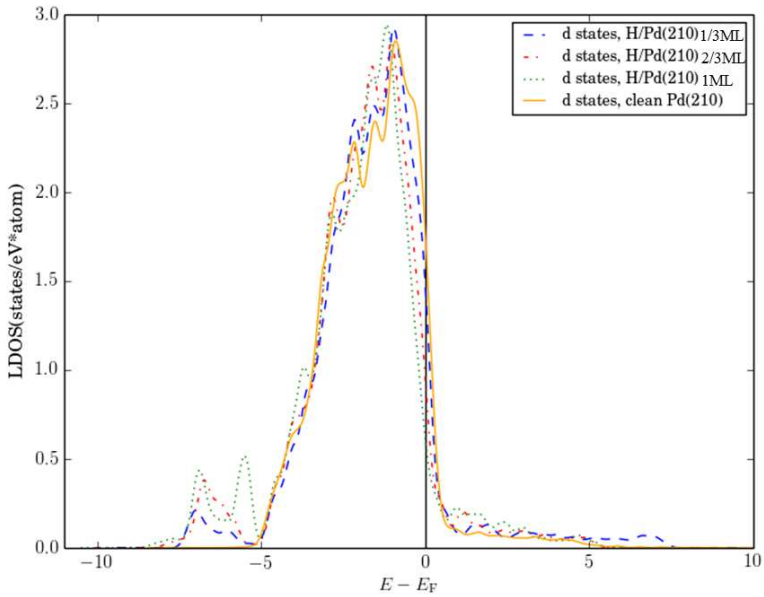

FIGURE B.5: Local density of states (LDOS) of the step-edge Pd atom of a clean and $H_{nML}/Pd(210)$ surfaces.

Awards

Best in Poster Presentation Award, 1st Japan Society of Applied Physics Kansai Meeting, 2017, Himeji, Japan

Best in Poster Presentation Award, 55th Japan Vacuum Society Meeting, 2014, Osaka, Japan

Research Fellowship for Young Scientists (DC), Japan Society for the Promotion of Science (JSPS)

Scholarship (MS), Ministry of Education, Culture, Sports, Science and Technology (MEXT), Japan

Science Education Institute Scholarship (MS), Department of Science and Technology (DOST), Philippines

Science Education Institute Scholarship (BS), Department of Science and Technology (DOST), Philippines

List of Publications

E. F. Arguelles, H. Kasai, K. Fukutani, A. Yajima, K. Nakayama, S. Yamashita, and W. A. Diño, H_2 Hindered Rotation and Nuclear Spin Isomer Separation on Pd(210), in preparation

E. F. Arguelles, H. Kasai, K. Fukutani, A. Yajima, K. Nakayama, S. Yamashita, and W. A. Diño, H_2 Bound Nuclear Spin States on a Stepped Metal Surface, in preparation

S. Ohno, D. Ivanov, E. F. Arguelles, W. A. Diño, and K. Fukutani Nuclear Dynamics of Quantum Rotor Under a Highly Anisotropic Potential, in preparation

D. Ivanov, S. Ohno, E. F. Arguelles, W. A. Diño, S. Ogura, and K. Fukutani Photodesorption of H_2: Probing the initial rotational wavefunction, in preparation

T. Ohkochi, H. Fujiwara, M. Kotsugi, H. Takahashi, R. Adam, A. Sekiyama, T. Nakamura, A. Tsukamoto, C. M. Schneider, H. Kuroda, E. F. Arguelles, M. Sakaue, H. Kasai, M. Tsunoda, S. Suga and T. Kinoshita, Giant Spin Waves Induced in Ferrimagnetic GdFeCo Film by Pulsed Light Excitation, Applied Physics Letters, under revision

S. Amino, E. F. Arguelles, W. A. Diño, M. Okada, and H. Kasai, C_2H_4 Adsorption on Cu(210) Revisited: Bonding Nature and Coverage Effects, Physical Chemistry and Chemical Physics, 18, 23621 (2016)

E. F. Arguelles, S. Amino, S. Aspera, H. Nakanishi and H. Kasai, Surface Magnetism in αPbO induced by Fe interstitials, Journal of the Physical Society of Japan, 84, 045002 (2015)

E. F. Arguelles, S. Amino, S. Aspera, H. Nakanishi and H. Kasai, Impurity Induced Magnetism in α PbO Surface, Journal of Physics: Condensed Matter, 27, 016002 (2015)

E. F. Arguelles, K. Shimizu, H. Nakanishi and H. Kasai, The Yoshimori-Kasai Model Phase Diagram and Naniwa Series of Quantum Dynamics, JPS Conf. Proc., 2, 010312 (2014)

List of Conference Presentations

1st Japan Society of Applied Physics Kansai Symposium (poster presentation)
Interstitial impurity-induced surface magnetism in a layered oxide
E. F. Arguelles, S. Amino, S. Aspera, H. Nakanishi, H. Kasai and W. A. Diño
Egret Himeji, Himeji, Japan, May, 2017

1st Japan Society of Applied Physics Kansai Symposium (poster presentation)
Quantum and nuclear bound states of H_2 on a stepped metal surface
E. F. Arguelles, H. Kasai, K. Fukutani, A. Yajima, K. Nakayama, S. Yamashita, and W. A. Diño
Egret Himeji, Himeji, Japan, May, 2017

64th Japan Society of Applied Physics Conference (oral presentation)
H_2 Adsorption on Pd(210) Surface: Nuclear Spin Isomer Separation and Conversion
E. F. Arguelles, H. Kasai, and W. A. Diño
Pacifico Yokohama, Yokohama, Japan, March, 2017

Symposium of Surface Science and Nanotechnology, 25th Anniversary of SSJ Kansai (poster presentation)
Hindered Rotation and Ortho-Para Conversion of H_2 on Pd(210) Surface
E. F. Arguelles, H. Kasai, and W. A. Diño
Kyoto International Community House, Kyoto, Japan, January, 2017

International Symposium of "Recent Trends in Analysis and Techniques of Functional Materials" (invited speaker, oral presentation)
H_2 Adsorption on Pd(210) Surface: Nuclear Spin Species Separation and Conversion
E. F. Arguelles, H. Kasai, and W. A. Diño
Osaka University, Osaka, Japan, January, 2017

International Symposium of "Recent Trends in Analysis and Techniques of Functional Materials" (invited speaker, oral presentation)
Surface as a playground for studying gas-surface dynamics: increasing the ortho-para conversion yield via molecular orientation, a case study
W. A. Diño, E. F. Arguelles, R. Kishida, K. Murayama, S. Shimizu, H. Kasai, H. Nakanishi, K. Fukutani, K. Nakayama, A. Yajima, and S. Yamashita
Osaka University, Osaka, Japan, January, 2017

International Workshop on Advanced Materials and Nanotechnology 2016 (IWAMN2016) (oral presentation)
Surface as a building block for designer materials and a means to control reactions: increasing ortho-para H_2 conversion yield via molecular orientation, a case study

W. A. Diño, E. F. Arguelles, R. Kishida, K. Murayama, S. Shimizu, H. Kasai, H. Nakanishi, K. Fukutani, K. Nakayama, A. Yajima, and S. Yamashita
Hanoi, Vietnam, September, 2016

Japan Physical Society Conference, Autumn Meeting (oral presentation)
Nuclear Spin States of H_2 Adsorbed on Pd(210) Surface
E. F. Arguelles, H. Kasai, and W. A. Diño
Kanazawa University, Kanazawa, Japan, September, 2016

8th Asian Computational Materials Design (CMD) Workshop (invited speaker, oral presentation)
Nuclear Spin Separationa and Conversion of H_2 on a Stepped Metal Surface
E. F. Arguelles, H. Kasai, and W. A. Diño
De La Salle University, Laguna, Metro Manila, Philippines, September, 2016

32nd European Conference on Surface Science (ECOSS 32), (oral presentation)
Revisiting H_2 Adsorption on Pd(210): Nuclear Spin States Separation and Conversion
E. F. Arguelles, H. Kasai, and W. A. Diño
Grenoble, France, August 28 - September 2, 2016

Stereodynamics 2016 (invited speaker, oral presentation)
Surface as a playground for studying gas-surface reaction dynamics: increasing the ortho-para H_2 conversion yield via molecular orientation, a case study
W. A. Diño, E. F. Arguelles, R. Kishida, K. Murayama, K. Shimizu, H. Kasai, H. Nakanishi, K. Fukutani, K. Nakayama, A. Yajima, and S. Yamashita
Taipei, Taiwan, September, 2016

71st Japan Physical Society Conference, Spring Meeting (oral presentation)
Hindered Rotation of H_2 Adsorbed on Pd(210) Surface
E. F. Arguelles, H. Kasai, and W. A. Diño
Tohoku Gakuin University, Sendai, Japan, March 2016

Quantum Engineering Design Workshop (oral presentation)
Fe Interstitial Impurity-Induced Surface Magnetism in αPbO
E. F. Arguelles, S. Amino, S. Aspera, H. Nakanishi, and H. Kasai
Osaka University, Osaka, Japan, February, 2015

55th Japan Vacuum Society Meeting (poster presentation)
Interstitial Impurity-Induced Magnetism in αPbO
E. F. Arguelles, S. Amino, S. Aspera, H. Nakanishi, and H. Kasai
Isite Namba, Osaka, Japan, November, 2014

International Symposium on Computics: Quantum Simulation and Design (ISC-QSD) (poster presentation)
Surface Magnetism in αPbO
E. F. Arguelles, S. Amino, S. Aspera, H. Nakanishi, and H. Kasai
The University of Tokyo, Tokyo, Japan, December 2014

IEE International Magnetics Conference (Intermag) (oral presentation)
The Yoshimori Kasai Model
H. Kasai, E. F. Arguelles, and M. Alaydrus
Dresden, Germany, May, 2014

GCOE International Workshop on Atomically Controlled Fabrication Technologies (poster presentation)
Electron-Magnon Interactions in Fe-based Superconductors
E. F. Arguelles, and H. Kasai
Osaka University, Nakanoshima Campus, Osaka, Japan, February, 2014

International Symposium on Science Explored by Ultra Slow Muon (USM 2013) (oral presentation)
Yoshimori-Kasai Model Phase Diagram and Naniwa Series for Quantum Dynamics
H. Kasai, E. F. Arguelles, K. Shimizu, and H. Nakanishi
Matsue, Shimane, Japan, September, 2013

Workshop on Strongly Correlated Systems (oral presentation)
Electron-Magnon Coupling in Iron-pnictides
E. F. Arguelles, and H. Kasai
Osaka University, Osaka, Japan, August, 2013

Bibliography

[1] R. Janish, P. Gopal, and N.A. Spalding. *Journal of Physics: Condensed Matter*, 17:R675, 2005.

[2] Walther Gerlach and Otto Stern. *Zeitschrift für Physik*, 9:349–352, 1922.

[3] Walther Gerlach and Otto Stern. *Zeitschrift für Physik*, 9:353–355, 1922.

[4] W. Gerlach and O. Stern. *Zeitschrift für Physik*, 8:110–111, 1922.

[5] W. Pauli. *Zeitschrift für Physik*, pages 601–623.

[6] P. A. M. Dirac. *Proceedings of the Royal Society of London A: Mathematical, Physical and Engineering Sciences*, 117:610–624, 1928.

[7] G. Binasch, P. Grünberg, F. Saurenbach, and W. Zinn. *Physical Review B*, 39: 4828–4830, 1989.

[8] M. N. Baibich, J. M. Broto, A. Fert, F. Nguyen Van Dau, F. Petroff, P. Etienne, G. Creuzet, A. Friederich, and J. Chazelas. *Physical Review Letters*, 61:2472–2475, 1988.

[9] S.A. Wolf, P.D. Awschalom, R.A. Buhrman, J.M Daughton, S. von Molnár, M.L. Roukes, A.Y. Chtchelkanova, and D.M. Treger. *Science*, 294:1488–1495, 2001.

[10] H. Ohno. *Nature Materials*, 9:952, 2010.

[11] T. Dietl. *Nature Materials*, 9:965, 2010.

[12] T. Bland, K. Lee, and S. Steinmuller. *Physics World*, 21:24–28, 2008.

[13] D.D. Awschalom and M.E. Flatté. *Nature Physics*, 3:153, 2007.

[14] Igor Žutić, Jaroslav Fabian, and S. Das Sarma. *Review of Modern Physics*, 76: 323–410, 2004.

[15] T. Dietl, H. Ohno, F. Matsukura, J. Cibert, and D. Ferrand. *Science*, 287:1019, 2000.

[16] M.J. Calderón and S. Das Sarma. *arXiv:cond-mat/0603182v2*, 2006.

[17] Carten Timm. *Journal of Physics: Condensed Matter*, 15:R1865, 2003.

[18] Mona Berciu and R. N. Bhatt. *Physical Review B*, 66:085207, 2002.

[19] A.L. Chudnovskiy and D. Pfannkuche. Influence of disorder on ferromagnetism in diluted magnetic semiconductos. *Physical Review B*, 65:165216, 2002.

[20] D Matsunaka, MD M Rahman, H Kasai, W A Diño, and H Nakanishi. *Journal of Physics: Condensed Matter*, 16:S5787, 2004.

[21] T. Fukumura, Z. Jin, A. Ohtomo, H. Koinuma, and M. Kawasaki. *Journal of Applied Physics*, 75:3366, 1999.

[22] Y.J. Matsumoto, M. Murakami, T.J. Shono, T. Hasegawa, T. Fukumura, M. Kawasaki, P. Ahmet, T. Chikyow, S.Y. Koshihara, and H. Koinuma. *Science*, 291:854, 2001.

[23] Y.J. Matsumoto, M. Murakami, T. Koida, X.-J. Fan, T. Hasegawa, T. Fukumura, M. Kawasaki, P. Ahmet, S.Y. Koshihara, and H. Koinuma. *Japan Journal of Applied Physics*, 40:L1204, 2001.

[24] K. Ueda, H. Tabata, and T. Kawai. *Applied Physics Letters*, 79:988, 2001.

[25] S.B. Ogale, R.J. Choudhary, J.P. Buban, S.E. Lofland, S.R. Shinde, S.N. Kale, V.N. Kulkarni, J. Higgins, C. Lanci, J.R. Simpson, N.D. Browning, S. Das Darma, H.D. Drew, R.L. Greene, and T. Venkatesan. *Physical Review Letters*, 91:07725, 2003.

[26] S.N. Kale, S.B. Ogale, S.R. Shinde, M. Sahasrabuddhe, V.N. Kulkarni, R.L. Greene, and T. Venkatesan. *Applied Physics Letters*, 82:2100, 2003.

[27] J. Philip, N. Theodoropolou, G. Barera, J.S. Moodera, and B. Satpati. *Applied Physics Letters*, 85:777, 2004.

[28] S.K. Srivastava, B. Barbara, O Boistron, S. Paihés, and G. Bouzerar. *Journal of Applied Physics*, 110:043929, 2011.

[29] Anatoly L. Buchachenko and Vitaly L. Berdinsky. *Chemical Reviews*, 102:603–612, 2002.

[30] Igor V. Khudyakov, Yuri A. Serebrennikov, and Nicholas J. Turro. *Chemical Reviews*, 93:537–570, 1993.

[31] Emanuel Kockrick, Franz Schmidt, Kristina Gedrich, Marcus Rose, Thomas A. George, Thomas Freudenberg, Ralph Kraehnert, Ralph Skomski, David J. Sellmyer, and Stefan Kaskel. *Chemistry of Materials*, 22:1624–1632, 2010.

[32] A Z Moshfegh. *Journal of Physics D: Applied Physics*, 42:233001, 2009.

[33] L. Österlund, I. Zoric-acute, and B. Kasemo. *Physical Review B*, 55:15452–15455, 1997.

[34] P.O. Gartland. *Surface Science*, 62:183 – 196, 1977.

[35] A.M Bradshaw, P Hofmann, and W Wyrobisch. *Surface Science*, 68:269 – 276, 1977.

[36] Karoliina Honkala and Kari Laasonen. *Physical Review Letters*, 84:705–708, 2000.

[37] Y. Yourdshahyan, B. Razaznejad, and B.I. Lundqvist. *Solid State Communications*, 117:531 – 535, 2001.

[38] Y. Yourdshahyan, B. Razaznejad, and B. I. Lundqvist. *Physical Review B*, 65: 075416, 2002.

[39] Jörg Behler, Bernard Delley, Sönke Lorenz, Karsten Reuter, and Matthias Scheffler. *Physical Review Letters*, 94:036104, 2005.

[40] K. Svensson, L. Bengtsson, J. Bellman, M. Hassel, M. Persson, and S. Andersson. *Physical Review Letters*, 83:124–127, 1999.

[41] L. Bengtsson, K. Svensson, M. Hassel, J. Bellman, M. Persson, and S. Andersson. *Physical Review B*, 61:16921–16932, 2000.

[42] Y. L. Sandler. *The Journal of Physical Chemistry*, 58:58–61, 1954.

[43] David White and Edwin N. Lassettre. *The Journal of Chemical Physics*, 32:72–84, 1960.

[44] Clarence M. Cunningham, Douglas S. Chapin, and Herrick L. Johnston. *Journal of the American Chemical Society*, 80:2382–2384, 1958.

[45] David White and Edwin N. Lassettre. *The Journal of Chemical Physics*, 32:72–84, 1960.

[46] Walter J. Haubach, Charles M. Knobler, Anthony Katorski, and David White. *The Journal of Physical Chemistry*, 71:1398–1402, 1967.

[47] W. J. Haubach, P. Radhakrishna, A. Katorski, R. Wang, and David White. chapter 6, pages 73–98.

[48] David White and W. J. Haubach. *The Journal of Chemical Physics*, 30:1368–1369, 1959.

[49] Jerome T. Jankowiak, Joseph M. Schwartz, and Philip A. Barrett. *Adsorption*, 20:173–188, 2014.

[50] Timur A. Grinev, Alexei A. Buchachenko, and Roman V. Krems. *ChemPhysChem*, 8:815–818, 2007.

[51] William R. Moore and Harold R. Ward. *Journal of the American Chemical Society*, 80:2909–2910, 1958.

[52] Ph. Avouris, D. Schmeisser, and J. E. Demuth. *Physical Review Letters*, 48:199–202, 1982.

[53] S. Andersson and J. Harris. *Physical Review Letters*, 48:545–548, 1982.

[54] S. Andersson and J. Harris. *Physical Review B*, 27:9–14, 1983.

[55] Ernest Ilisca. *Physical Review Letters*, 66:667–670, 1991.

[56] K. Fukutani, K. Yoshida, M. Wilde, W. A. Diño, M. Matsumoto, and T. Okano. *Physical Review Letters*, 90:096103, 2003.

[57] K. Niki, T. Kawauchi, M. Matsumoto, K. Fukutani, and T. Okano. *Physical Review B*, 77:201404, 2008.

[58] R. Muhida, Y. Miura, W. A. Diño, H. Kasai, H. Nakanishi, A. Okiji, K. Fukutani, and T. Okano. *Journal of Applied Physics*, 93:644–648, 2003.

[59] K. Svensson and S. Andersson. *Physical Review Letters*, 98:096105, 2007.

[60] A. Okiji and N. Kawakami. *Journal of Magnetism and Magnetic Materials*, 31: 539 – 540, 1983.

[61] A. Yoshimori and H. Kasai. *Journal of Magnetism and Magnetic Materials*, 31: 475 – 476, 1983.

[62] Nghiem Thi Minh Hoa, Wilson Agerico Diño, and Hideaki Kasai. *Journal of the Physical Society of Japan*, 81(2):023706, 2012.

[63] Emi Minamitani, Wilson Agerico Diño, Hiroshi Nakanishi, and Hideaki Kasai. *Physical Review B*, 82:153203, 2010.

[64] P. Wahl, P. Simon, L. Diekhöner, V. S. Stepanyuk, P. Bruno, M. A. Schneider, and K. Kern. *Physical Review Letters*, 98:056601, 2007.

[65] Emi Minamitani, Noriyuki Tsukahara, Daisuke Matsunaka, Yousoo Kim, Noriaki Takagi, and Maki Kawai. *Physical Review Letters*, 109:086602, 2012.

[66] S. Munnix and M. Schmeits. *Physical Review B*, 33:4136–4144, 1986.

[67] J. Berashevich and A. Reznik. *arXiv:1303.7250v2*, 2013.

[68] J. Berashevich, J. A. Rowlands, and A. Reznik. *Europhysics Letters*, 102:47002, 2013.

[69] H.J. Terpstra, R.A. de Groot, and C. Haas. *Physical Review B*, 52:11690, 1995.

[70] J. Berashevich and A. Reznik. *arXiv:1304.2945v1*, 2013.

[71] M. Khalid, A. Setzer, M. Ziese, P. Esquinazi, D. Spemann, A. Pöppl, and E. Goering. *Physical Review B*, 81:214414, 2010.

[72] T. Dietl, A. Haury, and Y. Merle d'Aubigné. *Physical Review B*, 55:R3347–R3350, 1997.

[73] M. Venkatesan, C. B. Fitzgerald, J. G. Lunney, and J. M. D. Coey. *Physical Review Letters*, 93:177206, 2004.

[74] Jörg Behler, Bernard Delley, Sönke Lorenz, Karsten Reuter, and Matthias Scheffler. *Physical Review Letters*, 93:036104, 2005.

[75] P. Sati, R. Hayn, R. Kuzian, S. Régnier, S. Schäfer, A. Stepanov, C. Morhain, C. Deparis, M. Laügt, M. Goiran, and Z. Golacki. *Physical Review Letters*, 96: 017203, 2006.

[76] G. T. Thaler, M. E. Overberg, B. Gila, R. Frazier, C. R. Abernathy, S. J. Pearton, J. S. Lee, S. Y. Lee, Y. D. Park, Z. G. Khim, J. Kim, and F. Ren. *Applied Physics Letters*, 80:3964–3966, 2002.

[77] K. Ando. *Applied Physics Letters*, 82:100–102, 2003.

[78] Z.W. Pan, Z.R. Dai, and Z.L. Wang. *Applied Physics Letters*, 80:309, 2002.

[79] Kay Potzger and Shengqiang Zhou. *physica status solidi (b)*, 246:1147–1167, 2009.

[80] S. Banerjee, M. Mandal, N. Gayathri, and M. Sardar. *Applied Physics Letters*, 91: 182501, 2007.

[81] M. Khalid, M. Ziese, A. Setzer, P. Esquinazi, M. Lorenz, H. Hochmuth, M. Grundmann, D. Spemann, T. Butz, G. Brauer, W. Anwand, G. Fischer, W. A. Adeagbo, W. Hergert, and A. Ernst. *Physical Review B*, 80:035331, 2009.

[82] A. Barla, G. Schmerber, E. Beaurepaire, A. Dinia, H. Bieber, S. Colis, F. Scheurer, J.-P. Kappler, P. Imperia, F. Nolting, F. Wilhelm, A. Rogalev, D. Müller, and J. J. Grob. *Physical Review B*, 76:125201, 2007.

[83] Thomas Tietze, Milan Gacic, Gisela Schütz, Gerhard Jakob, Sebastian Brück, and Eberhard Goering. *New Journal of Physics*, 10:055009, 2008.

[84] J. Berashevich and A. Reznik. *Europhysics Letters*, 104:37008, 2013.

[85] W. Kohn and L. J. Sham. *Physical Review*, 140:A1133–A1138, 1965.

[86] P. Hohenberg and W. Kohn. *Physical Review*, 136:B864–B871, 1964.

[87] G. Kresse and J. Furthmüller. *Computational Materials Science*, 6:15 – 50, 1996.

[88] H. J. Terpstra, R. A. de Groot, and C. Haas. *Physical Review B*, pages 11690–11697, 1995.

[89] K. Sato and H. Katayama-Yoshida. *Semiconductor Science and Technology*, 17: 367–376, 2002.

[90] K. Sato, L. Bergqvist, J. Kudrnovsky, P.H. Dederichs, O. Eriksson, I. Turek, B. Sanyal, G. Bouzerar, H. Katayama-Yoshida, V. A. Dinh, T. Fukushima, H. Kizaki, and R. Zeller. *Reviews of Modern Physics*, 82:1633, 2010.

[91] H. Akai. *Physical Review Letters*, 81:3002–3005, 1998.

[92] P. Yu, X. F. Jin, J. Kudrnovský, D. S. Wang, and P. Bruno. *Physical Review B*, 77:054431, 2008.

[93] Eddy Bernard, Céline Houriez, Alexander O. Mitrushchenkov, Marie Guitou, and Gilberte Chambaud. *The Journal of Chemical Physics*, 142:054703, 2015.

[94] K. Fukutani and T. Sugimoto. *Progress in Surface Science*, 88:279 – 348, 2013.

[95] Yoshinori Takahashi. *Journal of the Physical Society of Japan*, 43:1342–1350, 1977.

[96] N. D. Lang and W. Kohn. *Physical Review B*, 1:4555–4568, 1970.

[97] John Bardeen. *Physical Review*, 49:653–663, 1936.

[98] Irving Langmuir. *Journal of the American Chemical Society*, 40:1361–1403, 1918.

[99] B. Hammer, O.H. Nielsen, and J.K. Nørskov. *Catalysis Letters*, 46:31–35, 1997.

[100] B. Hammer. *Physical Review Letters*, 83:3681–3684, 1999.

[101] G.A. Somorjai. volume 26 of *Advances in Catalysis*, pages 1 – 68. Academic Press, 1977.

[102] R. Ducros, M. Housley, and G. Piquard. *Physica Status Solidi (a)*, 56:187–193, 1979.

[103] Jacques Jupille, Pierre Pareja, and Jean Fusy. *Surface Science*, 139:505 – 540, 1984.

[104] Shuichi Amino, Elvis Arguelles, Wilson Agerico Dino, Michio Okada, and Hideaki Kasai. *Physical Chemistry Chemical Physics*, 18:23621–23627, 2016.

[105] Daichi Yamazaki, Michio Okada, Francisco C. Franco Jr., and Toshio Kasai. *Surface Science*, 605:934 – 940, 2011. ISSN 0039-6028.

[106] Jr. Nelson B. Arboleda, Hideaki Kasai, Wilson A. Diño, and Hiroshi Nakanishi. *Japanese Journal of Applied Physics*, 46:4233, 2007.

[107] H.J. Robota, W. Vielhaber, M.C. Lin, J. Segner, and G. Ertl. *Surface Science*, 155:101 – 120, 1985.

[108] J. Harris. *Langmuir*, 7:2528–2533, 1991.

[109] L. Barrio, P. Liu, J. A. Rodríguez, J. M. Campos-Martín, and J. L. G. Fierro. *The Journal of Chemical Physics*, 125:164715, 2006.

[110] B. Hammer and J.K. Nørskov. *Nature*, 376:238 – 240, 1995.

[111] B. Hammer and J.K. Nørskov. *Surface Science*, 343:211 – 220, 1995.

[112] Nuria Lopez and Jens K. Nørskov. *Journal of the American Chemical Society*, 124:11262–11263, 2002.

[113] A. S. Mårtensson, C. Nyberg, and S. Andersson. *Physical Review Letters*, 57: 2045–2048, 1986.

[114] Uwe Muschiol, Pia K. Schmidt, and Klaus Christmann. *Surface Science*, 395:182 – 204, 1998.

[115] Pia K. Schmidt, Klaus Christmann, Georg Kresse, Jürgen Hafner, Markus Lischka, and Axel Groß. *Physical Review Letters*, 87:096103, 2001.

[116] Markus Lischka and Axel Groß. *Physical Review B*, 65, 2002.

[117] W.A. Diño, H. Kasai, and A. Okiji. *Progress in Surface Science*, 63:63 – 134, 2000.

[118] Toshiki Sugimoto and Katsuyuki Fukutani. *Physical Review Letters*, 112:146101, 2014.

[119] Toshiki Sugimoto and Katsuyuki Fukutani. *Nature Physics*, 7:307, 2011.

[120] D. Ivanov, T. Ohno, E. F. Arguelles, W. A. Diño, and K. Fukutani. *Private Communication*, 2017.

[121] T. Ohno, D. Ivanov, E. F. Arguelles, W. A. Diño, and K. Fukutani. *submitted to Physical Review Letters*, 2017.

[122] N. M. Rosengaard and Börje Johansson. *Physical Review B*, 55:14975–14986, 1997.

[123] Yu-mei Zhou, Ding-sheng Wang, and Yoshiyuki Kawazoe. *Physical Review B*, 59: 8387–8390, 1999.

[124] M. Pajda, J. Kudrnovský, I. Turek, V. Drchal, and P. Bruno. *Physical Review B*, 64:174402, 2001.

[125] G. Kresse and J. Furthmüller. *Computer Materials Science*, 6:15, 1996.

[126] G. Kresse and J. Furthmüller. *Physical Review B*, 54:11169, 1996.

[127] W. Kohn and L.J. Sham. *Physical Review*, 140:A1133, 1965.

[128] P. Hohenberg and W. Kohn. *Physical Review*, 136:B864, 1964.

[129] P.E. Blöchl. *Physical Review B*, 50:17953, 1994.

[130] J.P. Perdew, K. Burke, and M. Ernzerhof. *Physical Review Letters*, 77:3865, 1996.

[131] H.J. Monkhorst and J.D. Pack. *Physical Review B*, 13:5188, 1976.

[132] J. Klimes, D.R. Bowler, and A. Michelides. *Journal of Physics: Condensed Matter*, 22:022201, 2010.

[133] J. Klimes, D.R. Bowler, and A. Michelides. *Physical Review B*, 83:195131, 2011.

[134] J. Leciejewicz. *Acta Crystallographica*, 14:1304, 1961.

[135] W.J. Moore and L. Pauling. *Journal of American Chemical Society*, 63:1392, 1941.

[136] P. Canepa, P. Ugliengo, and M. Alfredson. *Journal of Physical Chemistry C*, 116: 21514, 2012.

[137] Jean-Marc Raulot, Gianguido Baldinozzi, Ram Seshadri, and Pietro Cortona. *Solid State Sciences*, 4:467 – 474, 2002.

[138] J Berashevich, O Semeniuk, O Rubel, J A Rowlands, and A Reznik. *Journal of Physics: Condensed Matter*, 25:075803, 2013.

[139] R. C. Keezer, D. L. Bowman, and J. H. Becker. *Journal of Applied Physics*, 39: 2062–2066, 1968.

[140] P. Hohenberg and W. Kohn. *Physical Review*, 136:B864–B871, 1964.

[141] W. Kohn and L. J. Sham. *Physical Review*, 140:A1133–A1138, 1965.

[142] G. Kresse and D. Joubert. *Physical Review B*, 59:1758–1775, 1999.

[143] J.P. Perdew, J.A. Chevary, S.H. Vosko, K.A. Jackson, M.R. Pederson, D.J. Singh, and C. Fiolhais. *Physical Review B*, 46:6671–6687, 1992.

[144] J.P. Perdew, K. Burke, and M. Ernzerhof. *Physical Review Letters*, 77:3865–3868, 1996.

[145] Hendrik J. Monkhorst and James D. Pack. *Physical Review B*, 13:5188–5192, 1976.